A Study on Vision-based Distributed Displacement Measurement for Structural Health Monitoring

(構造物ヘルスモニタリングのための
ビジョンベースド変位分布計測の研究)

by

Muhammad Zulhaj Aliansyah
D163724

Graduate School of Engineering
Hiroshima University
October 2021

Contents

List of Figures

List of Tables

Chapter 1

Introduction

1.1 Background

Bridge is a structure characterized by its span which traverse over physical obstruction from topological and structural conditions, e.g., river, valley, railway, or elevated roads. The presence of the bridges provides connection in the transport system and, in turn, the society at large. Bridge has served a vital part in the transportation system by allowing road and train traffic, movement of people and goods, pipes and cable connection, and many more.

A bridge's inability to serve its purpose may dramatically affect the connectivity in the transport system, resulting in a longer travel route or an isolated area removed from the transport network. The failure of bridges often result in casualties and definitive large-scale monetary loss, thus such failures need to be prevented.

In recent years, large number of vital bridges are beginning to age worldwide, and rather simultaneously. This is due to the rapid development across nations from the 1960s to the 1980s. Given that most of bridges are design to last 50 years [1], most of the old bridges, often with steel truss construction will require proper assessment prior to retrofit or replacement. The focus of the assessment also should not leave the newer bridges built using pre-stressed construction method from 1980s onwards. Noting the higher load rating and the possibility of concrete spalling and cracking leading to internal corrosion, assessment on such bridges should be more comprehensive and holistic.

1.2   Structural deterioration and damages on bridges

Upon its construction, a bridge is constantly subject to damages from environmental factors or inherent usage loads during its service life. The damages to a bridge can be categorized into three kinds of effects [2]:

- primary effects—related to the bridge's material, construction type, shape, and design considerations in relation to the bridge's expected load and its dead weight under static condition,

- secondary effects—identified from the time-bound dynamic structural response excited from forcing actions due vehicular loads, wind, quake, or thermal expansion/shrinkage, which is often non-linear and inelastic,

- tertiary effects—not directly related to static nor dynamic properties of the bridge, which include environmental factors such as vegetation overgrowth, rust on metal reinforcing members, paint decontamination, water ponding, deck spalling, erosion, silting, etc. [3].

Although these three effects are in interplay with one another, addressing them is often done separately. Primary effects should have been addressed well in the design phase and carried well throughout the construction process. Secondary effects are to be evaluated using finite-element simulation or direct measurements on the structure under a defined load. Tertiary effects are usually assessed by routine direct visual inspection on the structure by designated personnel.

Condition assessment and maintenance need to be done to maintain the safety and durability of the bridge, especially to address the second and third effects of damage. Given the natural deterioration of damages, early damage detection may facilitate more economical management and maintenance of modern infrastructure in the long run. Detection of damages at early stage allows longer expected service life, relative ease to address smaller damage, and prevention of damage accumulation [4]. Such assessment and maintenance of structural integrity and detecting damage in a structure is often referred as structural health monitoring [5].

1.3 Methods of structural health monitoring

Structural health monitoring (SHM) has become prominent topic in the field of civil engineering in safety evaluation, detecting structural damage, estimating remaining service life of structure, optimizing decision making process on maintenance, maintenance support and aiding performance-based structure design methodology [5–8].

Various methods have been developed to detect structural damage before the damage being irreparable. The most common practice of bridge structural health monitoring is visual inspection on the structure's members and joints at intervals from one to five years interval [9], followed by the more detailed non-destructive examination if required, such as hammering test to identify local damage from corrosion if deemed to be required[10]. The visual inspection and local non-destructive examination methods are deemed to be unreliable, expensive, and impractical to carry out in a timely manner on larger structures [5, 11] due to several factors:

- lack of budget, especially for bridges deemed less important,

- small number of trained inspectors,

- subjectivity and variability of judgment criteria,

- potential of damage location at hard-to-reach areas.

Such tests required expensive equipment, laborious arrangements, need of destructive specimen sampling, and often service suspension of the bridge.

As an alternative, dynamics measurement is often employed for inspection and become more prominent structural health monitoring techniques. Dynamics measurement is carried out by measuring displacement or acceleration at different points on the structure using sensors. The dynamic characteristics of the structure derived from dynamics measurement, such as the natural frequency and damping ratio, are then compared with the numerical analysis results, i.e. whether the value of displacement and derived properties are still within range of the design value.

1.4   Structural health monitoring by dynamics measurement

Bridges are subject to repetitive and temporary external forces from wind, current, quakes, and load in addition to its inherent weight. Upon being applied, these forces induce displacement of structure's members. Energy from those acting forces needs on a bridge to be adequately dissipated for the structure to return to its normal elastic state. The inability to properly dissipate applied force may lead to damage from irreversible plastic deformation of the structure. Due to varying mass, stiffness, and damping coefficient of different members of the structures, this results in random vibration occurring on the structure [12]. In addition to the forcing actions excited on the bridge could possibly be moving, changing orientation, or having fluctuating level at rather arbitrary point of time and space; measurement at static condition may not suffice to tell the whole structural integrity of bridges.

Dynamics measurement is one of technique to evaluate structural integrity and to diagnose deterioration of structures, done by measuring the time-varying displacement of several defined measurement points along the structural members deemed to be important. Damage or loss of integrity can be evaluated by measuring defined parameters derived from the measured displacement from several designated easily accessible points on the structure [13]. As dynamic displacement characteristics of a structure may change due to different loading conditions, temperature, deteriorating members, or presence of structural damage [14], measurements shall considers these variations when evaluating the structural integrity. Structural damages can often be characterized by discontinuity and excessive level of the measured displacement signals.

Furthermore, evaluation of derived metrics from the measured dynamics displacement, e.g. natural vibration frequencies of the structure, may tell the vibration characteristics and asses the global overall structural integrity of the structure [15]. The presence of local damage in a bridge can be detected using analysis from dynamics measurement involving displacement and its derivatives, i.e. mode shapes, the corresponding frequencies, damping coefficients, etc.

Various types of structural damages can be inferred from dynamics measurement of displacement and its derivatives, along with the corresponding caveats, these include:

- overloading can be detected when peak displacement exceeds its design value [16]. Some materials may observe changing behavior due to different loading condition in static and dynamic loading, thus distinct static and dynamic load ratings;

- localized crack or loose connection along the span of particular structure can estimated from slight changes in the mode shape [17] or minute changes in natural frequencies [18];

- decrease of the associated natural frequency in the specific direction happens along with the increase of the damage severity [19], implying the stiffness reduction in a particular member of the bridge or failing damping devices;

- cumulative plastic displacement may tell sign of fatigue-damaged or deformed members or joints [20].

Researches on structural health monitoring using structural dynamic responses focused separately either on limited local damage detection or on global damage assessment. The latter approach poses several limitations:

- structures are large and complex but damage is usually localized,

- natural frequency shift and dissipation properties change due to local damage is very small despite the relatively high precision measurement of vibration-based methods [21],

- modal shape change may be more sensitive to whole structure damage but easily disturbed by noise due to scattered applied forces, bending rigidity and dampening devices [22], thus causing uncertainties.

Employing more measurement points for the dynamics analysis will help to obtain more precise damage localization along with more precise global assessment.

Convenient method for structural health monitoring should be realized to address the vast number of bridges in lieu of sophisticated arrangement of instruments [23, 24], and ease of installation and flexibility of deployment in the field should be taken into account for minimizing social and economic losses with traffic regulation during the inspection, in addition to the inherently important resolution and accuracy of the measurements.

Environmental factors, e.g. temperature, humidity, river flow, and wind, have some effect on the variations of dynamic properties of bridges [25]. Integrating dynamics measurement with other sensors and measurement methods would be highly beneficial to obtain more holistic assessment of the structural health, e.g. weather station, traffic counting, seismograph, etc [26].

1.5   Displacement measurement methods

1.5.1   Conventional methods

Dynamics measurement is often done with contact sensors such as strain gauges, fiber Bragg gratings, penetrating radar, accelerometer. Contact sensors attached on a structure (e.g., accelerometers, strain gauges [27–30], and GPS systems) [31–34] or optical sensors for remote monitoring (e.g., laser-based vibrometers [35–38] and radar interferometry systems [39, 40]) have been used to inspect the dynamic responses of many structures.

These sensors are limited due to the need to be placed on the exact damage locations, also sufficient numbers are required to allow interpolation of the global structural response [41]. Several electronics contact sensors, such as accelerometers, are also susceptible to distortion in extracted time histories of estimated displacement from double integration [42]. At last, the requirement to attach them to measurement points on outdoor large-scale structures is time-consuming and often dangerous.

Vision-based systems are proposed to simultaneously capture the displacement of structural members without direct contact with the structure [43]. Captured displacement data can be then further processed for dynamics analysis. Though vision-based structural displacement measurement using is still regarded as a promising emerging technology in

structural health monitoring. Measurement sensitivity of vision-based system needs to be high because small changes in structural response produced from damage are often below the noise from environmental effects [5].

1.5.2   High-speed vision system

With the advent of digital cameras with higher performances: frames per second, pixels size and density, memory bandwidth, and image stabilization; high-speed vision becomes viable method for dynamics measurement. High-speed vision system works by capturing motion of structural members during specified loading condition on the structure at high frequency. The higher sampling frequency allows oversampling of the measured displacement signal resulting in finer temporal resolution. This may allow to detect early stage of damage hinted from subtle frequency response shift and modal shape change.

Equipped with the high pixel density and long-focal length telephoto lens, vision system may allow measurement of small structural displacement from a long distance. Although, long distance measurement resulted in narrower and more-localized field of view, thus lesser spatial resolution in global terms, as illustrated in Figure 1.1. Digital image correlation and motion magnification may improve the resulting spatial resolution of the measurement and produce agreeable result in terms of accuracy and precision [44, 45]. Nonetheless, there is still the need for further evaluation of the reliability and accuracy of these vision-based system, especially on a real-time monitoring of large structures and under adverse weather conditions.

short focal length
wide field of view

long focal length
narrow field of view
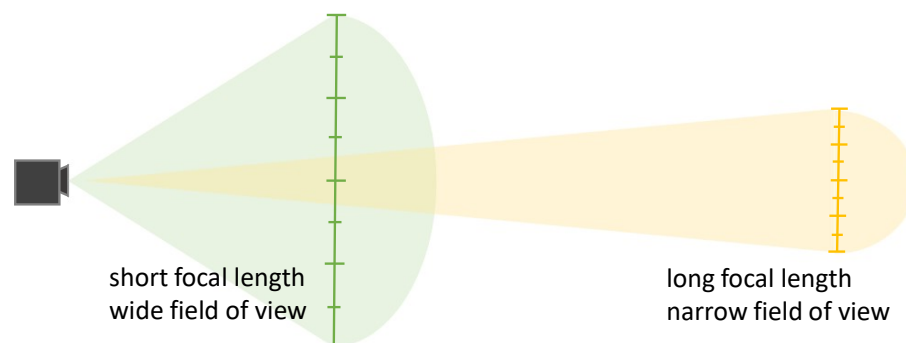
Figure 1.1: Focal length and field of view relationship.

Optical performance of the vision system also dictates the overall measurement resolution. There are trade-offs to be made regarding various optical parameters: narrow aperture will increase the depth of field, increasing the precision of the measurement at the cost of underexposed captured image, longer focal length will allow longer measurement distance but will limit the breadth of field view and depth of field. Hence, optical parameters for dynamic displacement measurement should be carefully determined to obtain accurate measurement result. The trade-off for high-speed vision system implementation for structural dynamics measurement is summaried in Table 1.1.

Table 1.1: Vision system trade-offs.

Parameters	Merit	Demerit
Focal length		
Long	long distance capability, fine spatial resolution	underexposure, heat haze, shallow depth of field
Short	wide field of view, plenty exposure	coarse spatial resolution
Exposure		
Short	fine temporal resolution, less motion blur	underexposure
Long	plenty exposure	coarse temporal resolution, chance of motion blur
Aperture		
Narrow	good focus, deep depth of field	underexposure
Wide	plenty exposure	focal blur, shallow depth of field

1.6   Purpose of the study

The study aims to verify the feasibility and to address the current limitations of structural health monitoring approaches on bridges using vision-based dynamics measurement system. The limitations to be addressed include the limited measurement points across the structure, camera placement to allow simultaneous measurement of lateral and vertical motion of the structure, overall accuracy and precision of the measurement, and the applicable measurement distance in the actual field.

Robustness also needs to be considered against various measurement noises, such as ambient vibration and optical distortion. Convenient deployment without traffic closure is desired not to impede the bridge operation while using the expected load from driving-by traffic as sources of vibration.

1.7   Organization of the thesis

Figure 1.2 illustrates how this thesis is organized related to vision-based structural health monitoring of viaduct bridges. Chapter 1 explains the importance of structural health monitoring, its applicable measurement methods and structural test, and the viability of vision-based system to perform so.

Chapter 2 presents the application of high-speed vision system for distributed displacement measurement and subsequent dynamic analysis. Chapter 3 extends the application of high-speed vision system with set of half-mirror and full-mirror to allow capturing displacement at both sides of a bridge model.

Chapter 4 delves into the vision system integration of displacement measurement camera and traffic counting camera to capture vehicle-specific structural response of an actual bridge in a field experiment with normal traffic.

Chapter 5 presents the concluding remarks of the study and recommendations for possible future researches.
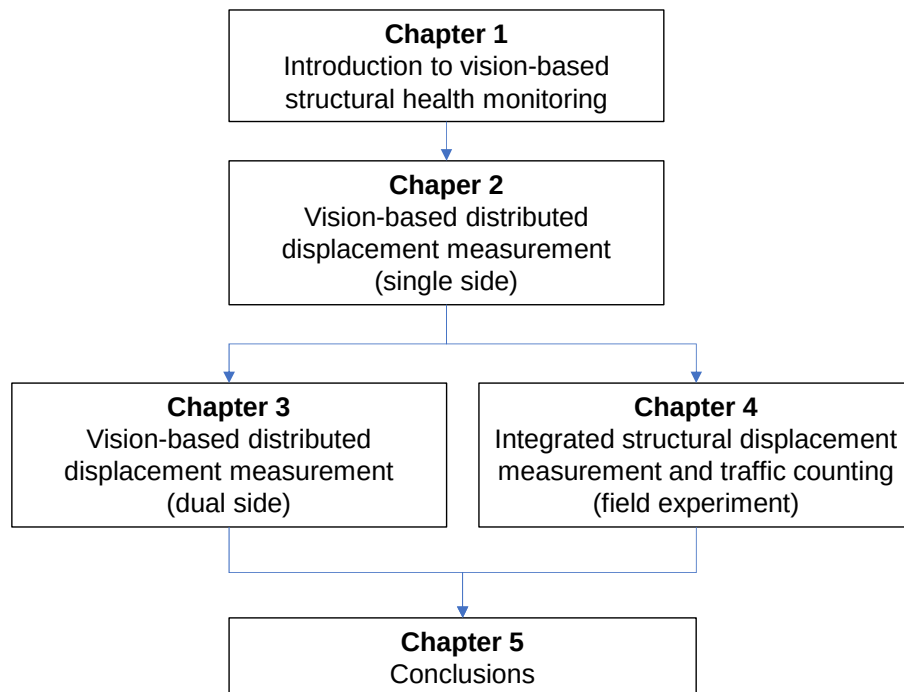
Figure 1.2: Organization of this study.

Chapter 2

High-speed Vision System for Dynamic Structural Distributed Displacement Analysis

2.1 Introduction

Dynamics measurement is one of important techniques in structural health monitoring on bridges by inspecting their dynamics properties. The properties are mainly derived from the measured displacement time-series from multiple measurement points across the structure. Various conventional distributed displacement measurement techniques of civil structures currently in place have been limited due to various constraints: inadequate accuracy, narrow distribution of measurement points, measurement drift, robustness issue on field usage, structural obstruction, and reliability for long-term installation. Vision-based measurement provides alternative for contact-less distributed displacement measurement over some distance. The increasing availability of high-performance vision systems provides the potential for developing adaptable and reconfigurable monitoring systems of complex deformation field measured at various locations and orientations [42].

Vision-based method utilizing high-contrast markers has been proposed in this study as an alternative for dynamic distributed displacement measurement of a bridge model. This method incorporates a system of high-speed camera system equipped with telephoto lens. The camera optical axis is placed rather parallel to the bridge model's axis. This allows capturing of both lateral and vertical displacement of multiple markers the bridge members. LED and retro-reflective corner cube optical prism were utilized to serve as high-contrast markers to cope with the insufficient incident light over long distance and

small camera aperture. This also helps locating the position of the markers by providing visual cue. The markers were aligned within the depth of field of the vision system with different slant angles so that all markers could be captured in a single field of view from the camera without occlusion.

Scaling factor, representing the actual physical displacement of each marker from the perceived pixel-wise motion in the captured image, was calculated taking into account the slant angles of each particular marker. The accuracy of the measured displacement was calibrated against laser displacement sensor and optical jig. Estimated displacement from dynamics measurement was compared against contact accelerometer. Subsequent analysis was conducted to identify natural vibration frequencies of the structure using Fast Fourier Transform and damping ratio estimation using peak-picking method.

2.2   Related works on vision-based structural displacement measurement

Vision system works in structural dynamics measurement by capturing the motion of markers, either using natural markers (edges, surfaces, or points in the structure) or artificial markers (LEDs, printed patterns, optical markers). Pixel-wise motion in the captured image is then converted to physical displacement value according to calibrated scaling factors. The process can be done either real-time or post-process. Data of estimated structural displacement can be then further processed for various SHM evaluations, e.g.natural frequencies, modal parameters, and mode shapes [46][47].

Vision system can capture displacement of grater number of points more flexibly compared to more conventional contact-based measurement. The denser measurement points allow for smoother mode shape and interpolation of structural member response. Additional camera head(s) can also be added for camera calibration to obtain more precise displacement in 3D plane given that the position of camera heads and markers are well-defined in the global coordinate system [48].

Image captured by vision system is subject to distortion, both from the optics or the non-orthogonal orientations towards the test structure. It was demonstrated that the

pan/tilt angle between the camera head and test structure should be not more than 10°
to reduce errors from focal distortion [49]. Satisfactory measurement accuracy could be
achieved for small tilt angles with distance 300 m away from the target structure [46].
Thus, a trade off between the measurement resolution and the breadth of field of view of
multiple markers is necessary. In addition, application of vision system in field has to take
into account various factors from the environment. Vision system is also susceptible to
errors caused by the heat haze and camera vibrations when measuring small displacement
from long-distance [47]

Optical motion tracking system using surveillance camera was proposed to mea-
sure induced motion in the event of an earthquake [50], but the system is limited due to
low frame rate, and low pixel resolution of the surveillance camera, and in the event of
an actual earthquake, inherent camera self-vibration resulting in unsteady measurement
reference point. Optical system with telephoto lens, focal length extender, and active
lighting device close to the camera may develop noticeable inaccuracy due to camera
head vibration and heat haze from the lighting device, thus operating time of the lighting
device needs to be limited [51]. This renders such system only suitable for structures with
routine periodical loading such as railway bridge.

Target-less vision-based displacement sensor system was proposed by extracting
and tracking feature points in video stream [49]. Multiple displacement point approach
can be achieved using image key-points [8], but these methods largely depend on low
noise image and crisp edges. Given that only feature point was extracted from a small
area and edge detection is susceptible to focal blur, the system isn't suitable for distributed
measurement points with different frontal distances, long distance measurement, and low
ambient lighting condition.

A more complex system incorporating two cameras equipped with telephoto lens
and non-coplanar control points markers with Affine camera modeling has been proposed
to measure tri-axis displacement and rotation of fixed monitoring zone of a structure [52].
Considering the extended period of operation, the geometry of components may change
due to temperature effects and camera frame synchronization had yet been taken into
account.

Herewith, a vision system comprises of a single camera head and high-contrast markers is proposed. Reference point is provided from fiducial marker(s) installed on the anchorage points of the bridge model to cancel out camera head vibration. High-contrast markers are utilized to cope with the scalable measurement distance, short exposure of high-frame vision system, and locate the position of each marker more reliably.

2.3   Truss vibration experiment with LED marker

Experiment was conducted to simultaneously capture lateral and vertical displacements of high-contrast markers installed on a test bridge model using high-speed camera system. Natural vibration frequencies of the structure was then to be evaluated to identify the vibration characteristics of the structure.

2.3.1   Experiment setup

Bridge model used for the experiment is Warren truss structure with L-beam aluminum (25 mm flanges, 1.2 mm thickness) for end posts, top and bottom chords, and flat aluminum strips (15 mm width, 2 mm thickness) for the struts and diagonal members. The span, height, and width of the truss are 4 m, 21 cm, and 33 cm respectively. The bridge model incorporates no deck and bracing.

LED markers are $5\varnothing$mm in with white color, installed 25 cm apart between one another. Figure 2.1 shows 16 LED makers installed on a single side of lower chord of the deckless truss. Excitation force was applied to the center of the span on both bottom chords with arbitrary hand force with general upwards direction using a rod to tap both sides' chords simultaneously.

Focal length, aperture, and focus distance need to be adjusted proportionally to cover the whole span of the truss within the depth of field of the camera. The equation to the depth of field (D_{dof}) is given as:

$$D_{dof} = D_d - D_d \tag{2.1}$$

Figure 2.1: Test truss structure with LEDs attached on a single lower chord of the truss.

with D_p, D_d, and D_f are depth of field near limit distance and far limit distance. These two limits distance are evaluated to:

$$D_p = D_f - \frac{\epsilon N D_f^2}{f^2 + \epsilon N D_f} \tag{2.2}$$

$$D_d = D_f + \frac{\epsilon N D_f^2}{f^2 - \epsilon N D_f} \tag{2.3}$$

where N is aperture number, f is focal length, ϵ is blur diameter, D_f is focus distance. The aperture should be as narrow as possible to obtain the sharpest image possible and as much depth of field. Blur diameter is determined roughly given that the edges of each marker are still clearly identifiable in the captured image.

In the experiment, optical settings were 9.3 m focus distance with F/32 aperture at 410 mm focal length which resulted in depth of field of 4.178 m with 22 px acceptable blur diameter, covering the whole span of the truss bridge model (4 m). The closest marker was 7.3 m away from the camera, while the furthest one was 13.3 m away as illustrated in Figure 2.2.

The camera head was put 45 cm higher than the chord on which all sixteen LED markers vertically, also with slanted lateral angle between camera optical axis and bridge axis. Figure 2.1 shows general overview of the experiment setup with LED markers installed on one side of the test truss structure. This resulted in lateral distance of 20 cm between Marker1 and the optical axis and 13.3 cm between Marker16 and optical axis. The slant angles were introduced to eliminate occlusion between markers.

Scaling factor gives the ratio between vision-system resolution in pixels and actual
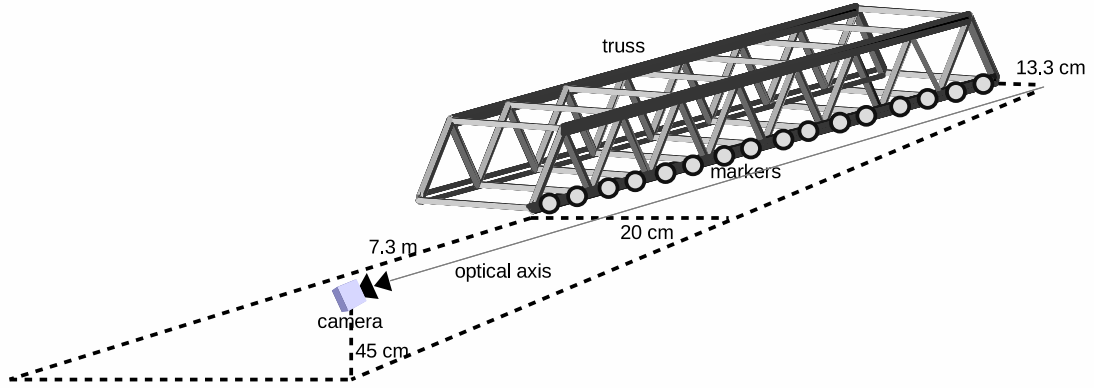
Figure 2.2: Placement of the vision system in relation to the bridge model.

physical dimension. For setups with non-perpendicular lens optical axis between camera and markers, scaling factors for lateral and vertical direction need to be estimated separately [53]. Scaling factor was calculated taking into account sensor size and distance between camera and marker, in addition to the frontal, lateral, and vertical distances between camera axis and LED markers.

As the camera head perceives displacement according to its sensor orientation, the scaling factor for both vertical and will be compensated so that the evaluated displacement use the orientation of the bridge model as coordinate system, following the equation:

$$SF_v = \frac{11.27D_m}{f\cos(\pi - \arctan(D_v/D_m))} \tag{2.4}$$

$$SF_l = \frac{11.27D_m}{f\cos(\pi - \arctan(D_l/D_m))} \tag{2.5}$$

where D_f, D_v, D_l, and D_m are frontal distance, vertical distance, lateral distance, and marker distance (Phytagorean resultant of D_f, D_v, and D_l). SF_v and SF_l are scaling factor in vertical and lateral direction respectively.

Summary of vision system specification is shown in Table 2.1. Image resolution was cropped to obtain effective frame rate to 180 fps due to hardware limitation. Camera head was set to capture the vibration of the bridge model at 180 fps for 10 seconds duration.

Table 2.1: Vision system specification (LED experiment).

Camera		Lens		Computer	
Ximea MQ042MG-C		SIGMA APO HSM 300-800		Dell Latitude 3540	
Resolution	2048x1024 px	Focal length	410 mm	Memory	8 GB
Sensor	5.5 μm pitch	Focus distance	9.3 m	OS	Ubuntu 14.04.1
Exposure, frame rate	5 ms, 180 fps	Aperture	F/32	CV library	OpenCV 2.4.8

2.3.2 Result and discussion

Pixel-wise motion of each marker was translated to actual displacement using its respective scaling factors after subtracted from its steady-state value. Each marker's centroid was extracted using OpenCV's `cvblob()` blob detection function to obtain the exact lateral and vertical position of each marker within the frame. The motion of each marker was then multiplied by its respective scaling factor to obtain distributed displacements of the structure after firstly subtracted from its steady state value, i.e. when no vibration were observed on the bridge model during prolonged duration.

Figure 2.3 shows six frames capturing minute pixel-wise motion of markers from t=3 s to t= 5.5 s with 0.5 s interval.

Figure 2.4 shows the truss' chord displacement from the same time span during each captured frame shown earlier. Figure 2.5 shows Marker9 displacement, positioned at the center of the truss' span, over the course of 10 s capture duration. A highlight at the displacement signal between t=3 s and t=4 s for lateral (Figure 2.5c) and vertical displacement (Figure 2.5d) shows the damped vibration with stable first mode vibration period.

Fast Fourier Transform (FFT) analysis was conducted to evaluate natural frequencies of the structure vibration. Only 1024 samples (t=2.5 s to t=8.183 s) was selected in order to avoid adding initial transient response to the natural frequency analysis. Peak-picking method was applied to frequency response of Marker9 vibration to extract up to fifth mode of vibration. Figure 2.6 shows the structure's frequency response both lateral and vertical directions. Table 2.2 summaries the natural vibration frequencies in both lateral and vertical directions.

Unique natural vibration frequency was observed on 8.6133 Hz for lateral direc-
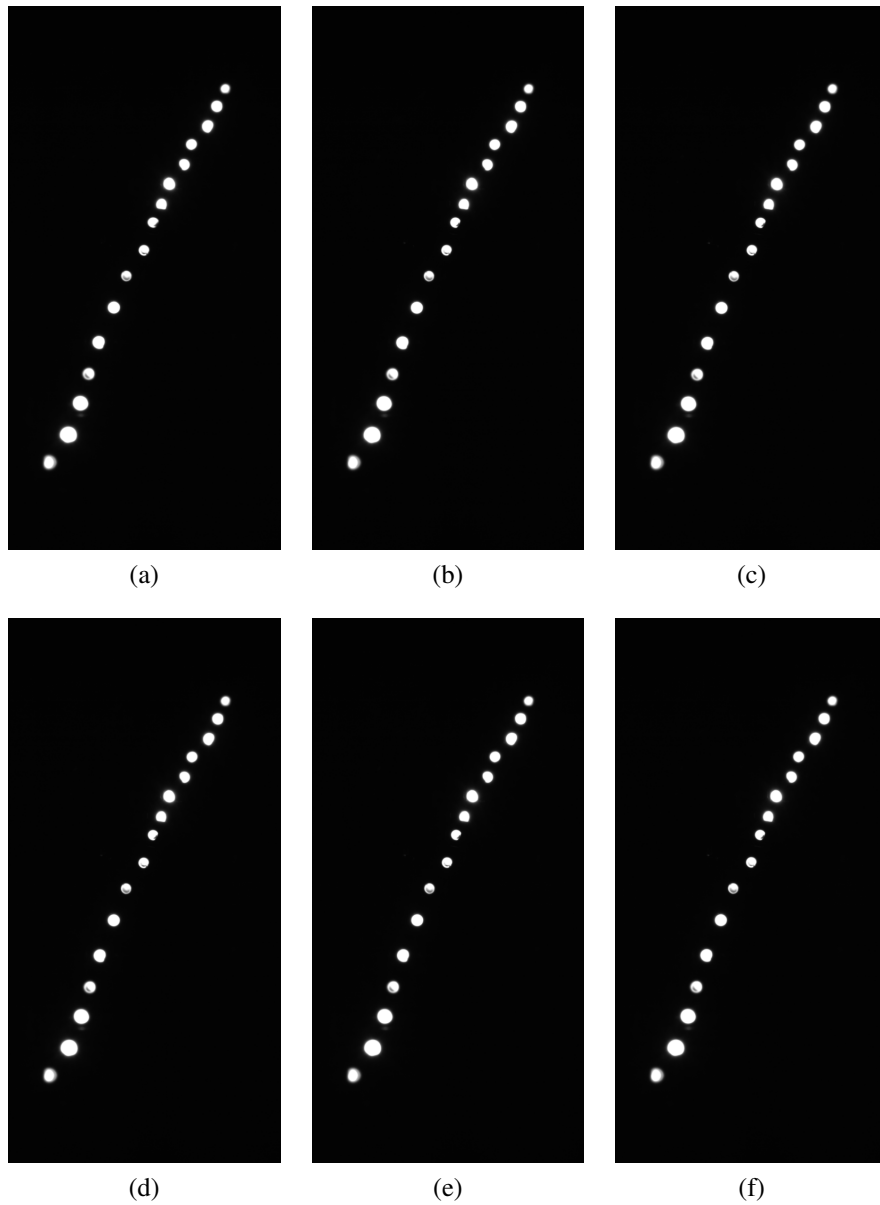
Figure 2.3: Captured frames of sixteen markers showing minute motion.

tion and 19.6875 Hz for vertical direction respectively. The rest of the natural vibration frequencies are most likely due to material characteristics which found in both vibration directions. The higher natural vibration frequency on vertical direction compared to one of lateral direction shows that the truss is more rigid vertically.
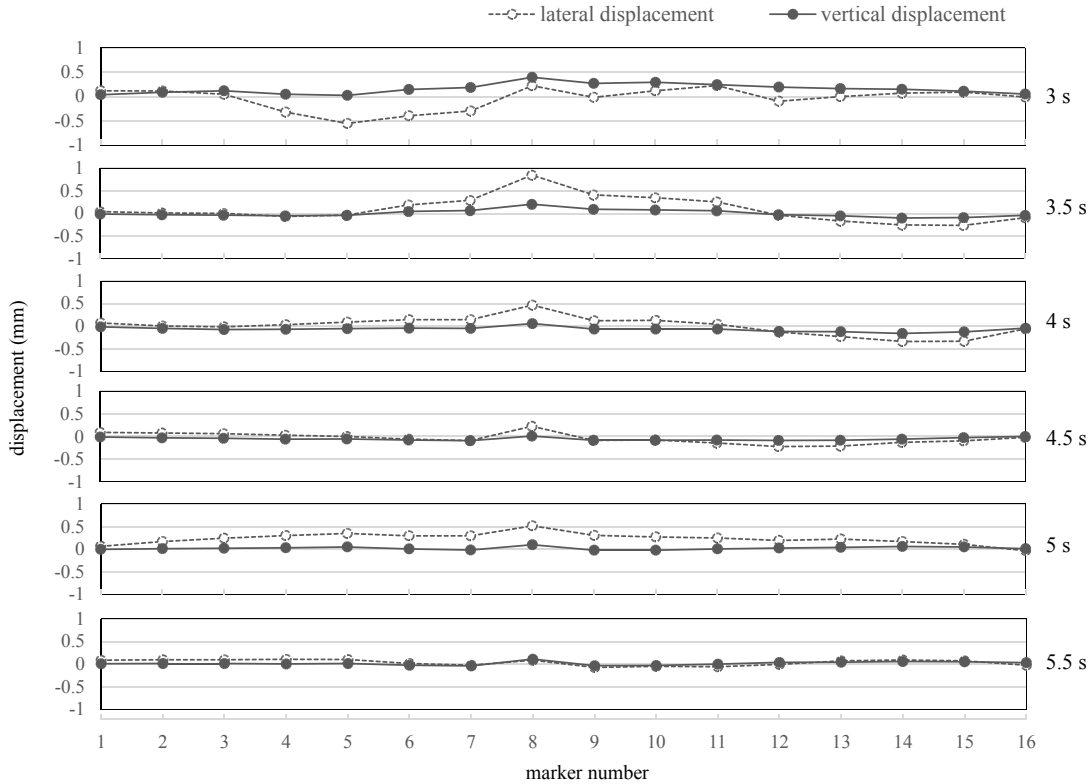
Figure 2.4: Chord displacement between t=3 s to t= 5.5 s.

Table 2.2: Natural vibration frequencies of the truss (LED experiment).

Direction	Natural frequencies (Hz)				
	Mode 1	Mode 2	Mode 3	Mode 4	Mode 5
Lateral	8.6133	15.2930	39.5508	41.8359	45.5273
Vertical	15.2930	19.6875	39.5508	41.8359	45.5273

2.4 Truss vibration experiment with corner cube prism

The previous experiment utilized LED as marker to provide a visual cue of the marker position, which implies power supply requirement for each marker [54]. This requirement is impractical for long term installation as the power requirement for each LED would be too high for long-distance measurement. Hence, a method with retro-flective optical prism marker with similar tandem alignment is proposed.

Corner cube prism has been demonstrated to be useful for displacement measurement with only lighting requirement at the optical sensor side. Arrangement of corner cube and pentagonal prism beam splitter has been demonstrated to be able to measure

(a)

(b)

(c)

(d)
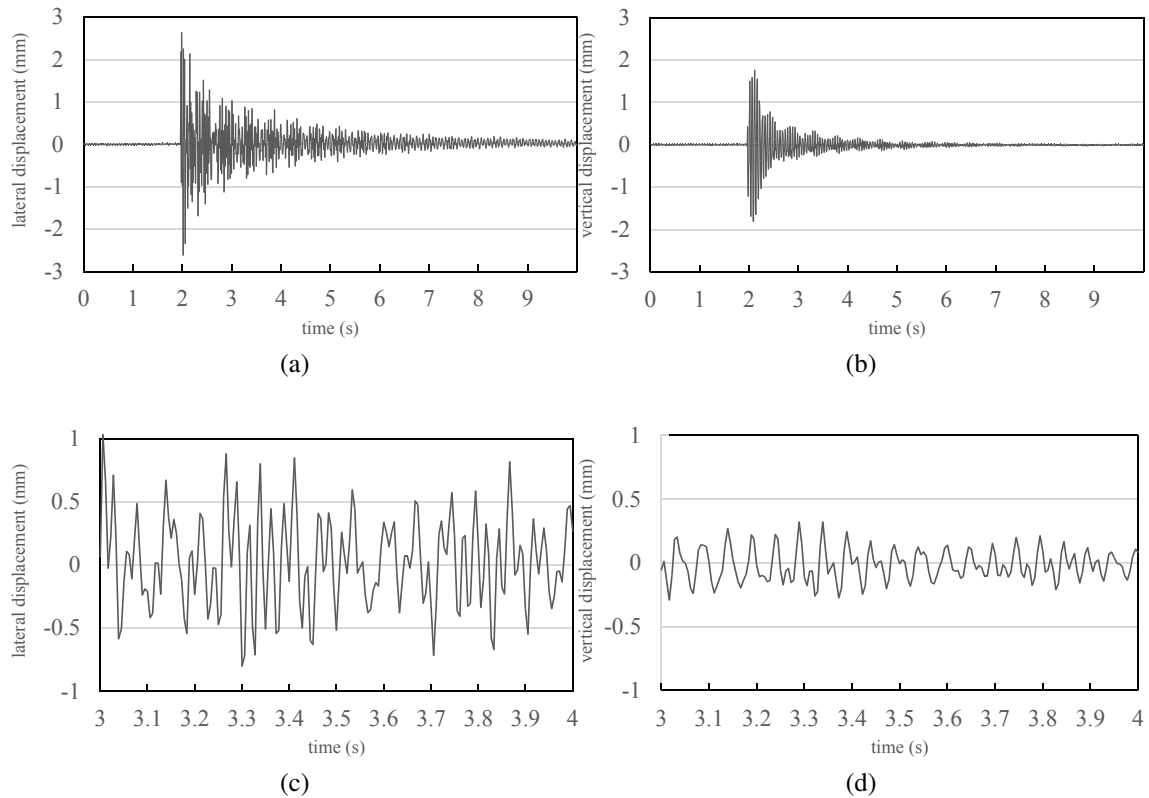
Figure 2.5: Lateral and vertical displacement at the center of the span (LED experiment).

roll angle change of a linear guide [55] at nanometer displacement accuracy from a distance of few centimeters [56]. Interferometer length measurement with two parallel laser beams was used to measure distance and lateral shift of corner cube prisms at micrometer resolution [57]. Such implementation is scalable towards longer distance with adequate lighting equipment and proper alignment.

Retro-reflective corner cube prism and coaxial lighting device were used to obtain high-contrast appearance of markers at long-distance measurement. Arrangement of coaxial lighting and corner cube as retro-reflective markers allows the high-contrast appearance of marker with only lighting apparatus at the side of the camera head. This arrangement is particularly useful when active lighting, such as LED, isn't practical for each marker. Usage of corner cube prism also implies perpendicularity between the camera head and marker, making displacement measurement more precise. Thus, the application of corner cube instead of LED as marker for structure displacement measurement
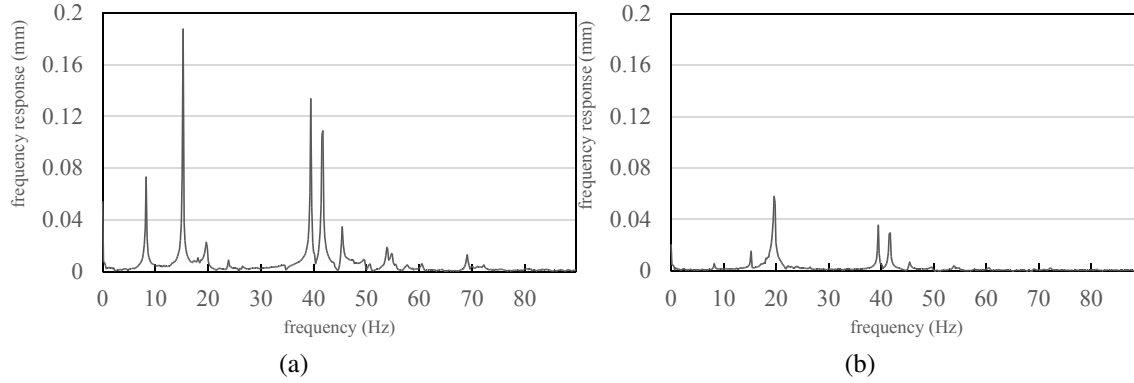
Figure 2.6: Normalized frequency response of the model bridge in lateral and vertical direction (LED experiment).

might be beneficial compared to LEDs or feature points on the structure.

2.4.1 Scaling factor with slant angle compensation

Scaling factor is needed to estimate actual physical displacement from the captured motion of markers from the images in vision system, taking into account sensor size and distance between camera. Prior to the measurement, scaling factor should be calculated independently for each marker considering the relative position of markers to the camera head.

General equation of lateral and vertical scaling factor for a marker perfectly perpendicular to the camera is given as:

$$C_l = \frac{V_w r}{f N_w}, \quad C_v = \frac{V_h r}{f N_h} \tag{2.6}$$

for C_l and C_v scaling factor for the lateral and vertical direction, f is lens focal length, r is the distance between camera and marker, V_w and V_h are camera sensor width and height with corresponding N_w and W_h pixel resolution, respectively. Figure 2.7 shows the relationship between marker and camera in Cartesian coordinate system with d_f, d_l, and d_v are frontal distance parallel to bridge axis, lateral distance, and vertical distance between camera head and marker.

Non-perpendicularity between camera sensor and corner cube prism markers may
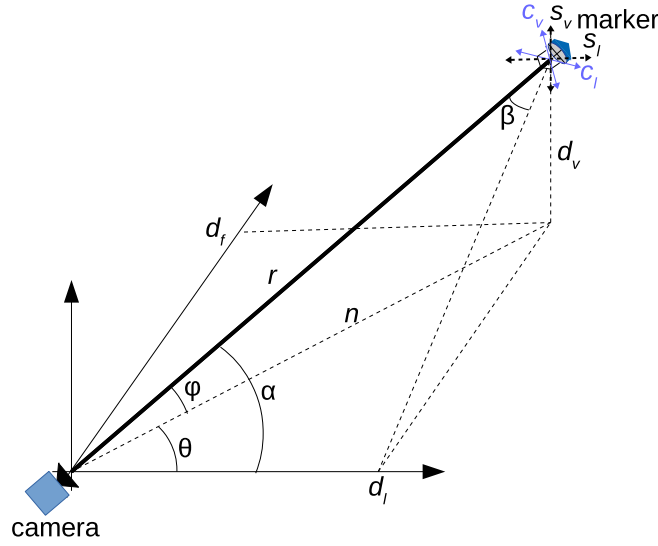
Figure 2.7: Camera and marker relationship in Cartesian coordinate system.

contribute to distortion in the captured image resulting in inaccurate scaling factor, hence scaling factor needs to compensate the probable lateral and vertical slant. For practical reasons such as placing the markers in a tandem alignment and eliminate occlusion between markers, the camera system's optical axis was placed slightly away from the general coordinate system of the structure.

These lateral and vertical slant angles resulted in non-perpendicularity between optical system and markers. Hence, Equation (2.6) can be then further expanded to accommodate slant angles:

$$SF_v = \frac{C_v}{cos(\phi)} \tag{2.7}$$

$$SF_l = \frac{C_l}{cos(\beta)} = \frac{C_l}{\sqrt{1 - sin^2\alpha}} = \frac{C_l}{\sqrt{1 - cos^2\theta cos^2\phi}} \tag{2.8}$$

with SF_l and SF_v are lateral and vertical scaling factor in respect to the structure's orientation. Figure 2.8 and 2.9 show the angular orientation of the markers in relation to the structure.

Several assumptions regarding the optical system, object alignment, and general
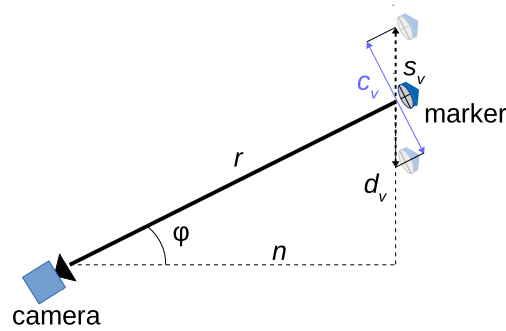
Figure 2.8: Vertical scaling factor.
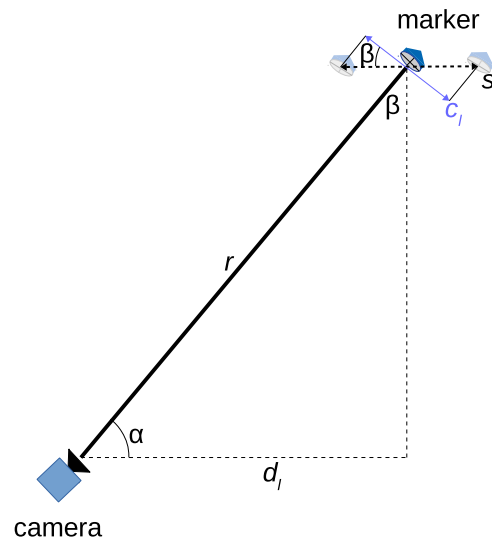
Figure 2.9: Lateral scaling factor.

coordinate alignment between the two are to be considered to obtain accurate lateral and vertical scaling factor estimation:

- no lens distortion throughout the whole width and height of field of view,

- no displacement of markers in the direction of bridge axis, i.e. axial displacement,

- all markers are directly perpendicular to the camera,

- bridge and camera are both parallel to the ground so that observed vertical displacement is totally separated lateral displacement.

Scaling factor can be calibrated prior to dynamics measurement using known marker size [49], known distance between markers [42], and pre-calibrated displacement [58].

Displacement calibration in the experiment to make sure that the calculated scaling factors are accurate was done using laser distance meter and translation optical jig.

2.4.2 Experiment setup

The same bridge model from LED experiment was used, with the addition of full deck from steel plates, as shown in Figure 2.10. Steel plates with 2.5 mm thickness were

Figure 2.10: Truss bridge model (corner cube prism experiment).

installed as the deck for the bridge model.

Nine optical corner cube markers were installed on one side of the lower chord of the bridge model: two at both anchorage points and the remaining seven at the chord members, as shown in Figure 2.11. Marker0 and marker8 were set as reference markers and expected not to have any notable displacement.

Summary of the vision system specification is described in Table 2.3. Camera resolution was cropped from the original 2048x2048 px to increase effective frame rate to 240 fps. In addition, focal length, aperture, and focus distance of the optical system need
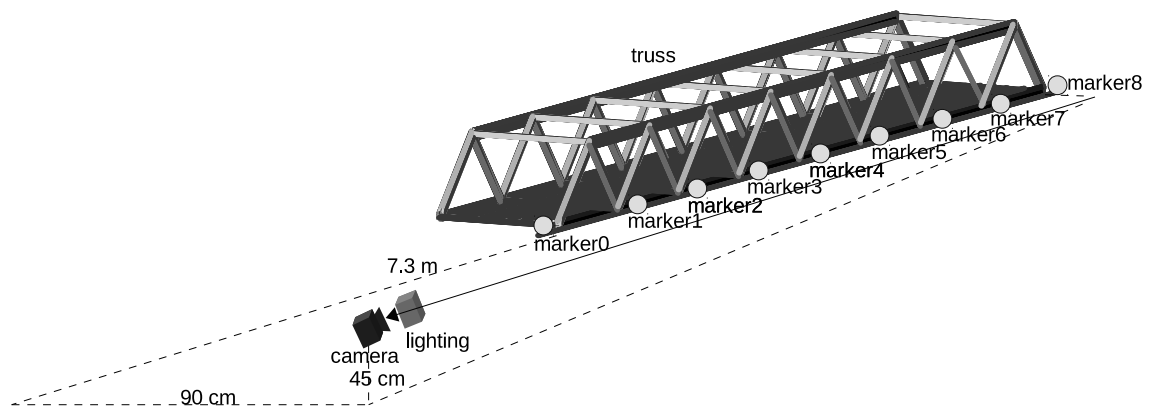
Figure 2.11: General setup of the vision system and marker placement on the truss (corner cube prism experiment).

to be adjusted proportionally to capture all the markers within field of the camera without excessive focal blur.

Table 2.3: Vision system specification (corner cube prism experiment).

Camera (Ximea MQ042MG-C)	Lens (SIGMA APO HSM 300-800)
Resolution: 2048x752 px (8-bit)	Focal length: 410 mm
Sensor: 5.5 μm pitch	Focus distance: 9.3 m
240 fps, 2 ms exposure	F/32 Aperture
Lighting	**Computer**
Coaxial Lighting FASTUS OPX-M100W	Dell Vostro 3558 (8 GB memory)
29 W, 6000 K color	OpenCV 3.3.1
Marker: Thorlabs PS974M-B 8$\varnothing$mm	Ubuntu 16.04.5 LTS

2.4.3 Results and discussion

2.4.3.1 Scaling Factor Calibration

The vertical scaling factor was calibrated by measuring pixel-wise displacement of set 10 mm vertical displacement of an optical jig of as shown in Figure 2.12. The vertical
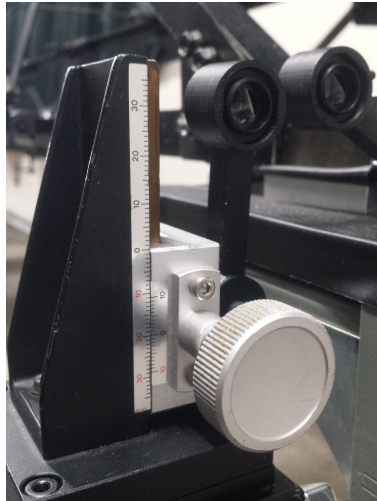
Figure 2.12: Markers attached to optical jig with set displacement.

alignment was verified using a digital protractor (DXL360S). The displacement of the optical jig was further verified using a laser displacement sensor (Keyence LK-G405).

The scaling factor for each marker from the calibration is shown in Table 2.4 taken into account the slant tilt angle between the camera head and marker. Maximum scaling

Table 2.4: Scaling factor calibration (corner cube prism experiment).

Frontal distance (mm)	Vertical distance (mm)	Displacement (mm)	Scaling factor (laser, mm/px)	Scaling factor (calculated, mm/px)	Error (%)
7100	600	9.9082	0.095975	0.095975	1.9717
7600	600	10.0874	0.102641	0.102641	2.2264
8100	600	9.9492	0.109313	0.109313	0.5868
8600	600	10.0604	0.115989	0.115989	1.2197
9100	550	10.0888	0.122584	0.122584	0.2921
9600	600	9.8121	0.129352	0.129352	2.4851
10100	600	10.0579	0.136038	0.136038	1.5811
10600	600	10.0490	0.142727	0.142727	3.5407
11100	600	10.0714	0.149417	0.149417	2.4212
11600	600	10.1691	0.156109	0.156109	3.2201

factor error was 3.5407%. Error-values were smaller at markers closer to focus distance (9.3 m) and bigger at markers further away from the focus distance at the center of the span.

2.4.3.2   Marker Motion Extraction

The camera system captured the motion of the corner cube optical prisms markers, aligned in tandem layout as shown in Figure 2.13. Each marker was able to be captured without occlusion between one another.

Centroid position of marker i was determined from the captured frames after grayscale binarization B with a threshold of 10 following:

$$M = \sum_{x,y} B_i(x, y) \tag{2.9}$$
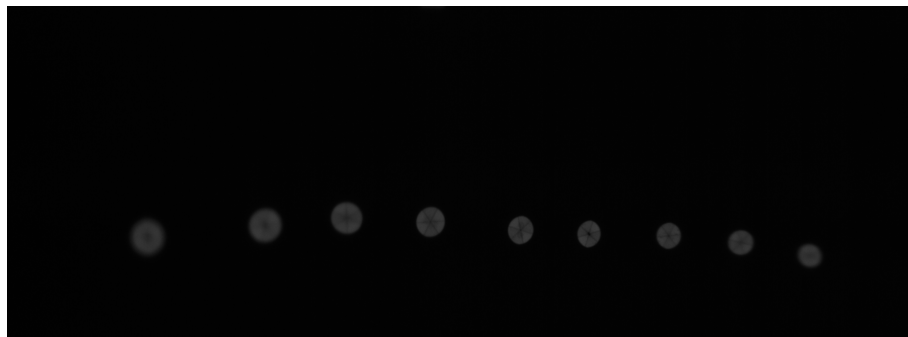
Figure 2.13: Frame of captured markers (rotated 90°clockwise).

$$M_x = \sum_{x,y} xB_i(x,y), \quad M_y = \sum_{x,y} yB_i(x,y) \tag{2.10}$$

$$(x_i, y_i) = (\frac{M_x}{M}, \frac{M_y}{M}) \tag{2.11}$$

with x and y of each marker is set within its respective marker's region of interest.

2.4.3.3 Truss Bridge Model Dynamics Measurement

Displacement measurement obtained from the vision system was calibrated against a set of accelerometer (RION PV-87 piezo accelerometer unit, RION UV-15 vibration signal conditioner). The accelerometer sampled only vertical displacement at 480 Hz, twice the frame rate of the vision system. Excitation was done from impulse strike from the top at the center of the span of the truss bridge model.
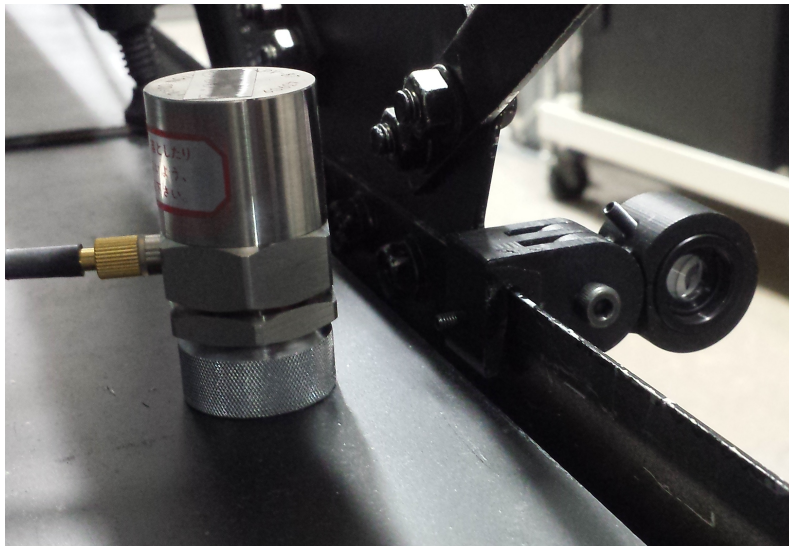
Figure 2.14: Placement of piezo accelerometer pickup and corner cube marker.

Given that the corner cube optical marker and accelerometer were not placed exactly at the same position as shown in Figure 2.14, displacement value from the vision system and accelerometer would have different amplitude.

Figure 2.15 shows displacement of Marker3 obtained from the vision system and accelerometer, the value from accelerometer is multiplied 5x for clarity. The displacement value from vision system and accelerometer differed slightly just after the initial impulse excitation, then dislacement signals well agreed in terms of phase towards the end of the free damped vibration.
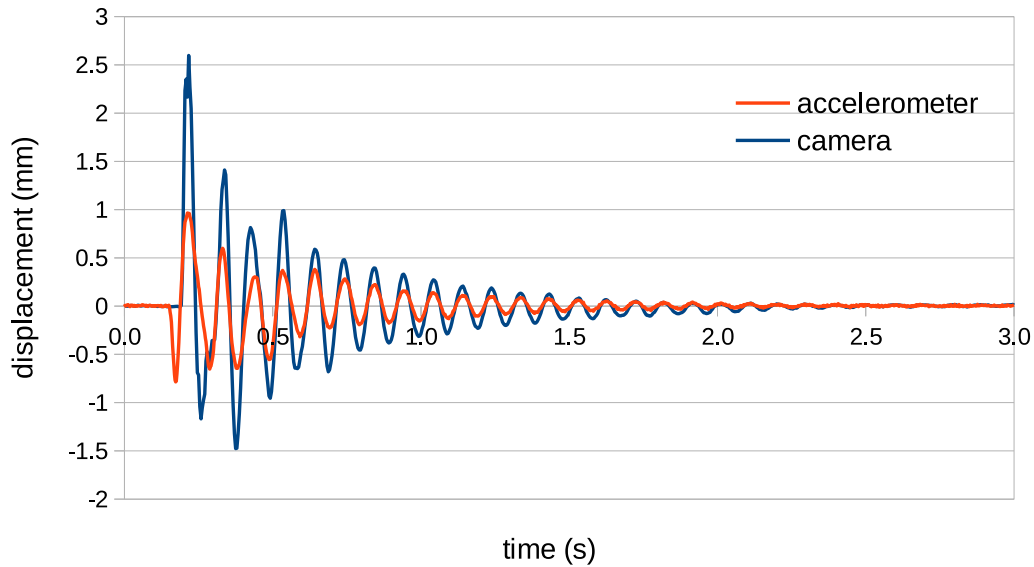
Figure 2.15: Marker3 vertical displacement values from accelerometer and vision system.

2.4.3.4   Natural Frequency and Damping Ratio

Simple Fourier transform was used to evaluate natural frequencies and damping variations of the truss bridge model from short-time impulse excitation [59]. The half-power method was used to evaluate modal damping of the structure [60] from each peak in frequency response from Fourier transform with the bandwidth shown in Figure 2.16, described as:

$$\zeta = \frac{f_2 - f_1}{2f_0} \tag{2.12}$$

of which the damping ratio is calculated from the frequency peak and the frequency band of which the signal level reaches its half power.

Table 2.5 shows the frequencies whose peaks appears at all the moving markers and
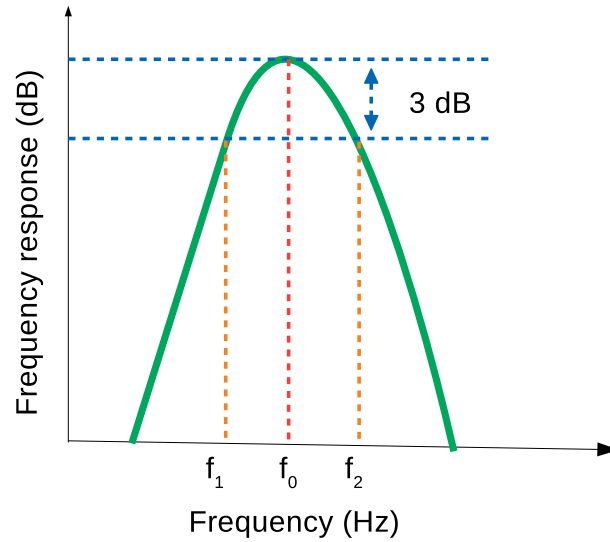
Figure 2.16: Half-power method for damping estimation.

the corresponding damping ratio. Frequency peaks apparent at all markers were picked with the corresponding damping ratios. Average first-mode natural frequency and damping ratio from the measurement points were 15.6 Hz and 0.0423 for lateral direction; 9.9 Hz and 0.0685 for vertical direction. The structure has different lateral and vertical frequencies, implying the natural frequencies contributed by the structural configuration rather by the material of the members. Vertical damping ratio at all markers were generally higher compared to ones of lateral direction, implying that the structure is stiffer in vertical direction for vertical load bearing capacity.

Table 2.5: Natural frequencies and damping ratio of the truss bridge model (corner cube prism experiment).

Marker Number	Lateral Natural Frequency (Hz)	Lateral Damping Ratio	Vertical Natural Frequency (Hz)	Vertical Damping Ratio
1	15.6	0.04167	10	0.07000
2	16	0.04274	9.7	0.07216
3	15.6	0.04140	9.9	0.06566
4	15.5	0.04839	9.9	0.07071
5	15.6	0.04487	10	0.06500
6	15.6	0.03846	9.9	0.06566
7	15.6	0.03846	10	0.07000

2.5 Conclusions

High-speed vision system was demonstrated to be able to concurrently measure dynamic lateral and vertical displacement of multiple markers installed on a bridge model, using both LED and corner cube prism as markers installed on the structural members. The accuracy of the measured displacement was within 4% error with working distance between 7 and 12 meter.

Subsequent frequency analysis was carried out by peak-picking method to identify the natural vibration frequencies and half-power method to estimate the corresponding damping ratios. The analysis was carried out separately on lateral and vertical direction. Such analysis may serve as a baseline to estimate the structural integrity of a bridge.

Several improvements could be made to the experiment:

- longer capture duration until the vibration signal reaches steady state again after excitation to find for any residual plastic displacement and to obtain higher FFT resolution,

- stronger lighting equipment for longer distance application,

- compensation of the camera head movement using fiducial marker,

- higher sampling rate for more precise modal characteristics estimation,

- provision to measure torsional displacement of the bridge deck by capturing distributed displacement at both sides of the bridge.

Chapter 3

Motion Capture Method with Tandem-marker for Dynamic Distributed Displacement Analysis

3.1   Introduction

A novel vision-based measurement method is proposed for capturing small structural dynamic displacements at multiple points simultaneously on a large-scale structure. The measurement points are to be aligned along the depth of field of the vision system so that all points are observable in a single field of view of a telephoto lens. To cope with low incident light and focal blur due to the long distance and high magnification, highly retro-reflective corner cube prisms are utilized as motion markers combined with a strong coaxial lighting device next to the vision system. This allows for measuring displacements of markers with tandem-layout in the captured image without decreasing measurement resolution compared to side-view alignment.

The placement of the vision system facilitates simultaneous measurement of lateral and vertical displacement. The arrangement of half-mirror from the coaxial lighting and plate mirror allows capturing collimated marker motion on both sides of the structure. This extends the vision system capability to also capture torsional displacement of the structure.

Deformation of the bridge model, its resonant frequencies, and the corresponding mode shapes at a frequency of tens of Hz can be determined by analyzing marker motion images captured and deriving the displacement of each marker using specific pre-calculated scaling factor ratio.

3.1.1 Current limitations of vision-based displacement measurement

In order to determine dynamic displacements on large-scale structures from long distance, many vision-based structural health monitoring systems using digital video cameras have been used to inspect structures [42, 51, 61–65]. Different approaches of vision-based structural health monitoring have been studied regarding structural members to be measured, marker feature identification, displacement extraction algorithm, types of structure construction, i.e. cable vibration measurements [66, 67], large-scale bridge monitoring with illuminated LED targets [68], railway bridge inspection using digital image correlation (DIC) [69], cantilever beam measurements using Hough transform [70], robust object searching pattern-marker determination [71], large-scale structure monitoring with rotational angle measurement [72].

Many DIC studies have addressed with small displacement measurements with sub-pixel accuracy [73–77]. As the pixel pitch and size of the image sensor determines the displacement measurement accuracy in vision-based approaches, there is apparent measurement spatial resolution trade-off related to the measurement distance and the breadth of the field of view. The image correlation criteria employed in the analysis are also susceptible to image degradation due to shadows and heat haze [78].

Application of pan-tilt mechanism from an galvanomirror, using a single high speed mechanical tracking camera that can function as multiple virtual cameras by switching views multiple times in a second, can be employed to obtain wider field of view without reducing the measurement's spatial resolution and acquire small displacement distribution and vibration sensing of a bridge model [17]. Setup with galvanomirror pan-tilt mechanism was able to expand the field of view came at the cost of the reduced effective sampling rate of each measurement point and the possibility of measurement drift due to camera head self vibration [79]. The position of the camera perpendicular to the side of the bridge also prohibits the measurement of lateral displacement of the structure.

Using a single camera to simultaneously measure dynamic displacements at many points on a large-scale structure of tens or hundreds of meters is quite difficult. For simultaneous multi-point displacement measurements, several multi-camera approaches have

been reported for large-scale structure inspection [52, 72, 80–83]. But such approach require proper synchronization and determination of common reference points between the cameras. In addition, installation of multiple cameras in situ is cumbersome and time-consuming due to multiple

High frame rate (HFR) video-based implementations have also been reported for structural vibration analyses at hundreds or thousands of Hz [84–90]. But the short exposure time for each frame, exacerbated by the narrow aperture of the lens, limits the effective distance of the measurement due to the insufficient light reaching the camera sensor.

3.1.2   Torsional displacement

Torsional displacement refers to the change of the bridge' deck orientation along the radius of the bridge's axis. This occurs when the two chords of the bridge exhibit different amplitude of vibration. The torsional displacement is more notable in long-suspension bridges noting the more flexible vertical members and the prevalence of suspension bridge location in wind -prone areas [91].

Low frequency sound pressure noise on a bridge was found to be more severe from vehicles passing in the outer slower lane compared to the faster inner passing lane, because of the torsional displacement [92]. Change of natural frequency of diagonal members of a truss bridge due to the local damage from corrosion could not be reliably detected in vertical and lateral direction, but the notable frequency drop can be recognized in the torsional modes. [10] Such issues indicate the importance of the three-dimensional analysis, including torsional displacement of traffic-induced bridge vibration

Vertical and torsional displacement and their modal modal frequencies are similarly coupled, but torsional component often have higher frequency compared to the vertical frequency [93]. Torsional displacement and its associated frequency response functions can be constructed from the combination of acquired vibration in vertical and lateral direction, this was demonstrated using large-size eccentric mass shakers at different forcing levels [94].

3.2   Proposed system

3.2.1   Issues in current vision-based systems

Vision-based structural displacement measurement systems have been previously used for structural inspection of bridges. The systems are often implemented using commercial digital cameras operating at tens of frames per second. Although this enable low-cost and flexible installation on the structure to be inspected, most of them have been limited to only local displacement measurements at a specific point on a large-scale bridge. Several problems still remain to be solved for practical bridge inspection, including locating displacement measurements at many points on a large-scale structure, as illustrated in Figure 3.1.
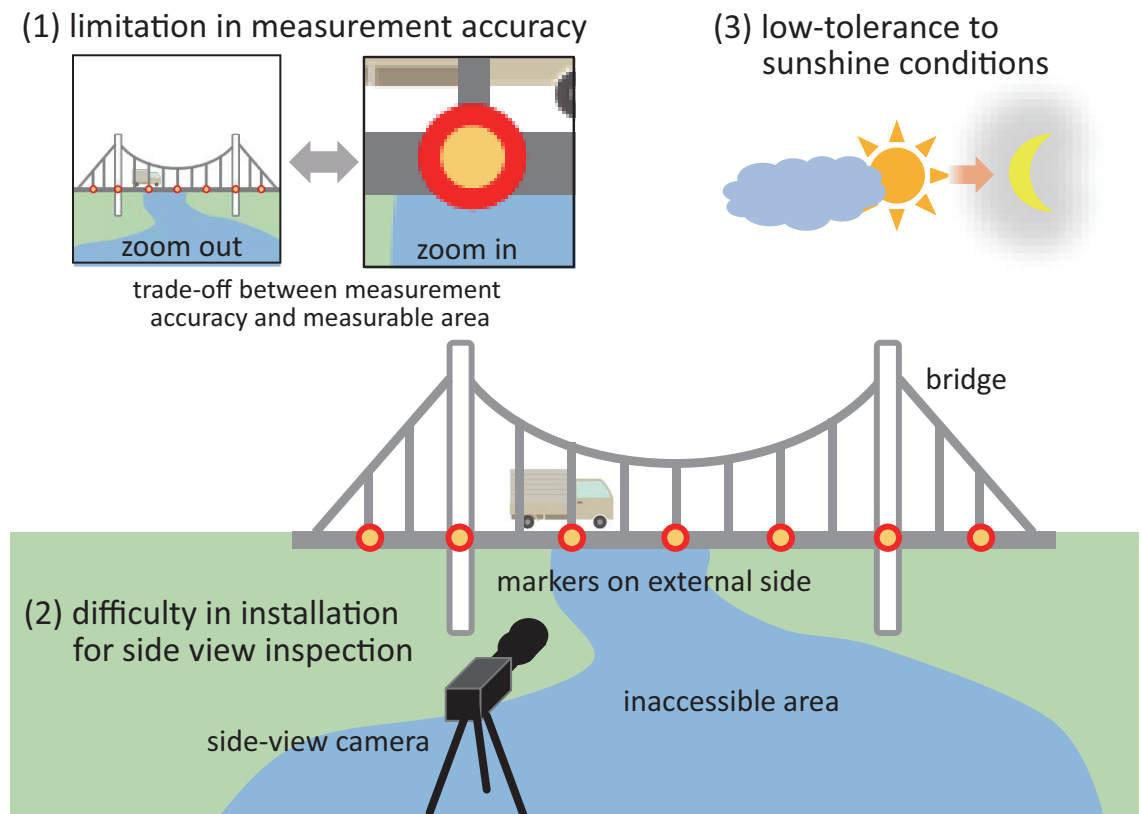
Figure 3.1: Current problems in vision-based bridge deflection measurements.

- Limitation in measurement accuracy.

  When a camera is used to capture side-view images of the bridge in its axial-vertical plane, the camera magnification should be lowered to observe all points within a

single camera view. There is a trade-off between the measurement accuracy and measurable area of the camera due to the limited number of pixels integrated on the image sensor. For example, when the side-view image of a 100 m long bridge is captured with a high-resolution 16 megapixel digital camera, one pixel corresponds to 25 mm. This is far from the sub-millimeter accuracy required for bridge inspection, and this is the reason that vision-based approaches have been limited for local deflection measurement.

- Installation difficulty for side-view inspection.

Most of the existing bridges were constructed in inaccessible areas such as rivers, valleys, and seas, and the installation of a camera in such inaccessible areas makes capturing side-view images of the bridge very difficult. Patterned markers are often attached on the bridge to be inspected and provide accurate deflection measurements in vision-based approaches (e.g., DIC methods), whereas the marker attachment for side-view inspection may increase the amount of labor required for installation. The markers should be attached to the external side of the bridge, where it is not easy to access, thus all markers should be observable without occlusion by a camera installed at a certain distance from the side of the bridge.

- Low tolerance to external lighting conditions.

In general, vision-based approaches are not so robust to changes in light conditions from the environment, e.g. sunshine, cloud, etc. They are often not suitable without any active illumination at night when sunshine is not available. Active markers which emit light and remote illuminators which shine light on the measurement points have often been used for vision-based displacement measurements in low light condition. However, they are difficult to install when a camera system is located tens or hundreds of meters from the bridge to be inspected. Strong light emitting active markers and illuminators are required for long-distance measurements, as well as a large aperture zoom lens that enables image capture with large magnification and high sensitivity.

3.2.2   Concept of the proposed system

The proposed system assumes that the measurement points are aligned along the depth direction, and this tandem layout of measurement points enables the observation of all points in a single camera view without lowering the lens magnification. In addition, video capture with very low image intensity and a certain blur circle diameter should be permissible for small displacement measurements within a specified depth of field from large magnification telephoto lens.

Vision-based approach has issues regarding measurement accuracy and system installation when measuring the distributed displacement of a bridge by capturing from its side-view. The front of the bridge parallel to its axis is generally open and accessible along the road direction compared to the inaccessible areas at the side of a bridge, and the installation of a camera at the front of the bridge is much easier than at its side. A camera installed at the front should have a large depth of field along the road direction and large magnification to precisely measure distributed displacements at multiple points along the bridge from a single camera view, whereas the narrow lens aperture for a large depth of field results in underexposed images due to insufficient incident light. If low incident light and image degradation with a certain blur circle diameter are permissible when capturing front-view images with large magnification, the management and installation cost of a vision-based measurement system could be remarkably reduced.

A tandem marker-based motion capture method is proposed to measure displacements at many retroreflective markers attached to a large-scale structure, such that all markers are observed in front-view images with large magnification. Figure 3.2 shows the concept of tandem marker-based motion capture. The features are summarized as follows.

- Corner cubes as retroreflective markers

  The focal length and aperture (F-value) of the lens are set to large values that all the distant markers, which are distributed on a structure along the optical axis of the camera lens, can be precisely observed in a single camera view. Focal length and aperture determine the magnification ratio and the depth of field of the cam-
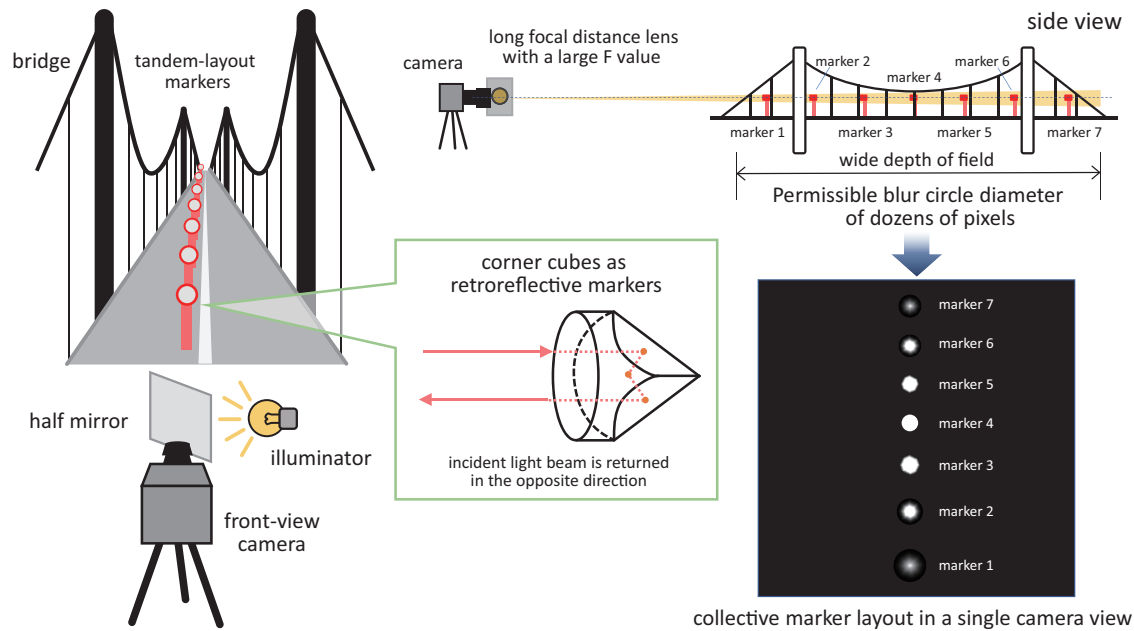
Figure 3.2: Concept of tandem marker-based motion capture.

era, respectively. The incident light intensity varies in proportion to the inverse square of the aperture, and the image intensity becomes much smaller as the aperture becomes narrower. To cope with the insufficient incident light at a narrow aperture, circle-shape corner cubes prisms are utilized as high-reflectance retroreflective markers for tandem marker-based motion capture. These markers were used in combination with a strong coaxial lighting device that emits light along the optical axis of the camera lens by diverting the light via a half mirror. However, there remains the problem of insufficient image intensity when the aperture is very narrow.

- Permissible blur circle diameter

Many commercial telephoto lenses have limitations regarding the size of their aperture due to difficulties in the precise design of the mechanism, as well as insufficient image intensity due to lens aberration. Considering such constraints in setting F values, some amount of lens focal blur should be permissible when capturing the input images on the assumption that the accuracy of the localization markers is not significantly reduced by image degradation due to the focal blur. The depth of field

is extendable by permitting a blur circle diameter of tens of pixels, which is much larger than that of one pixel or less in standard image capture which utilizes optimum focus distance at the specified marker. Generally, focus blur is expressed as a circular symmetric point spread function, and the center position of the marker is invariant to the degree of the focal blur when the markers are circular. Thus, tandem marker-based motion capture can be accurately performed using circle-shape corner cubes as markers, even if the input images are degraded with focal blur.

- Collective marker layout in a single camera view

  As the magnification of the camera increases using the longer focal length, the field of view of the camera becomes narrower. Despite the increase of the measurement accuracy, tt becomes difficult to observe multiple objects in a single camera view when the measurement points are distributed in a wide area. This is due to the limited number of pixels on the image sensor. During tandem marker-based motion capture, the markers should be well distributed along the optical axis such that all the markers are collectively observed in a narrow field of view without lowering the camera magnification. The diameter of the markers and the margin between markers are parameters that determine the number of measurable markers in a single camera view. The markers' displacement in the horizontal and vertical directions are measured with estimated center positions in the image with regards to the respective distances from the markers to the camera along the depth direction.

3.2.3 Measurable optical conditions and parameters

Most of depth of field calculation consider prismatic depth of field with a planar field of view which leads to inconsistent description of depth of field. Spherical cone depth of field is adopted to more accurately model depth of field distance between camera and object, thus consequently, the scaling factor.

The relationship between the permissible blur circle diameter and the depth of field in tandem marker-based motion capture can be described with the distance D where the camera is best-focused and sufficiently larger than the focal length f of the camera lens.

Depth of field ΔD with a permissible blur circle diameter ε can be approximated as follows:

$$\Delta D = D_F - D_N = \frac{2\varepsilon f^2 F D^2}{f^4 - \varepsilon^2 F^2 D^2} \tag{3.1}$$

$$D_N = D - \frac{\varepsilon F D^2}{f^2 + \varepsilon F D} \tag{3.2}$$

$$D_F = D + \frac{\varepsilon F D^2}{f^2 - \varepsilon F D} \tag{3.3}$$

where D_N and D_F are the depth of field near limit and the depth of field far limit, respectively.
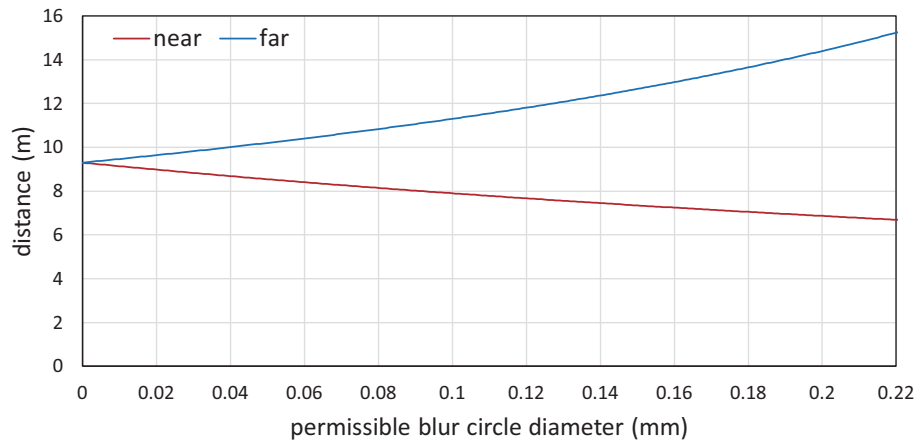
(a)
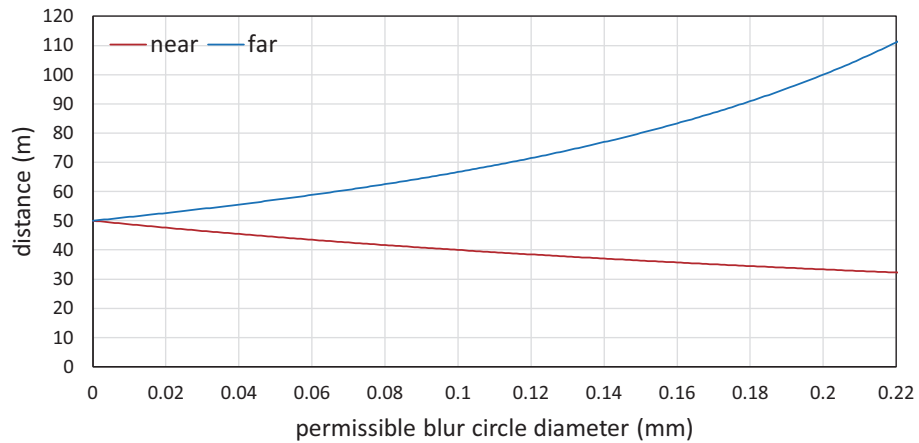
(b)

Figure 3.3: Relationship between permissible blur circle diameter and depth of field near and far limits.

Figure 3.3 shows the relationship between the permissible blur circle diameter ε and the depth of field near/far limits D_N and D_F when $f = 410$ mm, $F = 32$, and $D = 9.3$ m (a) applied for 4 m-long bridge model , and $f = 800$ mm, $F = 32$, and $D = 50$ m (b) applied for 20 m-long bridge observed at 50 m distance, summarized in Table 3.1.

Table 3.1: Optical parameters for bridge model and actual bridge.

	Bridge model	Actual bridge
Focal length (f)	410 mm	800 mm
Aperture (F)	F/32	F/32
Focus distance (D)	9.3 m	50 m
Pixel resolution	0.125 mm/pixel	0.344 mm/pixel
Blur circle diameter	10 pixel	40 pixel

Compared to the the depth of fields when only sharpest focus is allowed ($\varepsilon=1$ pixel), using larger permissible blur circle diameter resulted in the longer depth of field by the factor of 11.1× and 51.9× for the bridge model; 11.2× and 63.1× for the actual bridge; respectively for 10 pixel and 40 pixel permissible blur circle diameter, as shown in Table 3.2. The increased depth of field can be optimized to cover only the distance between the nearest and the furthest markers.

The observed diameters and positions of the retro-reflective markers projected on the image sensor plane can then be accurately extracted without overlapping. It is assumed that N corner cubes prisms of the diameter Φ are used for the markers, and the i-th marker ($i = 0, \cdots , N - 1$) is located at a distance D_i from a camera with focal length f and aperture F. The orientations of all the markers are perpendicular to the camera sensor along its optical axis, such that their projections on the image sensor are circular.

Table 3.2: Depth of field with varying permissible blur circle diameter.

Blur circle diameter (ε)	1 pixel (5.5 μm)	10 pixels (0.055 mm)	40 pixels (0.22 mm)
Bridge model ($D = 9.3$ m)			
Near limit (D_N, m)	9.22	8.47	6.69
Far limit (D_F, m)	9.38	10.30	15.23
Depth of field (m)	0.16	1.83	8.54
Actual bridge ($D = 50$ m)			
Near limit (D_N, m)	49.38	43.96	32.26
Far limit (D_F, m)	50.63	57.87	111.11
Depth of field (m)	1.25	14.01	78.85

When the image is focused at a distance D from the camera, the blur circle diameter $\varepsilon(d)$ is given as

$$\varepsilon(d) = \frac{f^2}{F} \cdot \frac{|D - d|}{d(D - f)}. \tag{3.4}$$

Considering the permissible blur circle diameter, the apparent diameter of the i-th marker projected in the image sensor plane is defined as

$$\phi_i = \frac{f}{D_i}\Phi + \varepsilon(D_i) = f\left(\frac{\Phi}{D_i} + \frac{f|D_i - d|}{Fd(D_i - f)}\right). \tag{3.5}$$

Figure 3.4 shows the relationship between the apparent marker diameter and its distance from the camera when (a) $f = 410$ mm, $F = 32$, $D = 9.3$ m, and $\Phi = 8$ mm, and (b) $f = 800$ mm, $F = 32$, $D = 50$ m, and $\Phi = 25$ mm. The observed marker diameter captured by a camera with 5.5-μm-pixel pitch image sensor is summarized in Table 3.3.

When all markers are captured in the input images, so as to satisfy the condition

$$|x_i - x_j| \geq \frac{\phi_i + \phi_j}{2}, \tag{3.6}$$

the apparent position of each marker can be correctly extracted without overlapping each other, with $x_i = (x_i, y_i)$ is the apparent position of the i-th marker in the image sensor plane. Given that all the markers are in the captured image from the 5.5-μm-pixel-pitch 2048×2048 image sensor, 18 or more markers can be positioned in a straight line without overlap between one another.

Table 3.3: Observed marker diameter.

	Bridge model (D = 7.3–11.3 m)	Actual bridge (D = 40–60 m)
Closest	111.1 pixel	109.4 pixel (0.602 mm)
Furthest	64.1 pixel (0.353 mm)	72.7 pixel (0.400 mm)
Actual marker diameter (Φ)	8 mm	25 mm
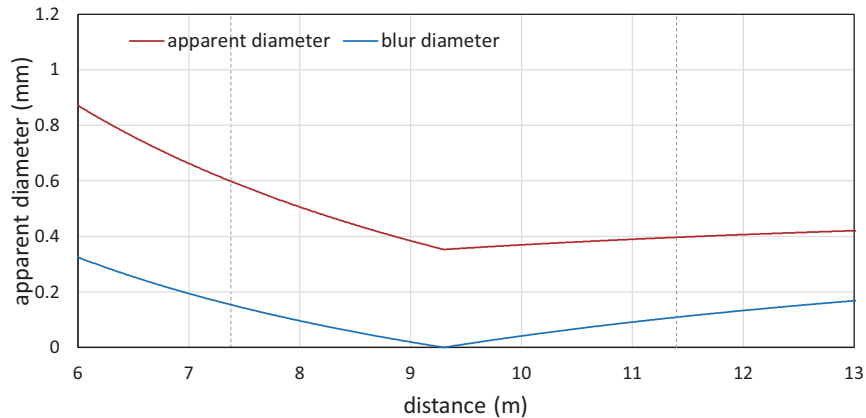
(a)
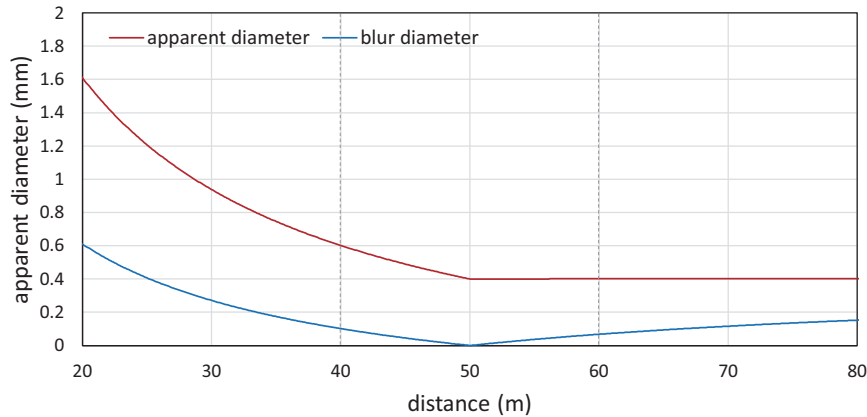
(b)

Figure 3.4: The apparent diameter of corner cube prism for bridge model and actual bridge.

3.3 Bridge model experiment

3.3.1 Test structure and marker configuration

Series of experiments were conducted to measure the dynamic displacement distributions for a 4 m long truss structure bridge model using a vision-based measurement system consisting of a single camera with large magnification, demonstrating the effectiveness of the tandem marker-based motion capture method. Figure 3.5 shows the geometric configuration of the bridge model to be inspected and the vision-based measurement system. Figure 3.6 shows the front view (a) and side view (b) of the bridge model used in the experiments.
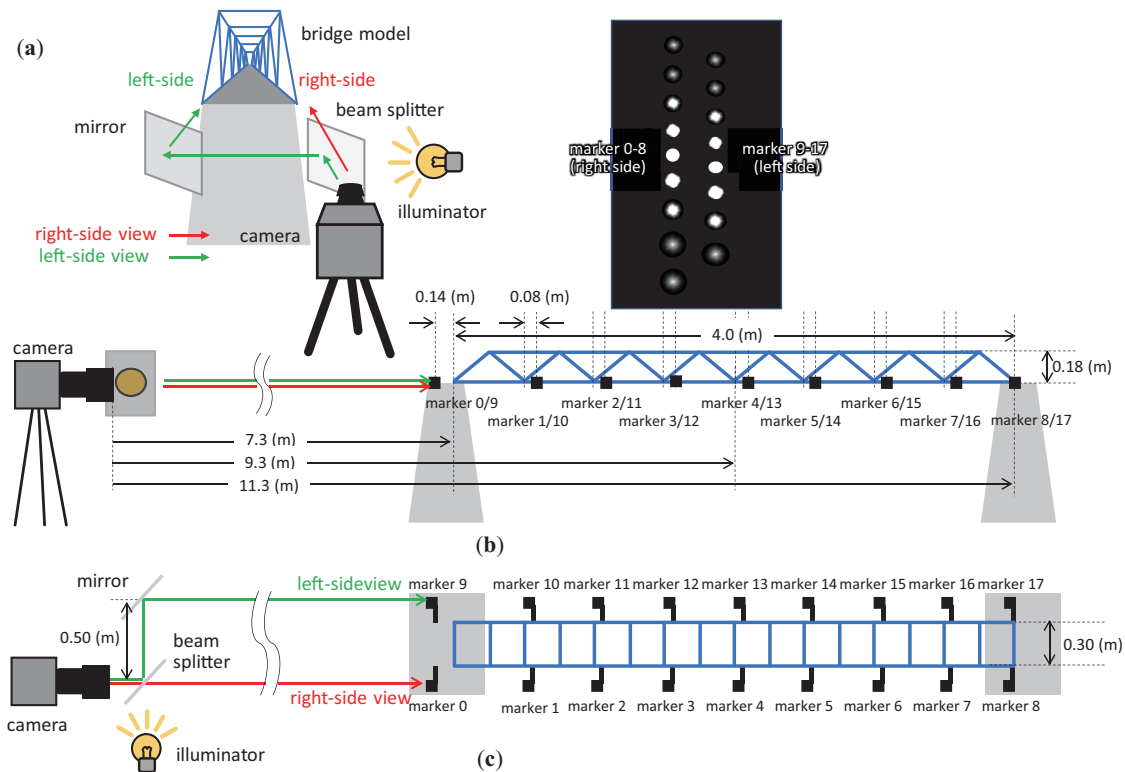
Figure 3.5: Geometric configuration in the bridge model experiment: front view, side view, and top view.

The length, height, and width of the bridge model are 4, 0.18, and 0.3 m, respectively, and the model was assembled as a Warren truss structure with 8 panels, L-25×25×1.2 mm L-type aluminum members for vertical chords, and FB-150×2 mm flat aluminum members for diagonal and horizontal chords. Both ends of the bridge model were fixed on 30 cm-high steel pedestals, which were fixed on the ground. The experiments were conducted with several steel plates (2945 g, 310×400 mm^2) to serve as the deck on the bridge model. Different numbers of steel plates (2, 4, 6, and 8) were installed on the bridge model in order to adjust its resonant frequency during the experiment as depicted in Figure 3.7.

As retro-reflective markers for tandem marker-based motion capture, eighteen corner cube prisms (PS974M-B, Thorlabs, Newton, NJ, US) were attached around the seven nodes between the eight lower panels and the fixed ends of each side of the bridge model. The effective diameter of the corner cube was $\Phi = 8.0$ mm. Each corner cube was installed
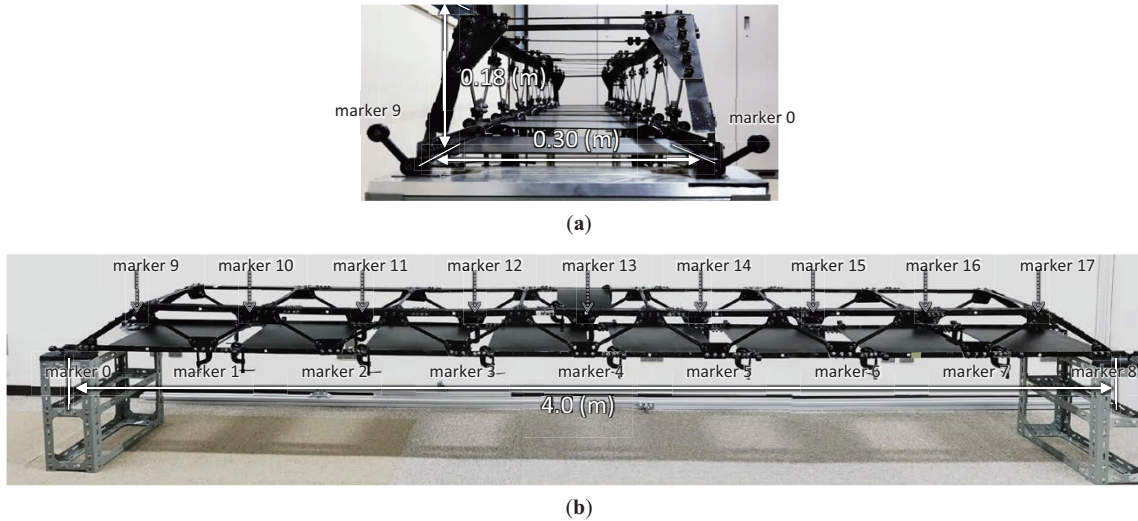
Figure 3.6: Bridge model overview: front and side view.

with 3D-printed jigs outside the bridge model so that its mirror faced the longitudinal direction of the bridge model, as depicted in Figure 3.8. The orientation of the two mirrors corresponds to the optical axis of the vision-based measurement system.

Markers 0, 8, 9, and 17 were attached with the 70 mm long jigs on the pedestals, markers 0 and 9 were located 0.14 m in ahead of the front end, and markers 8 and 17 were attached to the back end of the bridge model. The other markers were attached with 35 mm long jigs outside the bridge model; each marker was located 0.08 m behind the nearest node on the lower panels of the bridge model.

3.3.2 Vision system specification

The vision-based measurement system includes a USB 3.0 CMOS camera (MQ042MG-CM, Ximea, Münster, Germany), a zoom lens (APO 300-800 F5.6 EX HSM DGM, Sigma, Kawasaki, Japan), an LED illuminator (VLP-10500XP, LPL, Saitama, Japan), and a laptop PC with Ubuntu 14.04.11 (Latitude 3540, Dell, Round Rock, TX, US) for camera control. Figure 3.9 shows an overview of the vision-based measurement system.

The USB 3.0 camera mounted with the telephoto lens and metal-halide illuminator were installed on tripods (1.0 m-tall) so that they can horizontally observe the corner cubes prims markers. A 355×244 mm^2-plate beam splitter with 50/50 reflec-

(a)

(b)

(c)

(d)
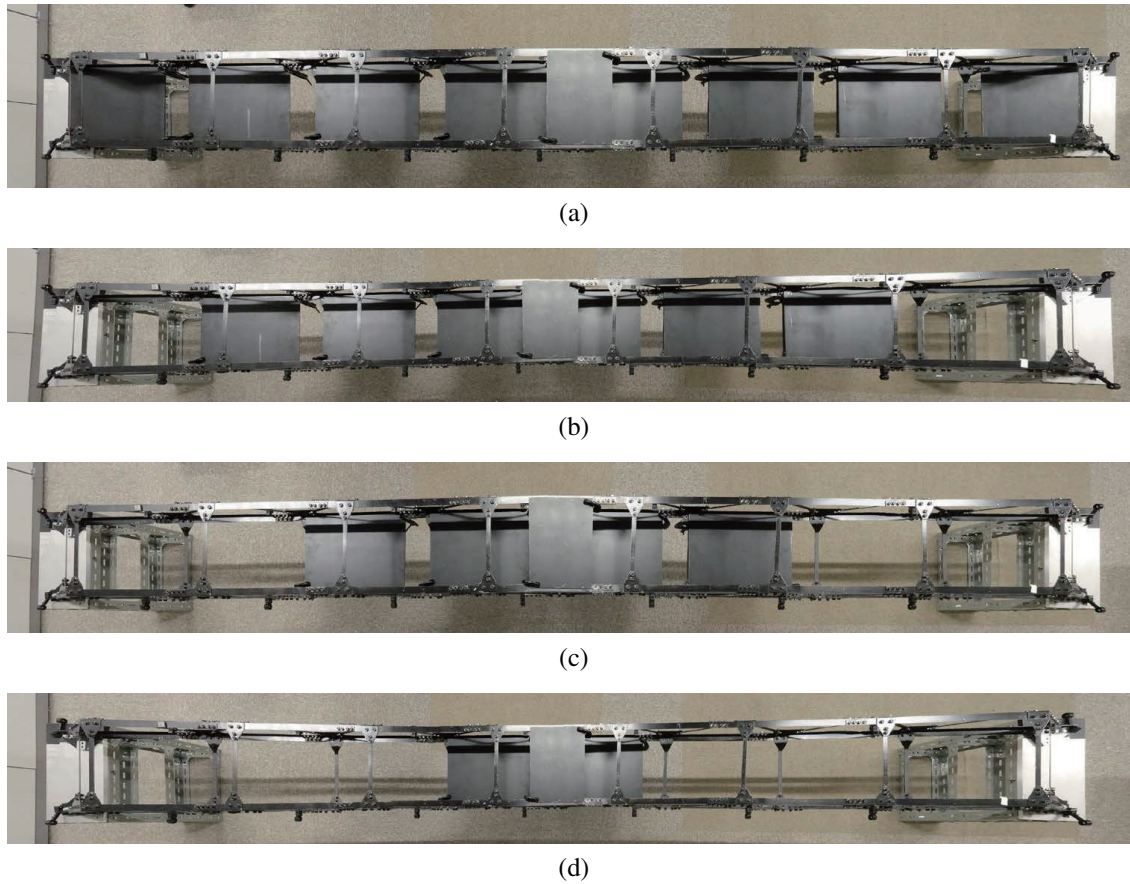
Figure 3.7: Top view of bridge with different number of decks.

tion/transmission ratio was installed 100 mm in front of the zoom lens so that the optical axis of the LED illuminator was aligned with that of the telephoto lens. Light emitted from the LED illuminator was diffused with a light diffuser film so that light reflected from a corner cube was observed with uniform intensity in the captured images.

In the bridge model experiments, the focal length and F value of the zoom lens were set to $f = 410$ mm and $F = 32$, respectively. The focus distance of the telephoto lens was set to $D = 9.30$ m. The distances from the telephoto lens to the front and back ends of the bridge model were 7.30 and 11.30 m, respectively. The depth of field is 8.54 m (from 6.69 to 15.23 m) when the permissible blur circle diameter was $\varepsilon = 0.22$ mm, which corresponds to 40 pixels in the image sensor. This allows all markers to be fully in the depth of field of the vision system.

The USB 3.0 camera (Ximea MQ042MG-CM) includes a 2048×2048 CMOS im-
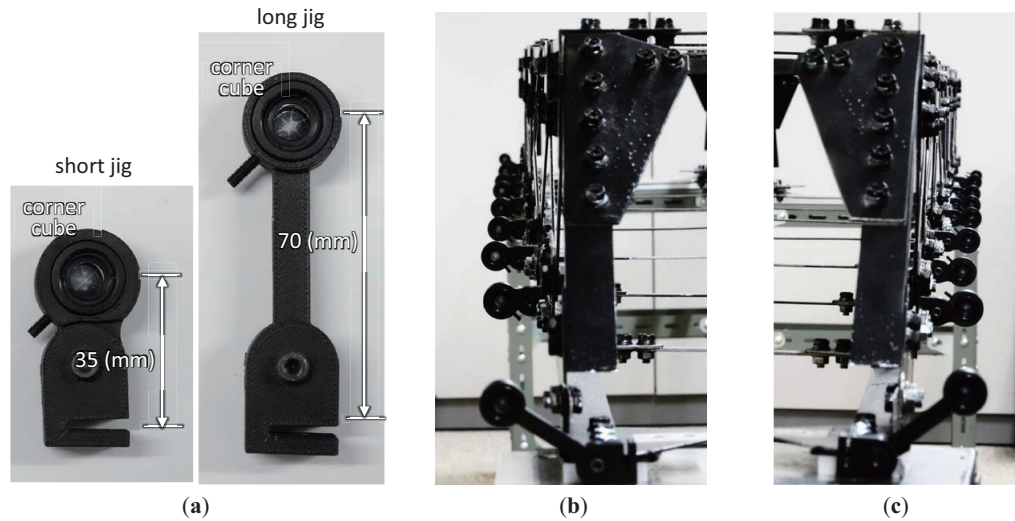
Figure 3.8: Corner cubes installed on a bridge model: attachment, right, and left side.
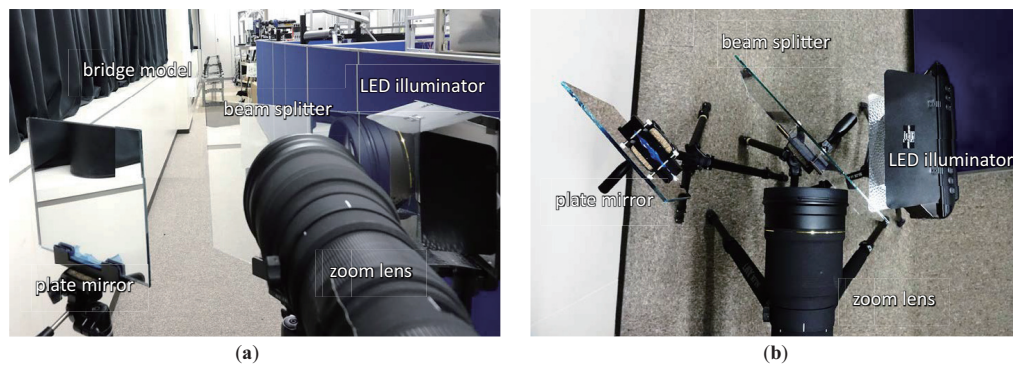
Figure 3.9: Vision-based measurement: general overview and top view.

age sensor with sensor and pixel sizes of 11.27×11.27 mm^2 and 5.5×5.5 μm^2 , respectively. The camera can capture and transfer 8-bit gray-level 752×2048 images to the PC via the USB 3.0 interface at 240 fps. At the front and back ends of the bridge model, which were located 7.30 and 11.30 m from the telephoto lens, one pixel corresponds to 0.098 and 0.152 mm, respectively. The measurement plane from the full frame of the captured image (752×2048 pixel) corresponds to 74×202 and 114×311 mm^2, respectively for the nearest and furthest marker.

In the experiments, the 355×244-mm^2 beam splitter and a 235×300-mm^2 plate mirror were installed 7 m in front of the right-front and left-front ends of the bridge model, respectively, as illustrated in Figure 3.5. This ensures that a single image with large magnification will include reflected light from 18 corner cubes at the left and right sides of

the bridge model, 9 markers on each side. The distance between the beam splitter and the plate mirror was set to 500 mm. The optical path lengths from the telephoto lens to the markers at the right side of the bridge model ranged from 7.095 to 11.229 m, whereas to those markers at the left side ranged from 7.594 to 11.729 m, respectively.

To obtain the apparent position of the i-th corner cube ($i = 0, \cdots, 17$) in the input image $I(x, y)$, the region of interest image $I_i(x, y)$ cropped from the input image for the i-th corner cube was considered. The center position (x_i, y_i) and diameter ϕ_i of the bright pixels of the i-th corner cube were estimated by computing the moment features of a binary image $B_i(x, y)$. This was obtained by binarizing the region of interest sub-images $I_i(x, y)$ with a threshold θ_i as follows:

$$(x_i, y_i) = (M_{10}/M_{00}, M_{01}/M_{00}) \tag{3.7}$$

$$\Phi_i = \frac{2}{\sqrt{\pi}} \sqrt{M_{00}} = 1.128 \sqrt{M_{00}}, \tag{3.8}$$

$$M_{00} = \sum_{x,y} B_i(x, y) \tag{3.9}$$

$$M_{10} = \sum_{x,y} x B_i(x, y) \tag{3.10}$$

$$M_{01} = \sum_{x,y} y B_i(x, y) \tag{3.11}$$

where we assume that the bright pixels in the i-th marker were only observed in $I_i(x, y)$, whereas those from any other corner cubes were not involved in the region of interest for the i-th marker.

3.3.3 Preliminary evaluation and calibration

To confirm the practical depth of field and verify the relationship between permissible focal blur and the distance from the telephoto lens to each corner cube prisms, images of the markers were then captured during no vibration occurring on the bridge model. Figure 3.10 shows 752×2048 input image with exposure time of 100 ms with the LED illuminator turned off (a), 752×2048 input image with exposure time of 2 ms with the LED illuminator turned on (b), and 150×150 images of the 18 corner cubes (c) cropped

from the input image.
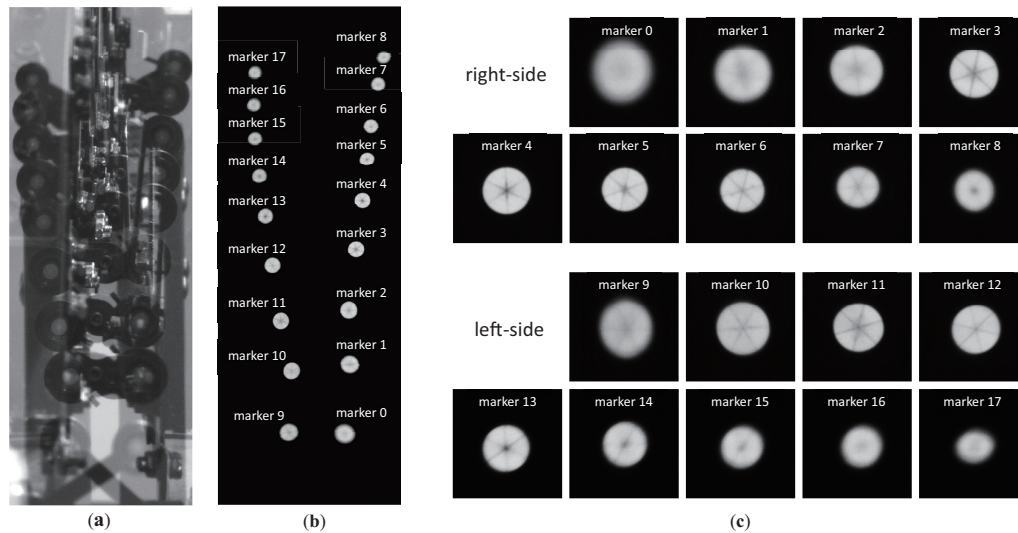
Figure 3.10: Captured image under no vibration.

The scene around the left-side of the bridge model overlapped with that of its right side, but none of the observed corner cube prisms were not occluded in the frame. Reflections from the corner cube prisms were much brighter while the background was very dark, this allowed the position of markers to be extracted without interruption from the background.

Figure 3.11 shows the relationship between the optical path length from the telephoto lens and the observed diameter of the corner cube prisms. The apparent diameters Φ_i of the corner cube prisms were estimated from the diameter of bright pixels in their cropped 150×150 images by binarizing with a threshold of $\theta_i = 10$, as described in Eq. (3.8).

The observed diameters are also shown in Figure 3.11, which were theoretically introduced in Figure 3.4(a). Figure 3.12 shows the relationship between the optical path length from the telephoto lens, and the maximum and average brightness in the cropped image of each corner cube prism. The average brightness was calculated using pixels where the brightness was 10 or greater in the particular region of interest of each marker. In Figure 3.10(c), cropped images of markers 4 and 12 were found to be the best-focused corner cubes at the right and left sides, respectively.
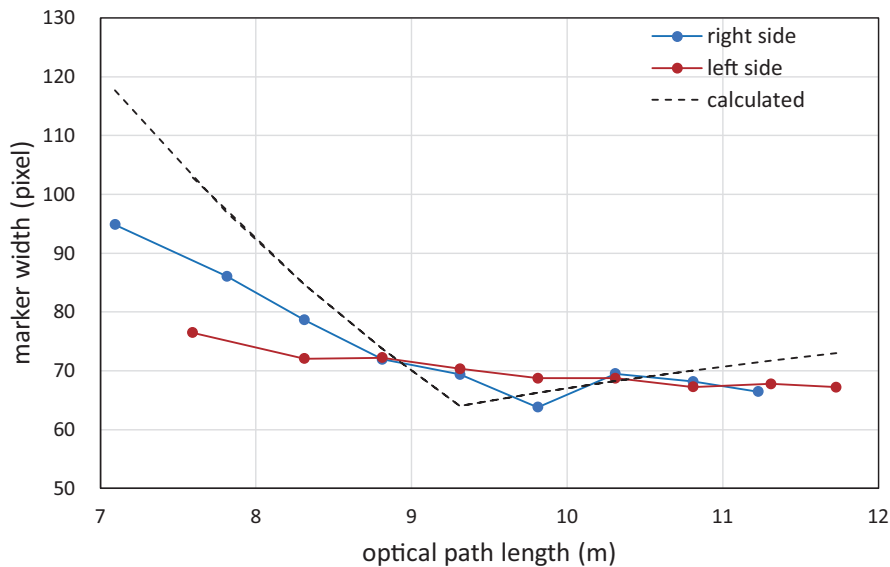
Figure 3.11: Relationship between the apparent diameters of the corner cube prisms and their optical path lengths.

Focal blur in the cropped images of corner cube prisms increased as the optical path length from the telephoto lens deviated from focus distance (D = 9.30 m). The observed diameters of all the corner cube prisms were less than 100 pixels, as illustrated in Figure 3.11. The observed diameters can be independently extracted without overlapping when their center positions are computed. The maximum brightness values of markers 0–8 at the right side were in the 115–128 range, and those of markers 9–17 at the left side were in the 105–120 range. The brightness values of the markers at the left side were slightly smaller than those from the markers at the right side, given the twice reflection from the half mirror and plate mirror. Here, the definition of permissible blur circle mentioned in Figure 3.4(a) did not perfectly correspond to the binarization operation with threshold θ_i = 10 when estimating the markers' diameters from the cropped images, and they were slightly different from those theoretically introduced in Figure 3.4(a).

To confirm the accuracy of the measured displacement of the markers, the center positions of the markers were evaluated at different optical path lengths, corresponding to the locations of markers 0–17 on the bridge model from the telephoto lens. The captured image was 752×2048 images at 240 fps when the corner cube was vertically moved by
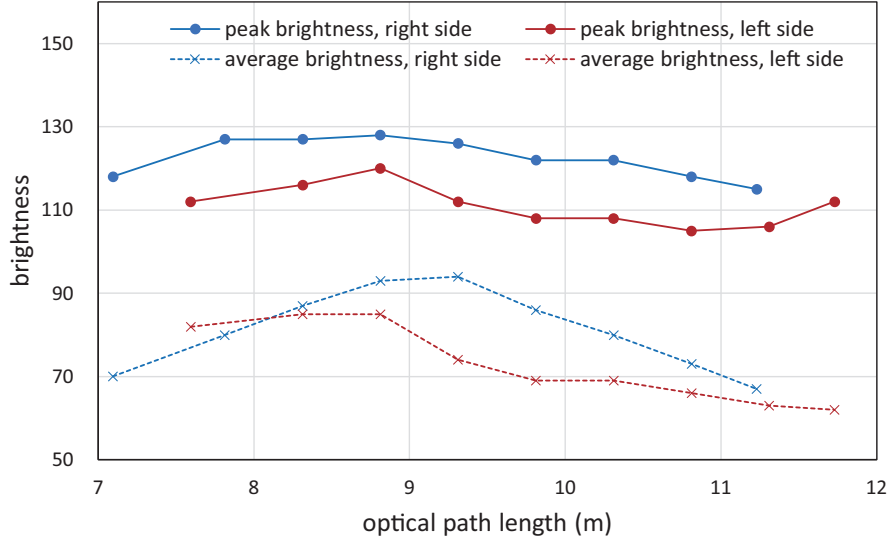
Figure 3.12: Relationship between maximum and average brightness of corner cube prisms and optical path lengths.

10 mm using an optical stage.

Figure 3.13 shows the relationship between the optical path length and displacement in the images (a), and the relationship between the optical path length and scaling factor which indicates the actual physical displacement corresponding to one pixel in the images (b). The increasing ratio of the scaling factors for the left markers was slightly larger than that of those on the right side because the left was not perfectly parallel with the right view due to the additional optical path length between the half mirror and the plate mirror.

Given the varying optical path length between 7.095 and 11.729 m of the markers, a 10 mm-amplitude displacement was observed from 104.8 to 63.5 pixels in the images, and the scaling factor linearly varied from 0.095 to 0.158 mm/pixel. The center position of the markers can be accurately determined at a sub-pixel level when the marker's diameter is larger than 60 pixels in the images.

Assuming that the scaling factor in the lateral direction was similar to that in the vertical direction, the actual displacement of marker i $(= 0, \cdots, 17)$ is computed with the center position (x_i, y_i) estimated from the images as follows:

$$(X_i, Y_i) = (s(D_i) \cdot x_i, s(D_i) \cdot y_i), \qquad (3.12)$$
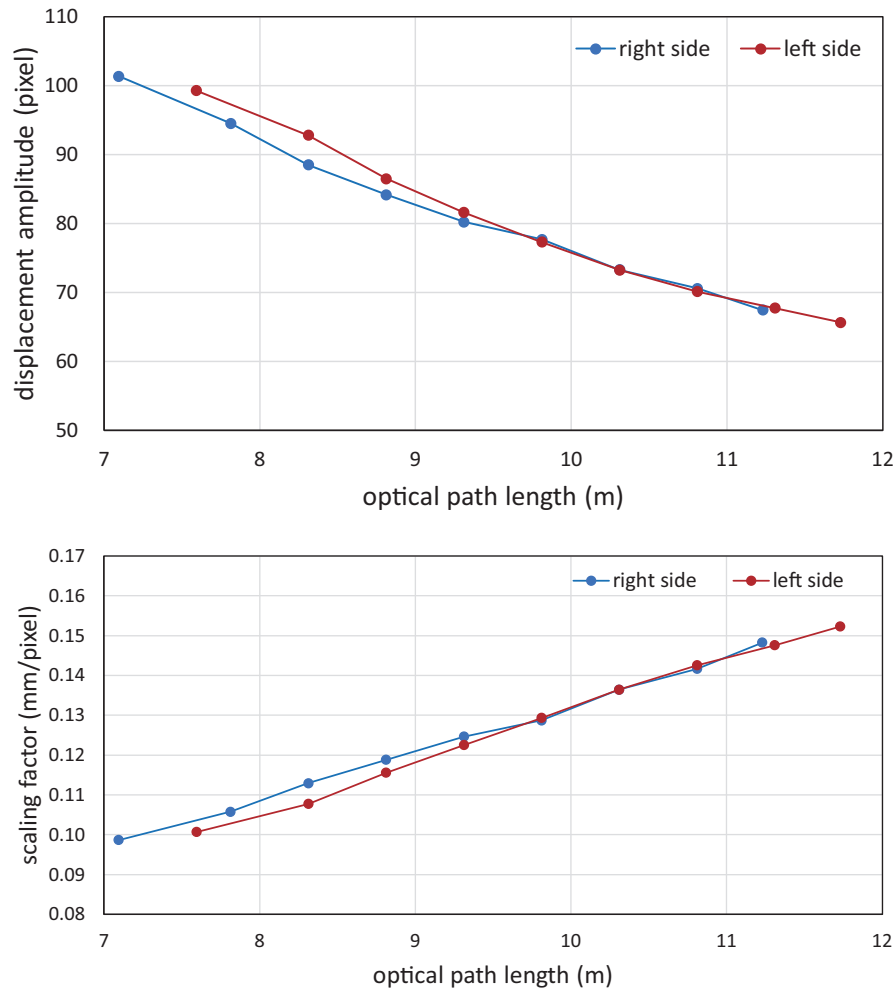
Figure 3.13: Image displacements for a corner cube with a 10 mm optical stage.

where $s(D)$ indicates a look-up table function for the scaling factors, corresponding to Figure 3.13(b). D_i is the optical path length from the zoom lens to marker i, and $s(D_i)$ is the scaling factor when observing marker i in the images.

3.4   Results and discussion

Time-transient vibrations were induced on the bridge model by hand-tapping to measure the structure's natural vibration responses. For each run, 752×2048 pixel images with 10.0 s capture duration at 240 fps. The top of the bridge model was tapped simultaneously using rod striking both sides' chords simultaneously at the centers, corresponding to the locations of markers 4 and 13.

Figure 3.14 shows the captured input images for t = 0.0–91.7 ms captured at 8.3 ms intervals. During the experiment, the maximum pixel-wise displacement for all markers was 1.73 pixels for marker 3 in the lateral direction, and 6.77 pixels for marker 3 in the vertical direction.
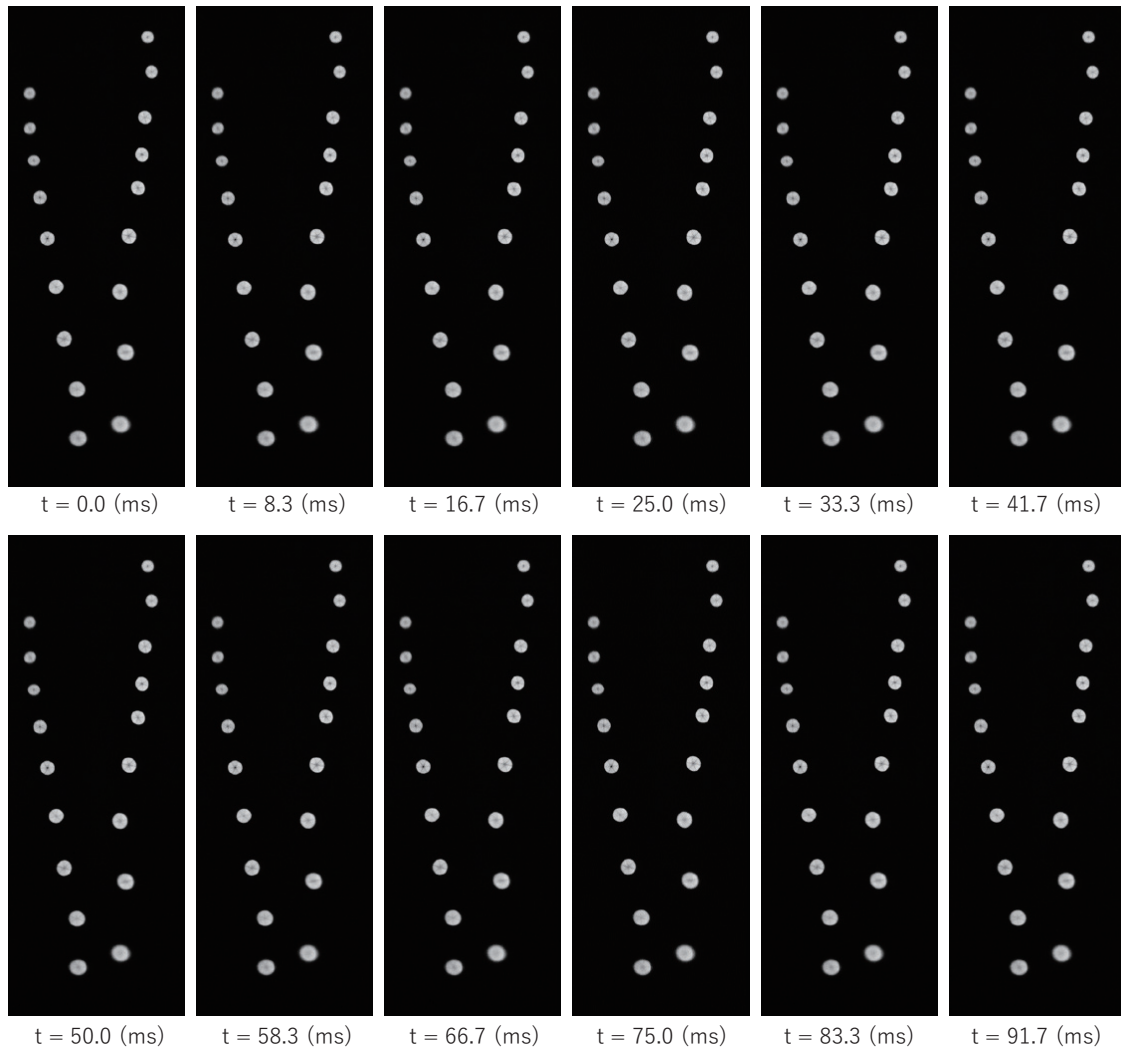
Figure 3.14: Input images when a bright model was tapped by hand.

Figure 3.15 shows time series data of the lateral and vertical positions of 18 markers for t = −0.5–3.0 s. The lateral and vertical positions were set to zero at t = 0.0 s just before the bridge model was struck.

Figure 3.16 depicts the bridge model's deck deflection during the same time duration, showing the relative torsional displacement of deck.

Figure 3.17 shows the frequency response of the vibration signal. Fast Fourier Transform was applied to the vibration signal of each marker from with approximately 5 s of sample window (≈1200 samples). Only two major frequency response peaks were observed in both vibration directions. Vibration in vertical axis was notably higher due to the direction of tapping excitation.

3.4.1 Distributed displacement measurement with different deck configuration

Subsequent experiment was conducted to verify the capability of the displacement measurement system to measure the structural dynamics of the bridge model under different conditions. The dynamics of the bridge bridge was verified by applying modal estimation to the small vibration distributions obtained with our tandem marker-based motion capture method.

In the experiments, different number of $310{\times}400$ m^2 steel plates, each weighing 2945 g, were placed on the deck of the bridge model. The conditions with different number of steel plates, eight (C1), six (C2), four (C3), and two (C4))steel plates respectively, placed on the deck of the bridge model were performed in order to observe the change of weight and resonant frequency of each condition. In the experiments, the experimental settings and protocols including excitation with human hand tapping were the same across different number of plates attached on the deck. Figure 3.18 shows the spatio-temporal deformations of bridge models in the vertical direction.

3.4.2 Modal analysis with SSI-CPAST

Time-varying displacements in the vertical and lateral directions were analyzed for their modal parameters with the SSI-CPAST algorithm [88, 95], which is an output-only stochastic subspace recursive modal identification algorithm to identify the input-invariant dynamic properties of an object under an unknown excitation [96]. The algorithm was applied to the vibration signal of each marker with 90-samples bin and the vibration up to the third modes. Figure 3.19 shows the first mode shapes of the bridge

model under conditions C1–C4.

The first mode resonant frequencies of the bridge model under conditions C1–C4 were found to be 9.82, 9.78, 9.52, and 9.41 Hz in the lateral direction and 9.85, 9.98, 10.20, and 11.70 Hz in the vertical direction, respectively. (see Table 3.4). The first

Table 3.4: First mode resonant frequencies.

Direction	8 plates	6 plates	4 plates	2 plates
Lateral	9.82 Hz	9.78 Hz	9.52 Hz	9.41 Hz
Vertical	9.85 Hz	9.98 Hz	10.20 Hz	11.70 Hz

mode resonant frequencies under condition C1 were closely matched with the first peak frequencies in the FFT analysis, illustrated in Figure 3.17.

The resonant frequency slightly decreased in the lateral direction as the number of plates decreased, while the mode shapes largely varied under conditions C1–C4, corresponding to the locations of the installed steel plates on the deck of the bridge model. The resonant frequency increased as the number of plates decreased in the vertical direction, while the mode shapes did not largely vary under conditions C1–C4. These experimental results show that a vision-based modal analysis can be used to distinguish the structural dynamic properties of the bridge model under different conditions.

3.5   Conclusions and considerations

A tandem marker-based motion capture method has been proposed to to measure small vibrations on a structure with a telephoto lens and high-speed camera by aligning retro-reflective markers on a test structure along the depth direction with a coaxial lighting device. All measurement points are observable in a single camera view without decreasing the measurement accuracy. 752×2048 images were captured at 240 fps with a telephoto lens (focal length of $f = 410$ mm).

Vibration experiments were conducted with a 4 m-long truss bridge model with 18 attached markers. It was confirmed that the single camera head can be used to measure deformation of the bridge structure and estimate the modal parameters, such as the resonant frequencies and mode shapes, at a frequency of tens of Hz.

Several approaches could be used to further extend the applicability of the distributed displacement measurement method:

- fiducial markers for camera-ego-motion compensation algorithms for robustness to ambient vibration in outdoor experiments,

- illumination with specific wavelength to cancel out light interference from changing ambient lighting,

- real-time implementation of the algorithm so that the system be easily installed at a low cost to monitor structural conditions of infrastructure, including bridges, roads, and other large buildings.
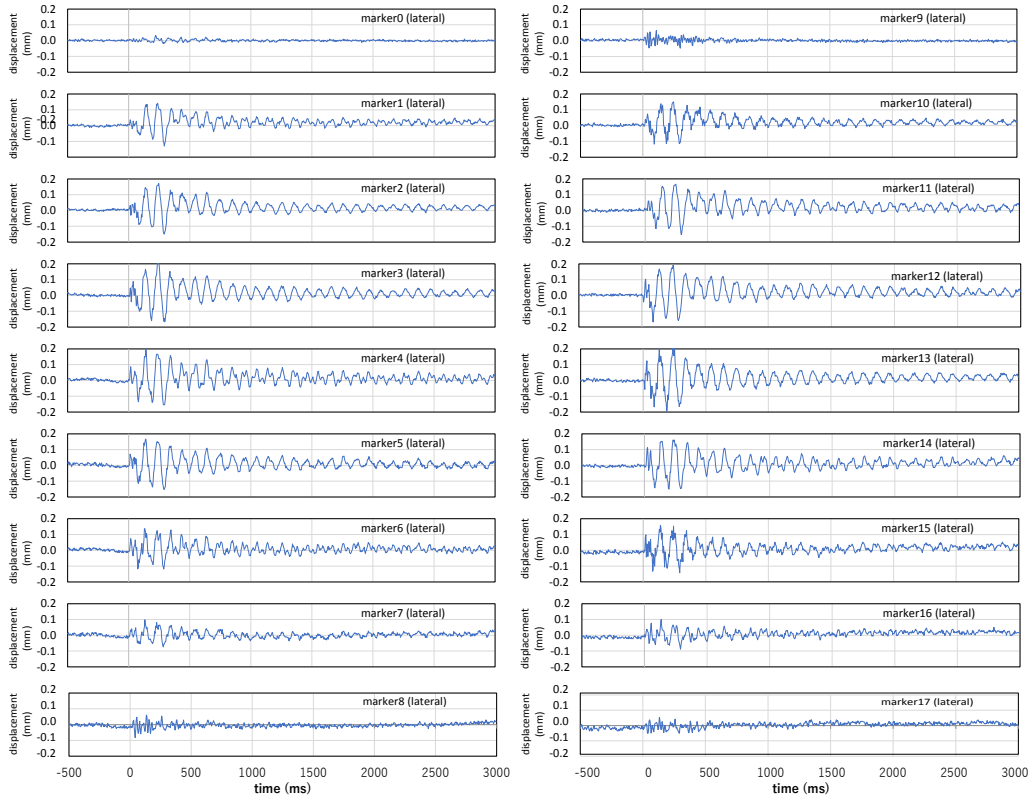
(a)
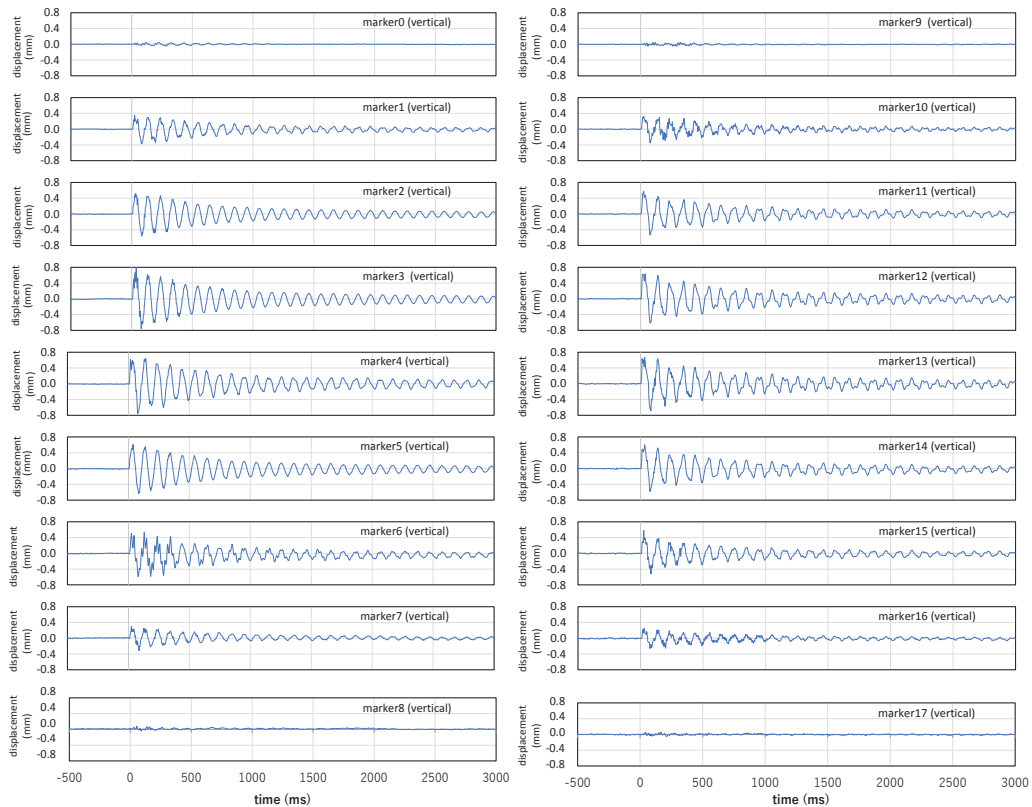
(b)

Figure 3.15: Vibration displacements from 18 markers.
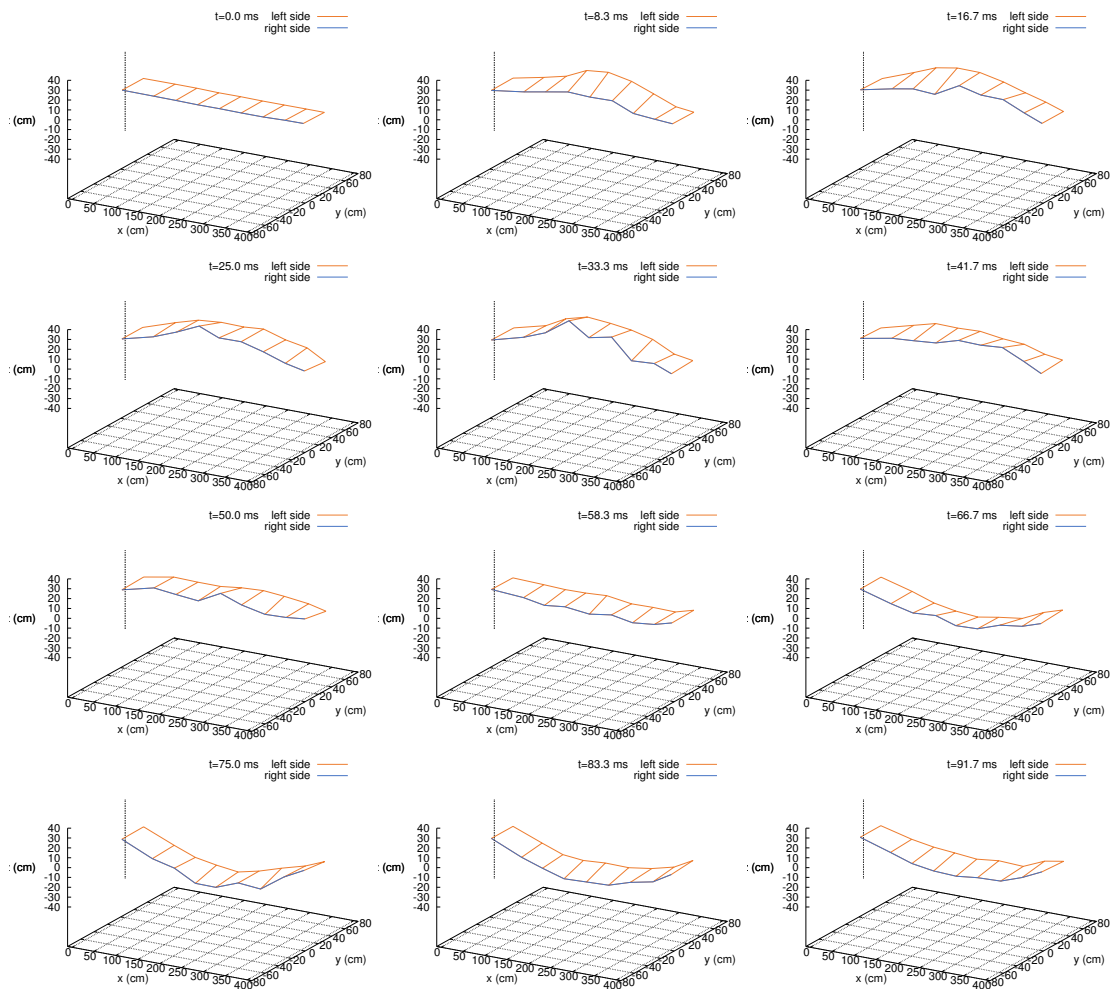
Figure 3.16: 3D deck deflection of the bridge model.

(a)

(b)
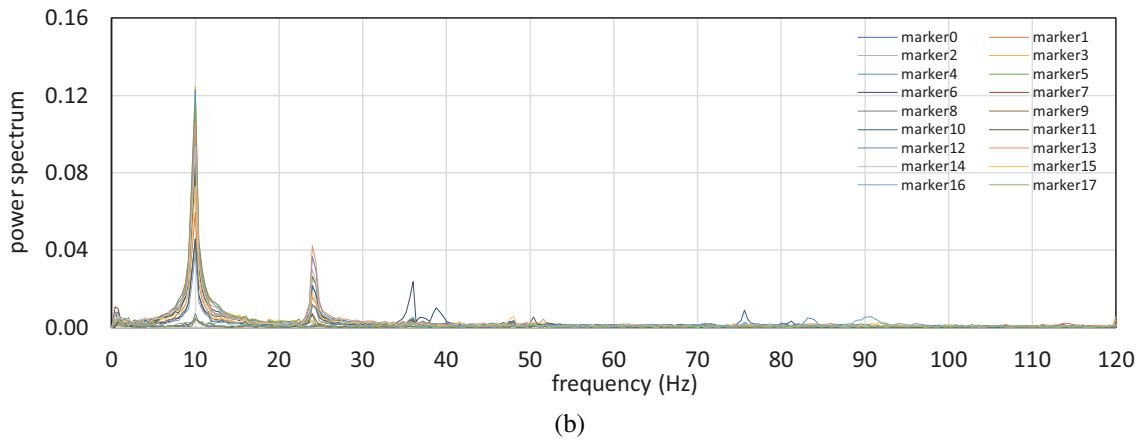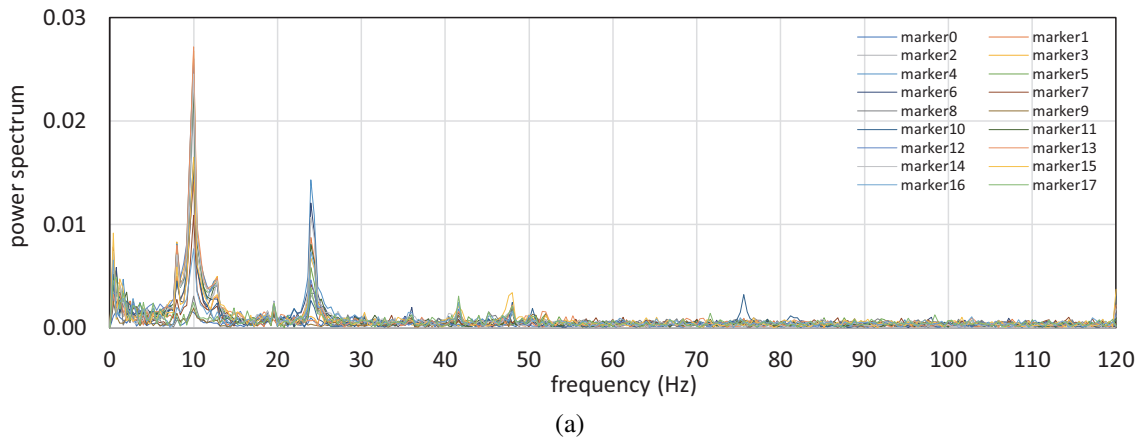
Figure 3.17: Frequency response of the bridge model in lateral and vertical directions.
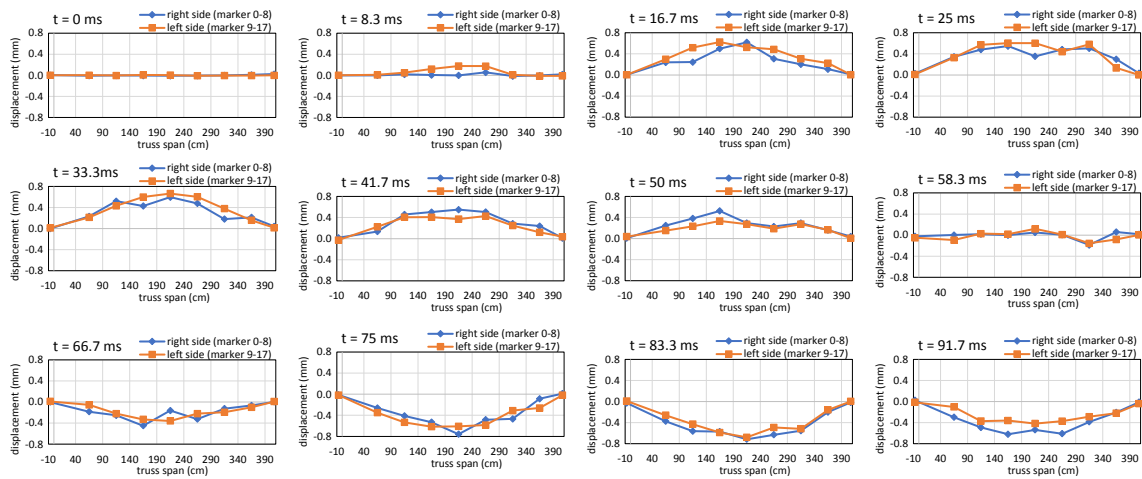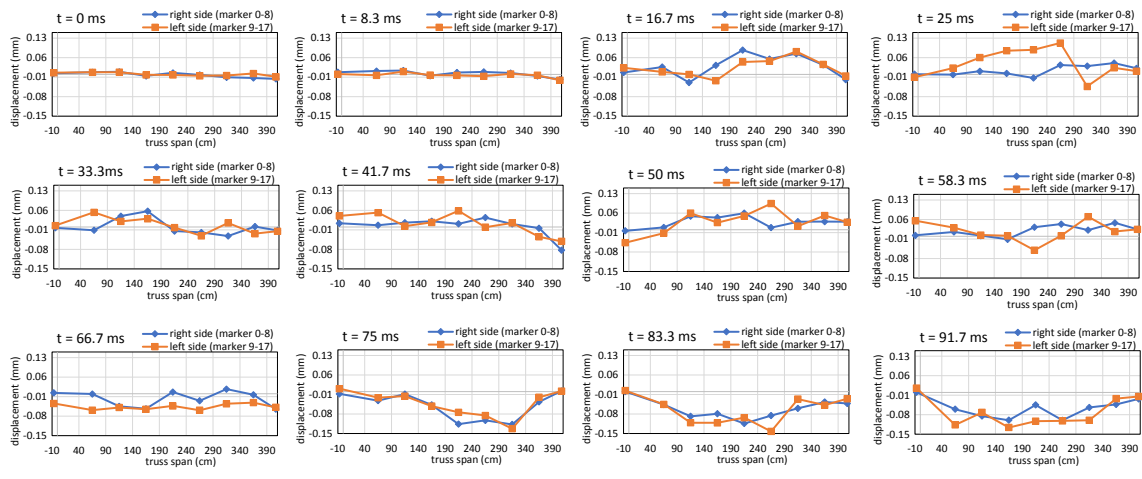
Figure 3.18: Spatio-temporal vertical and lateral deformation of the bridge model.
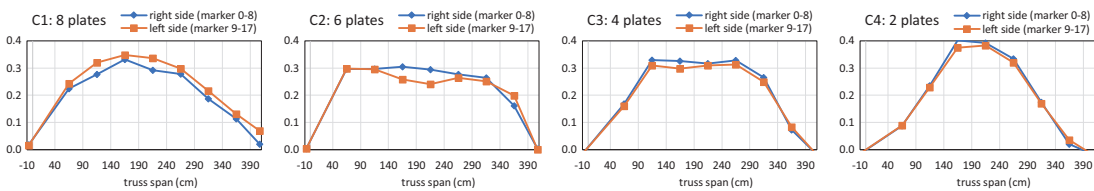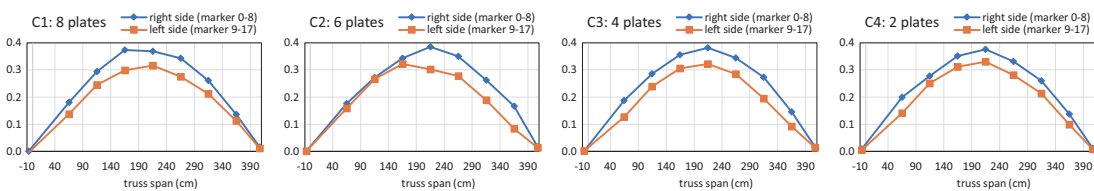
Figure 3.19: First mode shapes of the bridge models in lateral and vertical direction.

Chapter 4

Bridge Structural Displacement Monitoring with Traffic Counting

4.1 Introduction

Vision-based structural displacement methods allow convenient monitoring of civil structures such as bridges, whereas they are often limited due to the small number of measurement points, constrained spatial resolution, and inability to identify the acting forces of the measured displacement. To increase the number of measurement points in vision-based bridge displacement measurement, front-view tandem marker motion capture system is introduced.

A single camera distributed displacement measurement method with sub-pixel digital-image-correlation (DIC) analysis for a tens-of-meters-span road bridge; it is extended from the tandem marker-based motion capture method [97] that allows measurement of structural dynamic displacement from multiple tandem-distributed points at once, without decreasing measurement accuracy by installing a front-view camera positioned with a small angular delineation to the bridge's axis. The strategic position of the displacement measurement camera enables easy-installation bridge monitoring without partial or full traffic closure.

The displacement measurement system is coupled with side-view traffic counting camera to detect passing vehicles from two opposing lanes on the bridge's deck and identify particular vehicles which induces large displacement on the bridge during their pass. The traffic counting system will be able to assist establishing the relationship between the

sizes of passing vehicles and the structural response during such passes.

4.2   Related works

4.2.1   Structural health monitoring with displacement measurement

Bridge experiences elastic vertical, lateral, and rotational displacement from the service load combinations, and such load displacement may cause surface deterioration and local cracking in which could impair serviceability and durability [98]. Continuously-unattended excessive displacement may result in the accumulation of structural damages in the bridge, reflected in the loss of stiffness of weakened parts of the bridge: bearings, joints, integral abutments, and piers. To restrict excessive bridge deformations and vibrations, the displacement limit is determined by linking with human psychological perception on the structural safety due to the occurring structural responses [99], as well as inspecting the appearance of sagging in the bridge girders.

Structural damages are quantified with metrics derived from displacement, such as increase of frequency response in a specific frequency band, a shift of the bridge's modal frequency peaks toward a lower value, a discontinuity in the mode shapes, lower damping coefficient, and other anomalies [100, 101]. Frequency-domain analysis are usually employed on the extracted vibration signals to evaluate the structural health of bridges [102, 103]. The frequency response from bridge natural frequency and traffic load often reside at separate frequency bands [104], thus identifying the frequency response particular to the structure would be possible. Statistics of abnormal modal frequencies can infer structural damages [105]. Although the natural frequencies may exhibit variance between multiple methods, measurement points, and ambient loading condition [102, 104], frequency-domain analysis gives reasonable estimates from the extracted vibration signal. As often the structural damage is localized within a particular member or joint, simultaneous measurement on multiple points on the bridge is also important to pinpoint the damage's approximate location.

4.2.2   Drive-by bridge vibration measurement

Vibration-based SHM refers to in-field non-destructive displacement sensing and analysis of a structure; in the time, frequency, or modal domains. Changes and irregularities in these domains may indicate damage or degradation. Damage to a bridge may lead to some stiffness loss and consequently change its dynamic properties [106, 107]. Loss of stiffness could be reflected from displacement larger than the design value or drop in vibration frequency response given a specified loading condition. In practice, the specific loading condition is performed either using heavily-loaded trucks parked in specified points along the span of the bridge [108], large controlled excitation devices attached to a specific vehicle[109], or more recently with drive-by methods utilizing ambient excitation forces from the usual traffic [110, 111].

Testing the vibration of a bridge from vehicular traffic is intuitive as the bridge's service will still operate as usual and potentially can be done continuously in real-time. But in practice, the interaction between vehicle and the bridge will vary due to factors related to the bridge construction (length, dead mass, deck surface roughness, thermal stress on the members) [105], the passing vehicles (axle spread, weight, speed, suspension) [112], or superposition of multiple vibration sources [113].

The impact of vehicle load on bridge vibration varies by the weight on each axle, the distances between axles, and the number of axles. Vehicles need to be configured in such a way that the excitation force will result in dynamic displacement that is discernible from ambient vibration from the bridge's dead weight and environment [114], thus heavy vehicles are often used for various tests on a bridge instead of common car traffic. Vehicle speed and bridge deck roughness also affect the vibration profile of the bridge. At higher speeds, vehicle vibration dominates the observed vibration signal, hiding the bridge vibration itself, and the vehicle speed needs to be relatively low to obtain good separation between bridge and vehicle vibration frequency, as previously reported: 18 km/h [114], 36 km/h [115], and 40 km/h [110].

4.2.3   DIC analysis

Digital Image Correlation (DIC) is a method to infer sub-pixel deformation between two images using correlation of defined facet [116] from the object's normal surface, non-periodic speckled pattern, or target marker apparatus. DIC evaluates various criteria from the facet in a single 2D-plane [117], such as cross-correlation, sum of absolute, difference, and squared sum of difference. The adjacent frames can also be evaluated in either forward or backward temporal direction [118]. DIC can be expanded for multi-plane measurement using stereo camera heads, beam-splitter prism or mirrors, or wavelength separation of the exposures [119]. Measurement in 3D-plane can be achieved with digital projection of the facet or oblique arrangement between the camera and object with known distance [120]. The latter is more common for displacement measurement of structures.

Various DIC applications have been demonstrated on model bridge to measure displacement, strain, and modal responses [102, 121–123]. DIC shows comparable results to conventional methods with accelerometers, laser vibrometer, or finite element simulation [44, 102]; despite its limitations regarding changes in facet appearance [122], image distortion and out-of-plane displacement or rotation [124], limited sampling rate [125], and stray frequency responses from sensor aliasing or ambient vibration [44].

DIC has been implemented on actual bridges in several studies with addressing the issues of real-time performance, image degradation from optical turbulence, and sub-pixel accuracy [46, 126, 127]. Such implementation has yet to consider the moving traffic and address the inaccuracy due to imprecise synchronization of multiple cameras [128]. There is a trade-off between the field of view and spatial resolution due to finite sensor size and focal length. Usage of a pan-tilt mechanism allows wider field of view without resorting to lower pixel-wise spatial resolution [129], but the setup may introduce unwanted vibration and image distortion from the varying object distances. A higher spatial resolution could be achieved by applying a complex filter to down-sampled subset of the image [46, 121].

4.2.4   Video-based traffic counting

Traffic counting system detects individual passing vehicle and infer its properties: time of passage, travel direction, length, and estimated velocity. These information can be used for various purposes: congestion detection, automated tolling, road design, speed limit enforcement, etc. Automated traffic counting system has been implemented with various detectors, e.g. induction loop, speed-trap laser, and surveillance camera. Video-based traffic counting system is characteristically more robust with long MTBF (mean time between failures) compared to other detectors [130].

Video-based traffic detection methods of passing vehicles have been implemented with various techniques: MoG (mixed of Gaussian) [131] and frame-history background subtraction [132] can filter out non-static multi-modal background (e.g. shaking leaves, swaying branches, shadows), but both can still result in false detection of slow-moving or stopping vehicles, overlapping vehicles (either from a single or adjacent lanes). Color-histogram clustering addresses the issue with overlapping vehicles, but in turn exhibits inaccuracy due to sudden change of vehicle velocity, illumination changes, and color composition variation [133]. Image segmentation method with rolling average threshold proved to have good accuracy in various weather and lighting conditions [134], with detection lines to facilitate detection in multi-lane setting with heterogeneous traffic [135]. This proves that simple and adaptable image processing routine will suffice if detection thresholds are adjusted properly.

Classification of the detected vehicles has been conducted to infer their properties. SVM (support vector machine) classification is often inaccurate [131], and increased accuracy comes with the added cost of computational complexity [136]. The CNN (convolutional neural network) method promises better accuracy [131] but requires prior supervised learning for various different vehicle appearances, camera orientations, and lighting and weather conditions [137–139], and generally performs slower compared to image-processing-based methods. Thus, context-specific criteria should be applied to extract meaningful information from the passing vehicles to obtain better execution speed with acceptable accuracy.

4.3   Tandem marker motion capture with side-view traffic monitoring

Integration of structural health monitoring on a bridge and traffic identification allows measurement of structural dynamic response from traffic load to assess the structural integrity of the bridge. Several studies have been carried out by integrating an array of sensors (strain gauge, accelerometer, weigh-in-motion plate) and traffic monitoring video cameras [140]. Video-based methods have also been applied in place of the sensors to facilitate non-contact measurement of the bridge vibration under live load, measuring the deflection of a portion of the structural members, e.g., girders [141] and cable stays [142].

Although such systems are generally comparable to finite simulation [143] and able to identify simulated damages [144], they are still constrained due to the finite number of measurement points, the requirement of synchronization between cameras [142], and the lack of generated data from the traffic counting camera, especially in real-time setting [145].

The sub-optimal common placement of both displacement measurement (perpendicular to the bridge's axis) and traffic counting cameras (high vantage point) resulted in a set of issues: limited measurement field and the requirement of separate calibration/alignment for each displacement measurement camera [141], the difficulty to estimate the passing vehicle's details (size, type, speed), and susceptibility to errors related to frontal occlusion for the traffic counting camera [131, 146, 147].

4.3.1   System concept

Tandem arrangement of the optical markers along the span of a bridge with the frontal placement of displacement measurement camera has been found to facilitate simultaneous capturing of multiple displacement measurement points from a single camera viewpoint in its depth of field, requiring no synchronization module for multiple-points measurement [97]. This could enable a simpler method of whole-span bridge displacement observation. The placement of traffic counting camera perpendicular to the bridge axis could also allow a more reliable estimate of the passing vehicles' dimension.

This study aims to to identify the structural dynamic response of an actual bridge from various live traversing vehicular traffic, using combination of single-camera motion capture DIC technique and traffic counting system. The dynamic displacement signals from DIC analysis will be cross-referenced against traffic information using a synchronized timestamp. Figure 4.1 illustrates the general framework of the system. Frontal measurement displacement simultaneously captures multiple measurement points with additional static reference marker to cancel camera vibration. Side traffic counting camera captures the passing vehicles more accurately. Displacement and frequency of the traffic-induced vibration will be evaluated.
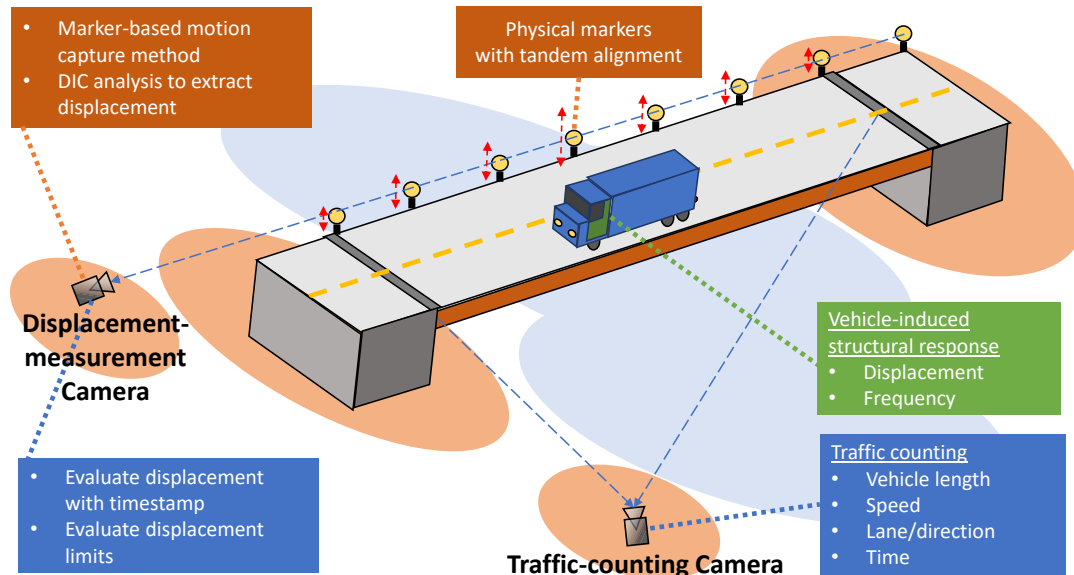
Figure 4.1: Framework of SHM method for traffic-induced dynamic displacement measurement using marker-based motion capture and traffic counting camera.

4.3.2 Field experiment with DIC

Field experiment was conducted on Hinotsume Bridge (34°21'27.2"N 132°43'17.4"E). The structure incorporates two steel plate girder spans with a concrete deck spanning in east-west direction which allows both vehicles and pedestrians to cross. Each span is approximately 25 m long with a support pier in the center connecting the two spans. The two-lane roadway on top of the structure is 8.4 m wide with adjacent sidewalks 2 m wide in both sides. Guardrails are featured on the edges of the bridge, also between the

sidewalks and the roadway. The speed limit in the vicinity is 50 km/h.

The displacement measurement camera was installed at the shoulder of the road to the west of Hinotsume Bridge facing eastward, positioned 64.2 m away from the furthest marker. With its depth of field mostly parallel to the bridge's axis, this allows simultaneous capturing of tandem-layout markers installed on the bridge without occlusion. The traffic counting camera was installed to the north of the bridge by the riverbank to capture the whole span of the bridge from perpendicular direction, as shown in Figure 4.2. The perpendicular placement to the traffic direction may allow more robust detection and length estimation of the individual passing vehicle.

(a)

(b)

(c)
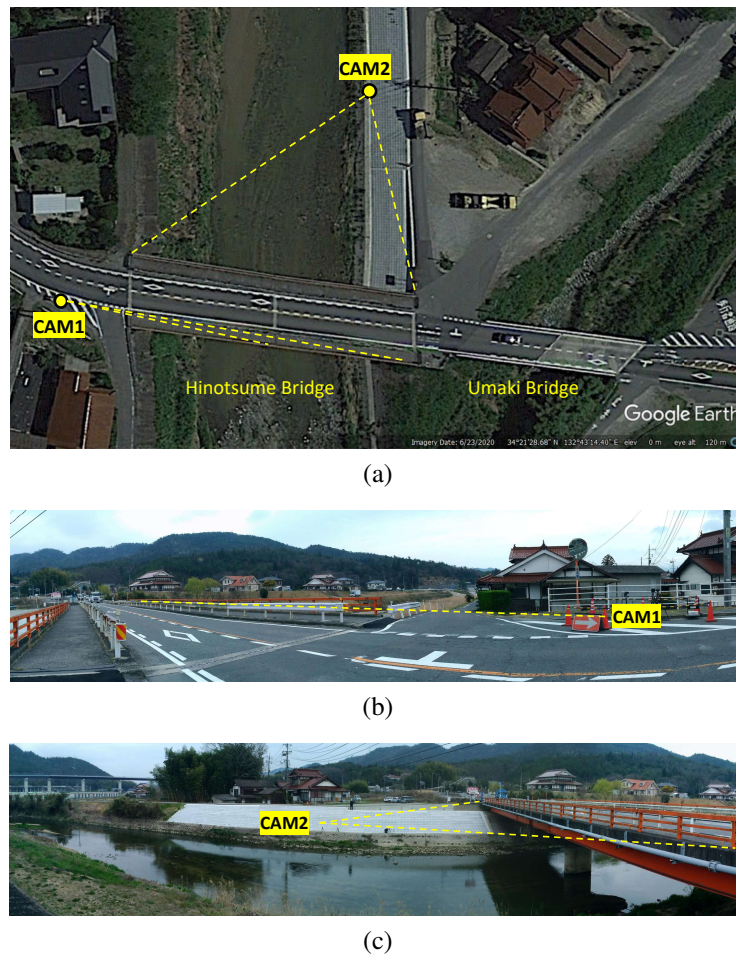
Figure 4.2: Field of view of displacement measurement camera (CAM1) and traffic counting camera (CAM2).

Cameras for the experiment are Panasonic HC-WZX2M at 1920×1080 px reso-

lution. Frame rate was 60 fps with 1 ms exposure, short enough to eliminate motion blur while still bright enough to detect the facets for DIC analysis reliably. Focal length of the displacement measurement camera was set to 98.9 mm with F/16 aperture to obtain as much depth of field as and the sharpest focus at maximum The daylight provided enough light for proper exposure in the displacement measurement camera even at its narrowest aperture. The duration during the experiment was 35.4 minutes during afternoon hours (15:49 to 16:25 JST). The daylight during the experiment provided enough light for proper exposure even at its narrowest aperture and no underexposure was observed in the captured frame of the displacement measurement camera, as shown in Figure 4.3b.

The markers were installed on the edge guardrail of the eastern span approximately 3.9 m apart from each other using a magnet holder stand (MiSUMi-VONA MNMGB-SHLD, Japan), as shown in Figure 4.3a. Markers' displacement was evaluated relative to the fiducial reference marker (M0) which was assumed to be static, installed on the abutment to the east of the bridge isolated from the deck, providing a mechanism to cancel camera head vibration. The markers were installed in a pattern as such that all the markers could be captured without occlusion from one another at different distances from the camera, as shown in Figure 4.3b.

Displacement measurement was performed using commercial DIC solution (GOM Correlate 2019 Hotfix6 rev. 125216, GOM GmbH, Braunschweig, Germany) which features point-based and full-field displacements measurement. Only displacement in vertical direction was evaluated in the analysis to emphasize the effect of vehicle loading on the bridge. Figure 4.4 explains the general workflow for DIC displacement measurement process. The deformation images have been cropped beforehand to reduce computational time of DIC process. The images would be discarded from DIC analysis if occlusion occurs between the camera and markers due to traffic coming from the sides. Displacement of each facet is estimated based on the position of region of the image with the highest correlation criteria across multiple frames.

As the facets' vertical displacement was evaluated from only a single axial plane, the calculated displacement of all markers was calibrated from the known object size of the printed pattern marker (60 mm) of marker M1. Displacement of each marker would

(a)
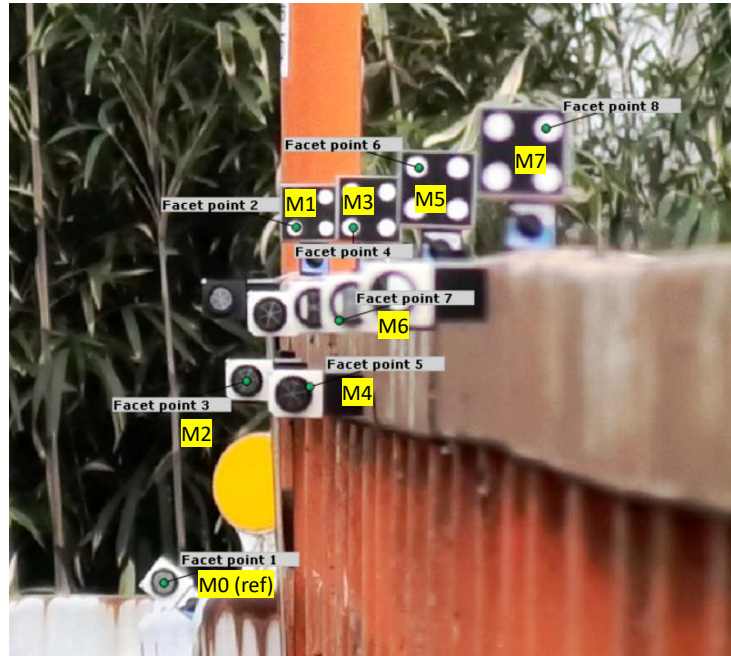
(b)

Figure 4.3: Markers' placement and the cropped field of view from the displacement measurement camera.

need to be rescaled separately based on its respective distance to the camera.

Scaling factor defines the ratio between actual physical displacement and perceived pixel-wise movement in the captured image. The approximate scaling factor for each marker is evaluated from the ratio of its respective distance to marker M1 distance from the camera, as specified in Figure 4.5, assuming no focal distortion from the displacement measurement camera throughout its field of view and no out-of-plane movement of the markers. Thus, the displacement for marker number n at time t is given as

$$S_{n,t} = \frac{SF_n}{SF_1}(P_{n,t} - P_{0,t})$$ (4.1)

where P is the captured pixelwise movement, SF is scaling factor for each marker, and S
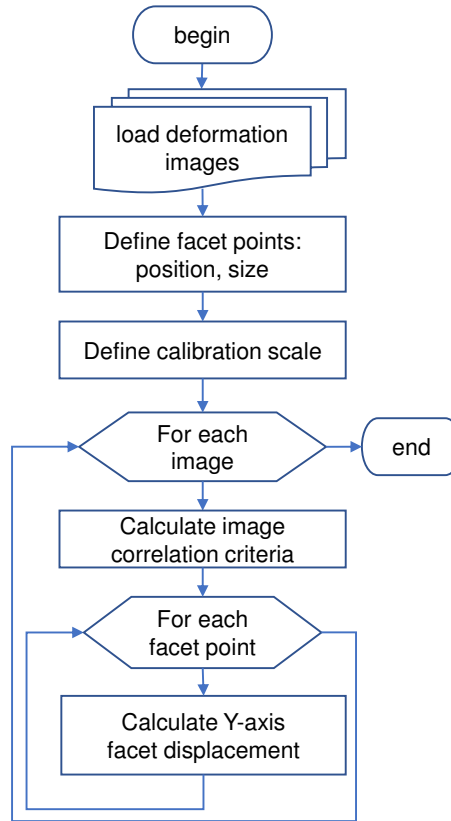
Figure 4.4: General workflow of DIC displacement measurement from multiple facets in a single plane.

is the measured displacement.

Given that the displacement limit of a bridge is often defined using static displacement and the loading scenario during the experiment is entirely dynamic, single-point time-series static displacement from the structure is approximated using differential displacement. Differential displacement evaluates single-point displacement between the center of the span and abutment in the time domain, given as

$$D_t = S_{4,t} - S_{7,t},$$ (4.2)

where S is the measured displacement of each marker at time t.

Differential displacement was calculated to compensate with the changing measurement baseline due to temperature, non-steady traffic flow, and facet detection drift from DIC process. Intermittent traffic jam and temperature changes had been shown to
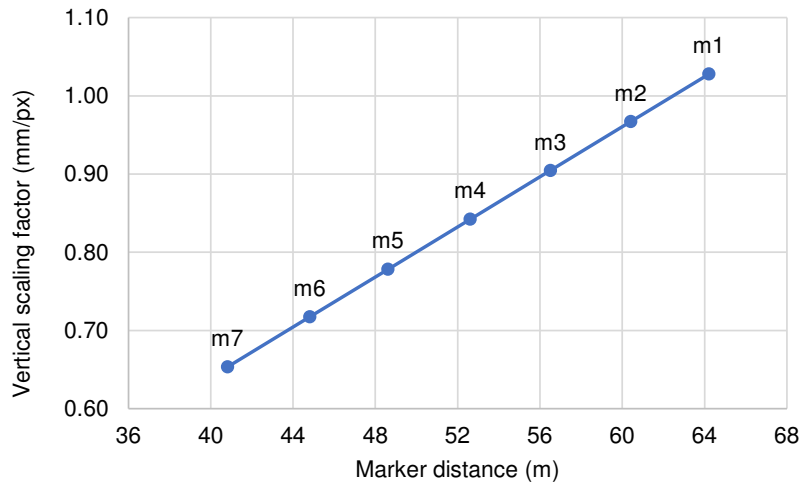
Figure 4.5: Scaling factor for each marker at different distances.

exhibit drift in the structural responses [148]. Butterworth band-pass filter (10th order, 1 Hz to 1.2 Hz band) was then applied on the differential displacement signal to suppress the vibration irregularities from the reverb vibration, vehicle suspension, road roughness, or superposition of vibration from other vehicles. Such signal smoothing has proved to better extract static component of bridge response [149].

4.3.3   Traffic counting from side-view camera

There was persistent occlusion from the guard rails as shown in Figure 4.7a, which made capturing the vehicles' full shape impractical. This may pose a challenge to neural network-based object detection. Thus, vehicle detection was performed using basic image segmentation to reduce complexity and increase the traffic counting system's overall performance in the experiment. The traffic counting system was implemented on a laptop computer (HP Omen 15-dc1xxx, Intel i7-8750H, Nvidia RTX2070, 32 GB RAM, python 3.8.6) and performed at 80 fps, citing the possible real-time application for the video stream captured at 60 fps from the camera. A preliminary experiment showed that a CNN-based traffic detection methods (YOLOv3 and YOLOv4, predefined standard weights) performed at 24 fps on the same platform. Given that the video frame was captured at 60 fps, we opt for the image-segmentation method to not lose any data

Figure 4.6 explains the workflow of the image processing routines for the traffic

counting system. A random ID is assigned to the blob wider than 60 pixels, which is maintained throughout the pass' duration between two defines line segment. Smaller blobs are regarded as non-vehicular traffic (pedestrian, motorcycle, etc.) or image noise from the environment. Figure 4.7 shows the images being handled from the traffic counting camera: captured image from the traffic counting camera, intermediate images in the background segmentation process, and the resulting image with tagged vehicles.
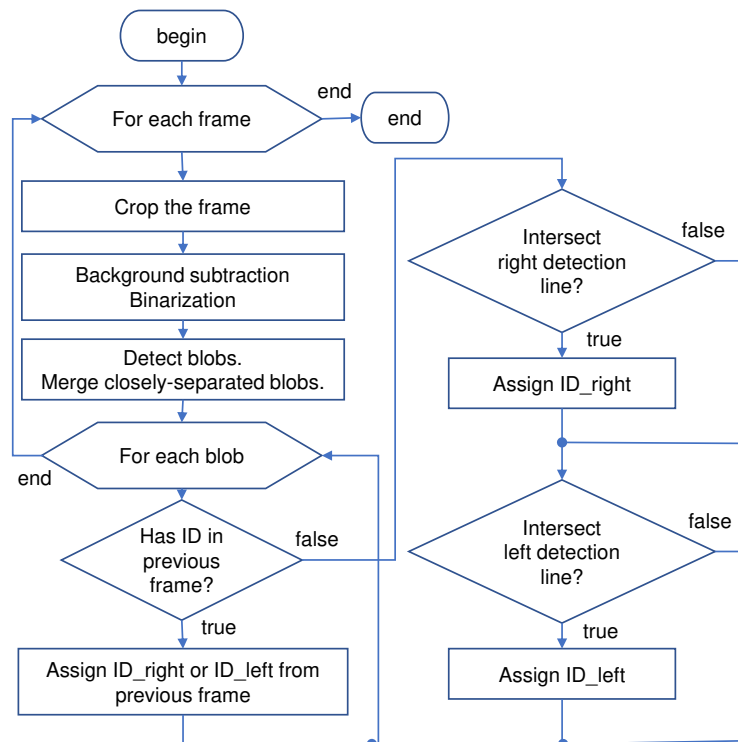
Figure 4.6: Flowchart for traffic detection algorithm.

Closely spaced blobs within 10 px apart are merged to account for the occlusion from the guardrail. A unique ID is assigned to a sizable blob (60 px wide minimum) based on its initial position when crossing either of the detection line. A single-vehicle blob can be assigned with two IDs (right-going ¡100, left-going ¿100) to handle momentary occlusion between left-going and right-going vehicles. The final ID is selected based on whether the ID value matches the movement direction.

Figure 4.7a cropped within the region of interest covering the bridge's deck. Background image was defined for background subtraction process is captured when no vehicle is present on top of the bridge (Figure 4.7b), updated with 10 minutes interval. The result-

(a)

(b)

(c)

(d)

(e)
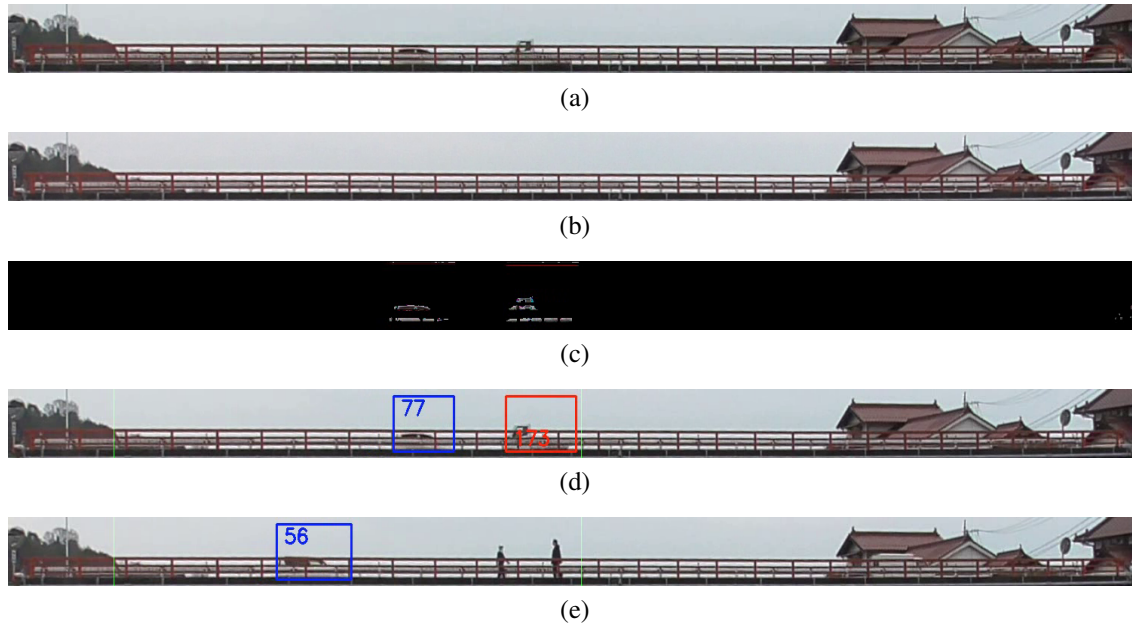
Figure 4.7: Captured frames from the video stream of traffic counting camera.

ing detected vehicle blob after background subtraction (Figure 4.7c) shows the masked detection region before the result frame with a unique ID assigned to the detected vehicles' blob (Figure 4.7d). The blob selection was able to filter out non-vehicular object such as walking pedestrian from vehicle detection based on minimum blob width (Figure 4.7e).

Lane overlap occurs when two vehicle coming from different direction and the right-going vehicle is hidden behind the left-going vehicle. At the first frame of such lane overlap, the ID from the opposing vehicle is doubly-assigned to each other. This ensures that a specific ID is retained for a vehicle throughout its pass duration despite momentary lane overlap with other vehicle(s). By the end of the pass, the ID is checked to match to its travel direction assuming that no vehicle is going reverse. Traffic count data during the duration of lane overlap is discarded from evaluation to ensure more representative data of respective vehicles.
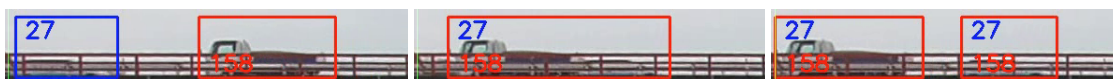
Figure 4.8: Image sequence before, during, and after the lane overlap.

4.3.4 Algorithm and analysis

Frequency-domain analysis is conducted to measure load-specific structural response from the bridge. Frequency spectrogram was evaluated using Fast Fourier Transform (FFT) from the measured displacement of M4 with 128 samples bin at 33 ms step. Only the lower half frequencies of the FFT output is presented for the analysis.

Displacement from all markers shall be evaluated not to exceed the displacement limit set in the design to ensure structural safety. Displacement limit defined by AASHTO (American Association of State Highway and Transportation Officials) will used for the evaluation, which considers the bridge material, construction type, designated load, and perceived psychological safety of the structure [150], summarized in Table 4.1. Compound load type (vehicular and pedestrian) has stricter displacement limit criteria as pedestrian is more sensitive to movement due to the absence of direct suspension system.

Displacement over the specified value indicates structural deficiency, although such deficiency may not right away lead to a structure failure and the bridge may still subsequently be able to serve typical loads within the limit. Nonetheless, repair or retrofit will be needed to ensure structural safety in the long run to avoid accumulation of damage.

Table 4.1: Criteria for displacement limit on girder bridge.

Bridge Construction	Load Type	Displacement Limit
steel, alumunium, or concrete	vehicular only	span/800
steel, alumunium, or concrete	compound	span/1000
steel, alumunium, or concrete (cantilever)	vehicular only	span/300
steel, alumunium, or concrete (cantilever)	compound	span/325
timber	compound	span/425

Frequency-domain analysis is conducted to measure load-specific structural response from the bridge. Frequency spectrogram was evaluated using Fast Fourier Transform (FFT) from the measured displacement of M4 with 128 samples bin at 33 ms step. Only the lower half frequencies of the FFT output is presented for the analysis.

4.4   Results and discussion

The experiment looks to measure dynamic structural responses under normal traffic flow. Several metrics (raw displacement, differential displacement, and frequency response) are to be evaluated and associated with each of the passing vehicle based on its timestamp. The displacement values should not exceed the defined limit at any occasion.

4.4.1   Long duration displacement measurement

Figure 4.9 shows the markers' displacement, derived differential displacement, and frequency spectrogram. The largest displacement during the experiment was 6.944 mm in M4 and still within the limit defined in Table 4.1 (25 mm, 1000th of the 25 m span). At any occasion during the experiment, neither measured raw displacement (Figure 4.9a) nor differential displacement (Figure 4.9b) exceeded the load rating of Hinotsume Bridge. This indicates that no overweight vehicle passed on the bridge and the displacement in vertical direction had been all within the range of elastic deformation. The constant low-amplitude vibration in the displacement signals could be attributed to sensors noises and spatial aliasing in the camera system and DIC process [44].

Passes of large vehicles resulted in large displacement in the markers clearly observable from the baseline. Short-duration peaks were observed in the displacement signals and the frequency response during large vehicle passes. The displacement is dominated by first mode curvature shown as single low frequency peak in the spectrogram (Figure 4.9c). Notable low frequency responses (peaks at 0.3 Hz) occurred at the same point as its differential displacement signal.

This could be useful to identify the bridge's structural response to loading forces which was excited exclusively from large vehicular traffic. But, passes of large vehicle might not always result in large structural displacement as the vehicle could possibly be lightly loaded, the axle load was spread further apart, or the possibility of vibration superposition from multiple vehicles/axles which canceled each other.

The temporary drift observed in the baseline of differential displacement signal, i.e., *t= 1020-1200 s* and *t= 1650-1800 s*, could be attributed due to image disturbance

from loose attachment, heat haze, or shadow cast on the markers [126]. Such occurrences simply affect the accuracy of DIC facet position detection rather than imply constant load on the bridge.

4.4.2 Traffic count

Traffic count during the duration of the experiment is shown in Figure 4.11. Among the detected 336 vehicles passes, 188 were going eastbound (left-going) and 148 westbound (right-going) with calm traffic flow. The slight difference could be attributed that the bridge is located in a feeder road to Umaki Interchange (Japanese Expressway E75) situated nearby to the east, of which many vehicles is heading towards to reach other places. The length of vehicle was evaluated from the passing vehicles' pixel-wise width in the frame, using different scaling factors for each lane as the left-going is closer to the camera: 36.55 mm/px (left-going) and 38.38 mm/px (right-going). The speed of detected vehicles was evaluated from the distance traveled and its duration from a particular ID.

In addition, vehicle speed and length were evaluated in relation to identify the vehicular loads, shown in Figure 4.10, further classified in Figure 4.12. Traffic was dominated by small and compact cars with occasional large trucks, mostly calm with the average of 4.13 vehicle/min eastbound and 3.25 vehicle/min westbound. Figure 4.12a shows that Japanese light *kei* car (¡ 3.4 m) was most common. Passing speed histogram (Figure 4.12b) shows that drivers adhered to the speed limit enforced (50 km/h). Besides, as the experiment was conducted while the inspectors standing on the shoulder of the road, drivers might voluntarily slow down slightly to ensure the safety of their surroundings.

Displacement of markers obtained from DIC analysis, accompanied by its timestamp, was cross-referenced with the timestamp from the traffic counting process to obtain correspondence between the passing vehicles and induced displacement on the bridge. Figure 4.13 shows the relationship between the markers' displacement and passing vehicles' length and speed. Most passes resulted in displacement less than 1 mm, while large displacement was only observed during passes of large vehicle longer than 8 mm. The vehicle needed to travel at substantial speed to induce substantial structural displacement

on the bridge. Also, several small vehicles were cross-recorded having large displacement due to crossing the bridge at the same time as a large vehicle. As there was no over-speeding large vehicle, effect of speed in amplification of force dynamics could not be observed.

4.4.3   Structural response from passing traffic with DIC

Bridges often will only exhibit notable structural displacement response from sizable vehicular load. AASHTO and FHWA (Federal Highway Administration, US) defined truck configurations and dimensions employed for load test on bridge for traffic load [150, 151], summarized in Table 4.2. These large vehicle configuration were incorporated for detection in the traffic counting system to determine the bridge's structural displacement from the traffic load.

Vehicle of interest (large vehicle) was classified based on the estimated vehicle length, given that the weight of the trucks could not directly be measured from the video feed. Although there is no exact specification on vehicle length for bridge live loading in Table 4.2, AASHTO exemplifies that the standard load trucks' total length are 3.66 m (12') longer than their outside axle spread [150]. Considering the shortest specified axle spread in the list is 4.27 m, only detected vehicles longer than 7.9 m (26') would be selected for displacement analysis. Three-axle truck may have variable outside axle spread up to 13.4 m (44') with the same tractor configuration as two-axle truck. Longer combination vehicles are not allowed in Japan road networks.

Table 4.2: Standard trucks for bridge impact testing.

Configuration	Gross Weight (ton)	Outside Axle Spread (m)
Two-axle truck	13.64	7.85
Three-axle truck*	24.55	10.67
Four-axle trailer	29.09	11.13
Five-axle trailer	36.36	20.21
Six-axle trailer	40.91	20.37
Five-axle double trailer	36.36	23.26
Seven-axle double trailer**	54.55	32.41
Eight-axle double trailer**	56.36	27.84
Nine-axle double trailer**	67.27	40.03
Seven-axle triple trailer**	60.00	33.29

Table 4.3 shows four occasions of large vehicles' passes among such passes, which resulted in differential displacement larger than 2.5 mm throughout the duration of the experiment. The corresponding raw displacement signal, differential displacement signal, and frequency response of those passes in one minute segment are shown in Figure 4.14. The corresponding identified passing vehicles in the passes are mentioned in Table 4.3.

The largest peak displacement was consistently observed in M4 (center of the span) with the peak displacement tended to be smaller towards both ends of the span. This agrees with the prior finding that the first mode curvature constantly comprises the largest component of traffic-induced displacement at all various speeds and weights of the passing vehicles [152].

Consecutive passes of vehicles resulted in sustained vibration which was initially excited from the pass of a large vehicle. The vibration larger than baseline lingers until the last trailing pass as shown in Figure 4.14c, with distinct frequency response peaks observed in Figure 4.14d despite its displacement signal has not return to baseline. Passes of left-going large vehicles resulted only in small displacement compared to right-going ones, shown in Figure 4.14b. This could be attributed to the fact that the displacement markers were placed closer to the right-going lane and torsional vibration happens on the span. Low frequency vibration spectrum was observed during the passes of large right-going vehicle while the passes of small vehicles did not result in notable vibration as in the earlier part of Figure 4.14a and Figure 4.14b.
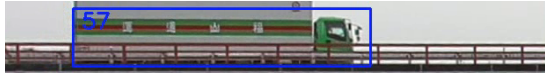
The marker displacement signal from the four passes is presented in more detail in Figure 4.15. Notable damped first mode vibration component ($\approx$0.3 Hz) was observed on the markers for the duration of approximately 3 s upon the excitation from the pass of a large vehicle, followed by high-frequency small-amplitude transient damped vibration. Consecutive pass(es) of either large (Figure 4.15d) or small (Figure 4.15c) vehicle following an initial excitation from a large vehicle's pass resulted in sustained 3 Hz vibration.

All markers started to vibrate rather simultaneously after the initial excitation from the pass of a large vehicles. This could be attributed to the plate stiff construction of the span and the placement of the markers on the guardrail rather than directly on the deck.

The corresponding deck deflection of the span during the passes' duration is illus-

trated in Figure 4.16. Time offset follows the segment in Figure 4.15 with 0.4 s interval between images which start just before the moment of excitation. The deflection shows downward movement during a large vehicle's pass with largest displacement consistently observed towards the center of the bridge span.

Table 4.3: Passing Large Vehicles.

Time (Vehicle ID)	Vehicle	Length [m]	Speed [km/h]
16:01 (24)		12.27	37.11
16:12 (171 and 57)		12.62	43.09
		12.36	39.38
16:18 (25)		8.26	36.65
16:22 (42 and 87)		7.94	42.36
		8.14	39.11

4.5   Conclusions

Application of video-based displacement measurement and traffic counting system was implemented on a plate-girder bridge to measure traffic-induced bridge deck displacement and vibration. The proposed system was able to measure structural displacement at sub-millimeter resolution on eight measurement points at once in the range of 40.8–64.2 m distance from a front-view camera.

Owing to the inability to directly measure vehicles' weight, the system instead relies on the estimated vehicle length to classify the traffic-induced structural displacement. A long-duration experiment was conducted for a 35 minutes on a 25-m-span steel road bridge when hundreds of cars passed on the bridge Notable displacement on the bridge could be observed from the passes of large vehicles in the lane closer to where the markers were installed, and less so from smaller vehicles and from the opposite lane. Vehicle-

induced frequency response could be observed more clearly from consecutive passes of large vehicle in the same lane.

Implementation with simpler image-based displacement measurement methods such as marker centroid tracking or phase correlation could be employed in the future to achieve real-time performance of the system for continuous in-situ structural health monitoring system.

(a)

(b)

(c)
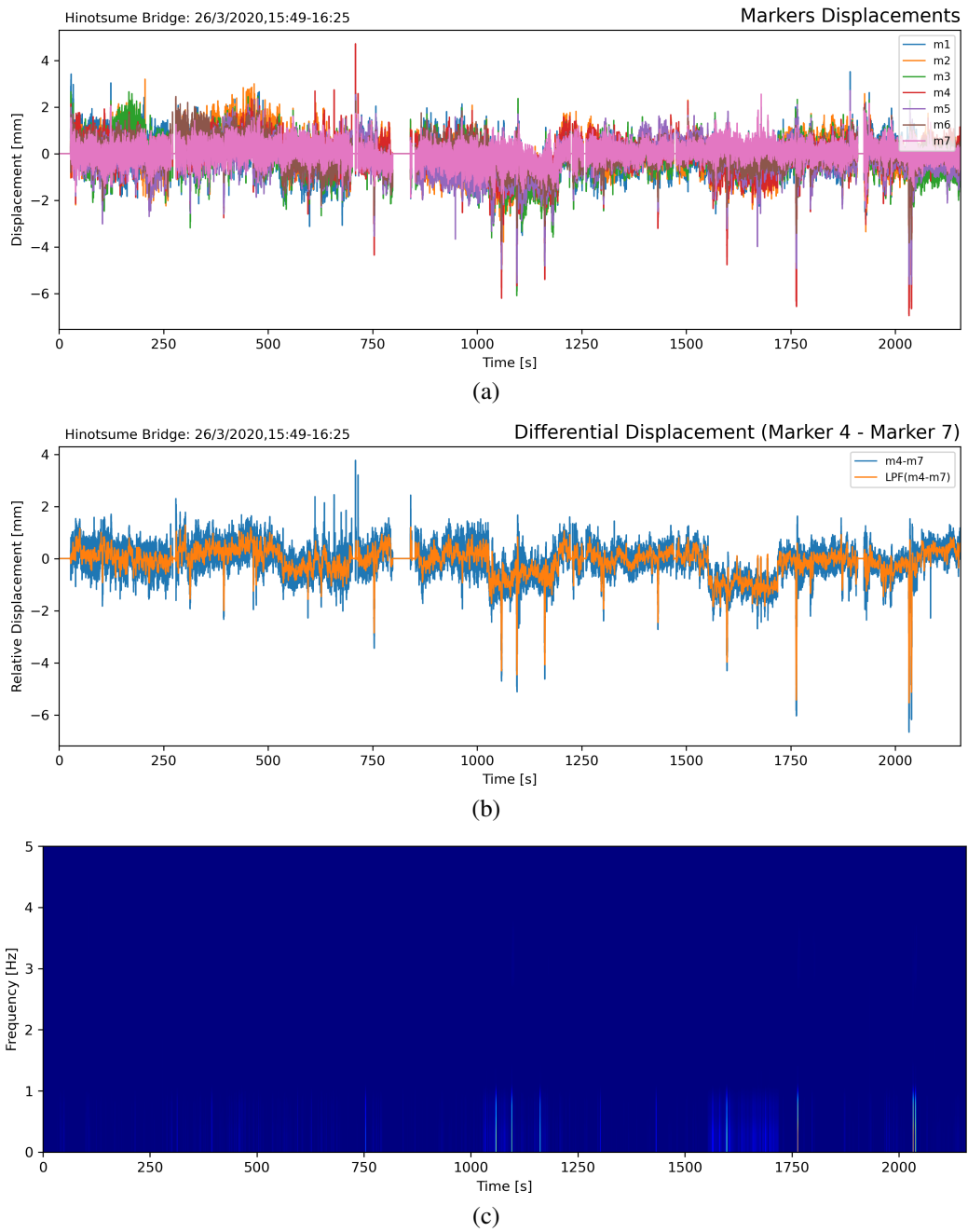
Figure 4.9: Raw displacement, differential displacement, and spectrogram of the vibration signal.
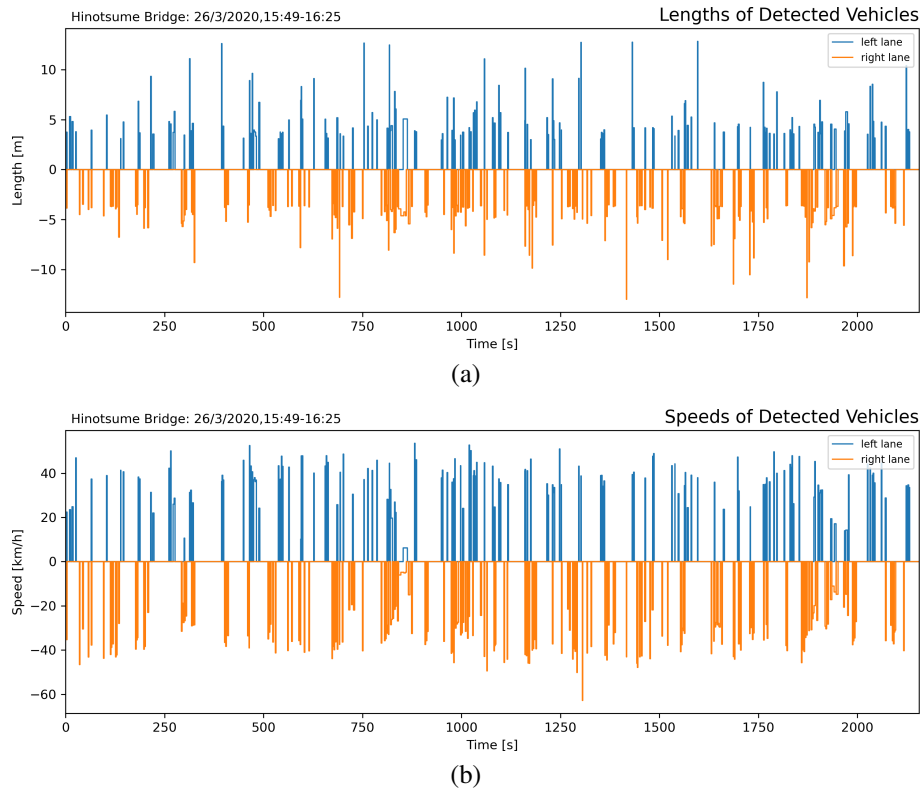
Figure 4.10: Length and passing speed of the detected vehicles in both lanes on the bridge.
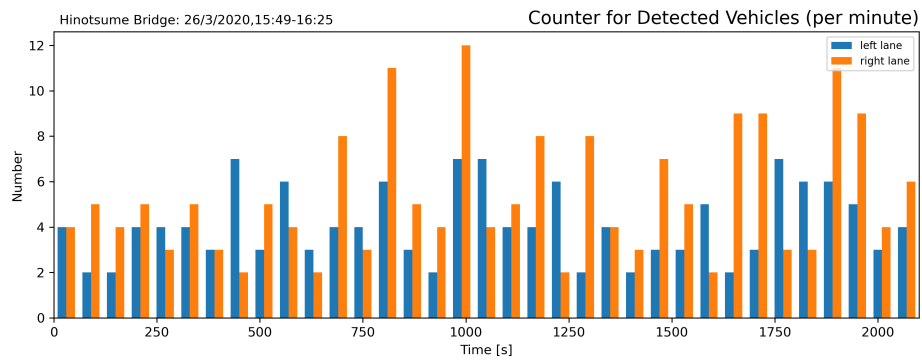
Figure 4.11: Traffic count in one minute segment.

(a)

(b)
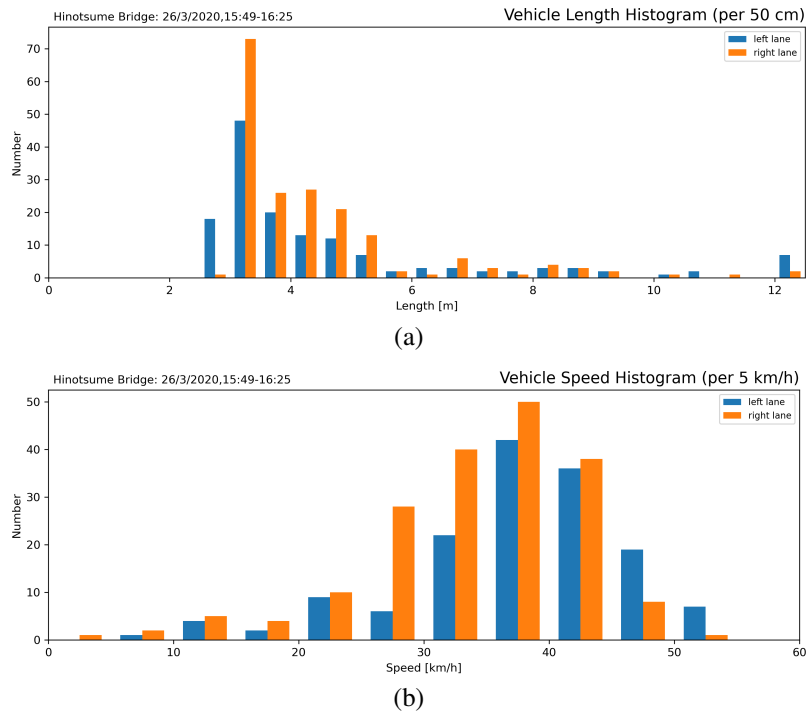
Figure 4.12: Vehicle length and passing speed histogram.

(a)

(b)
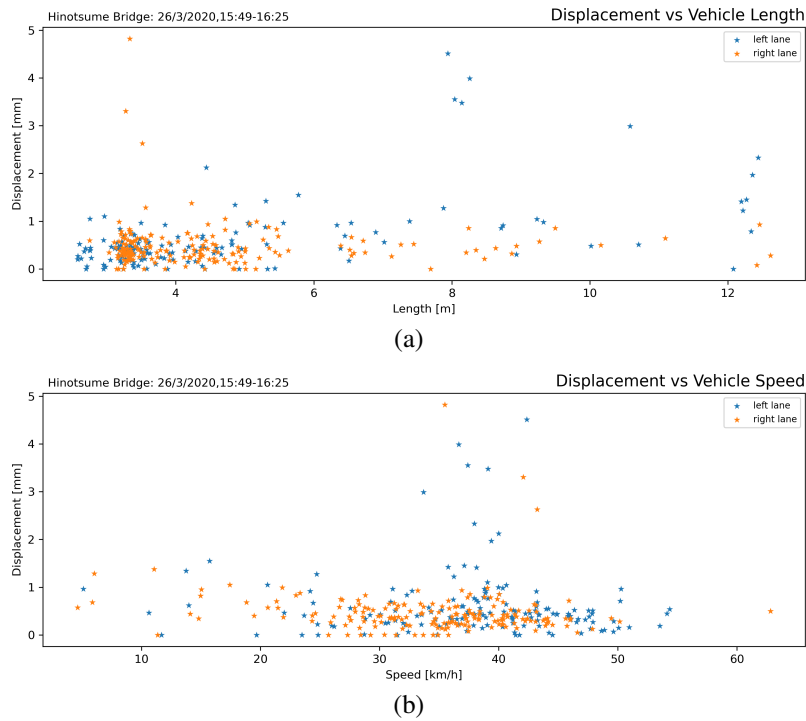
Figure 4.13: Bridge displacement according to vehicle lengths and passing speeds.
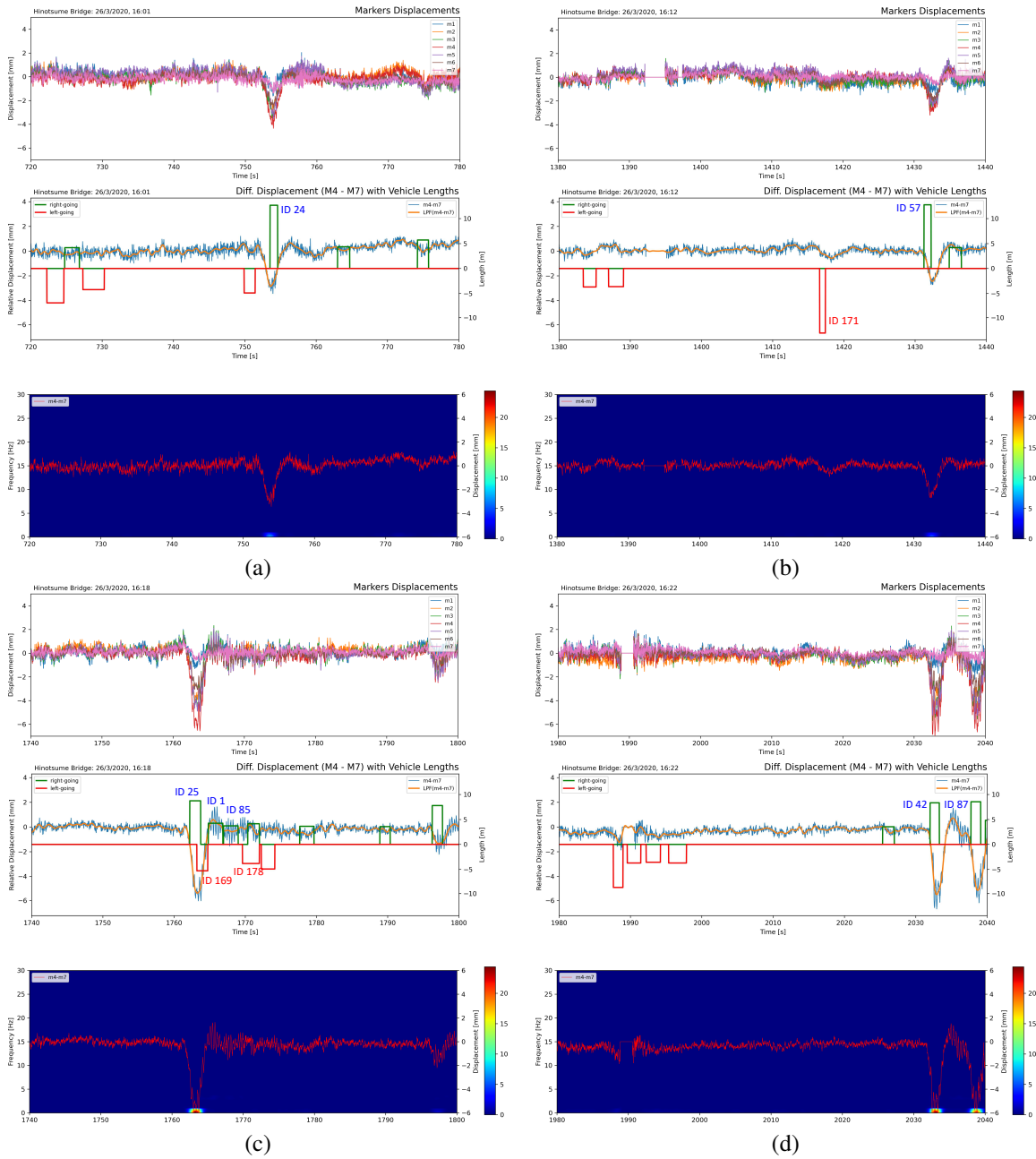
Figure 4.14: One minute segment of raw displacement, differential displacement, and vibration frequency response at 16:01, 16:12, 16:18, and 16:22.
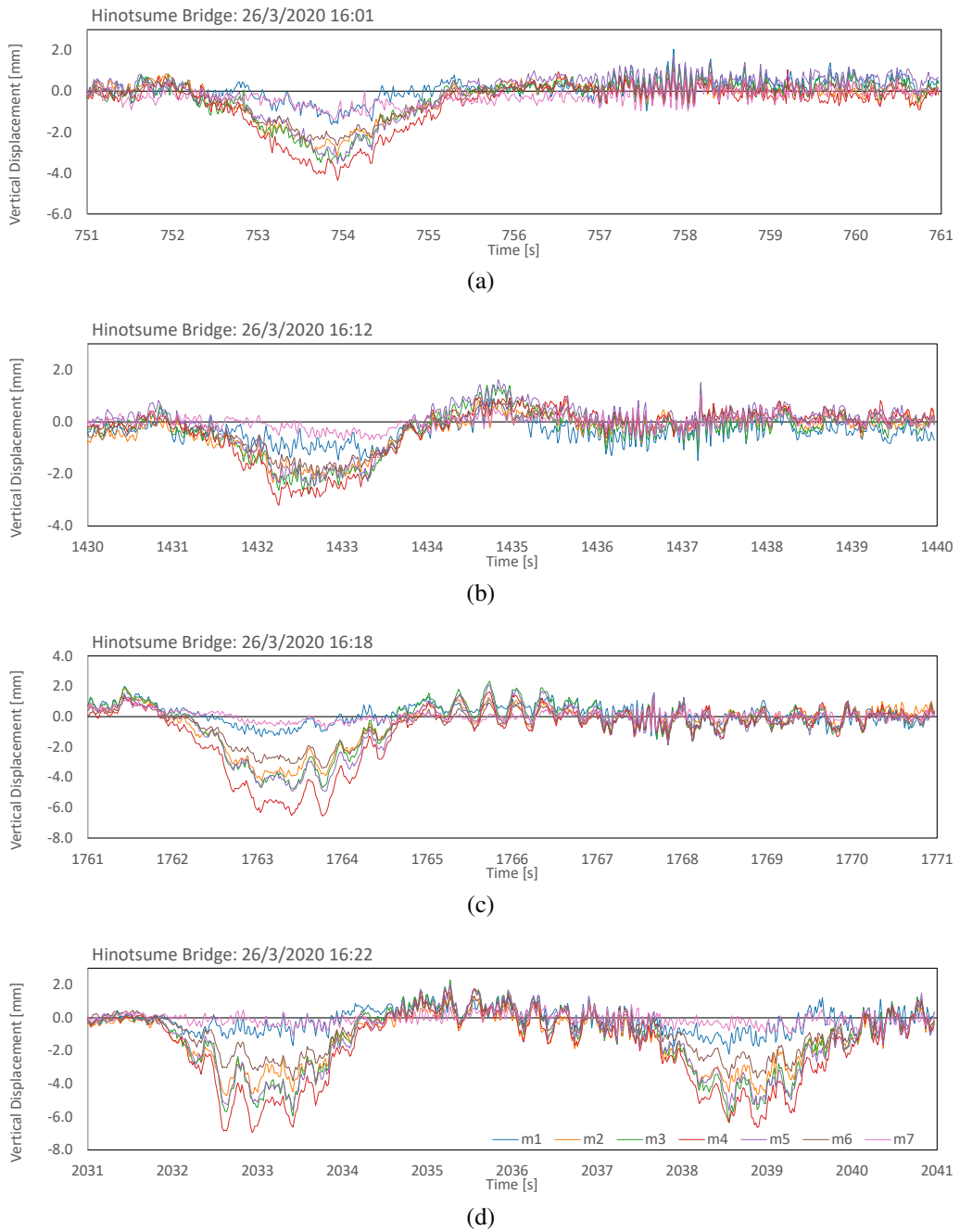
Figure 4.15: Ten second displacement upon large vehicles passes at 16:01, 16:12, 16:18, and 16:22.
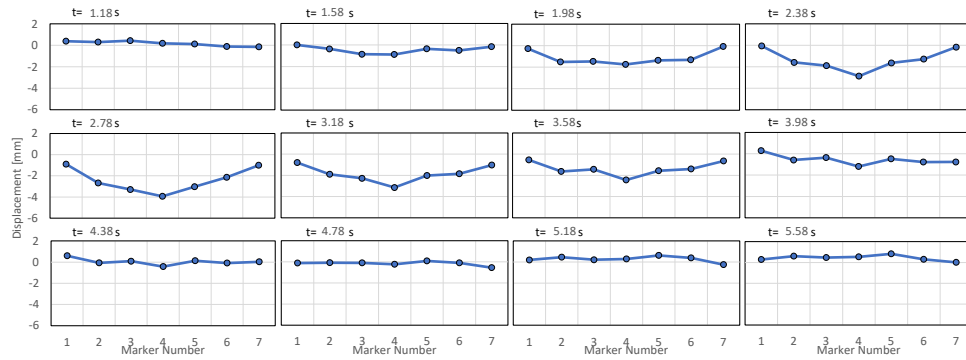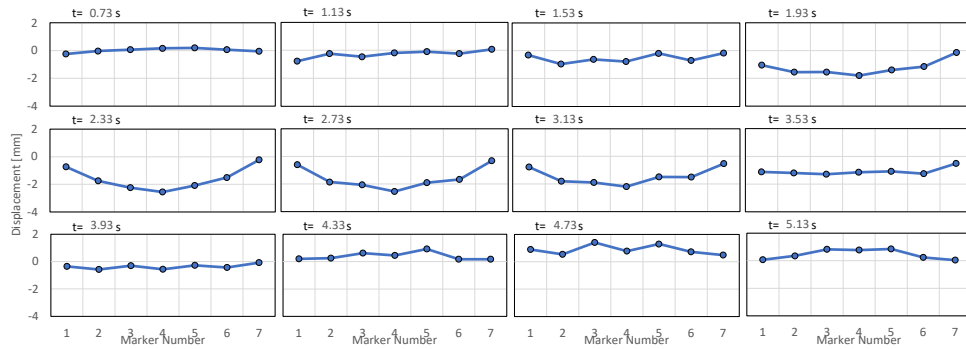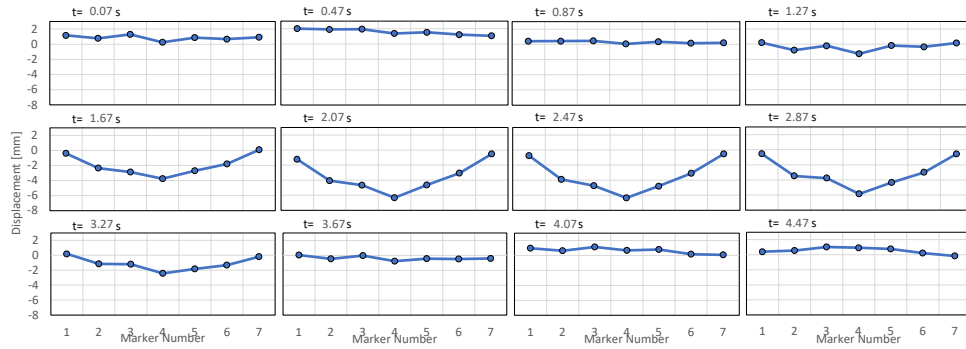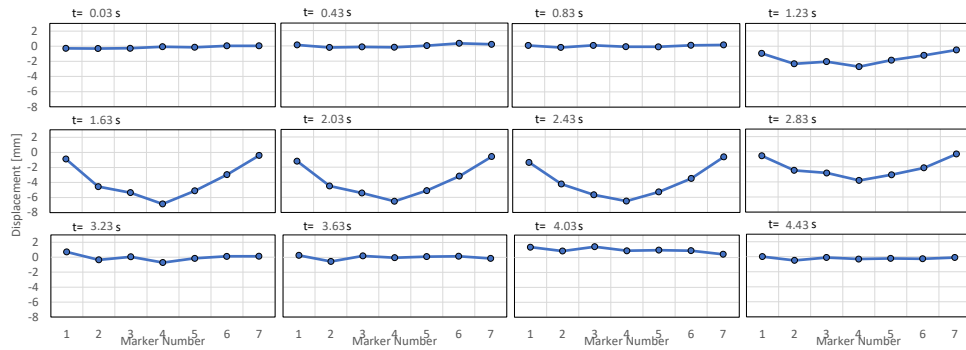
Figure 4.16: Bridge deck deflection at at 16:01, 16:12, 16:18, and 16:22.

Chapter 5

Conclusions and recommendations

Structural health monitoring is the process to maintain the safety and reliability of civil structures, by evaluating the overall structural integrity and detecting damages, both early and accumulated. Upon being applied to bridges, which serves important part in modern society, structural health monitoring can be done in various methods and approaches, ranging from routine inspection and contact sensors, to non-contact vision-based dynamic displacement measurement system. Vision system promises measurement with high sensitivity and accuracy, both in its temporal and spatial resolution.

Alternative placement of vision system frontal to the structure and tandem alignment of the markers along the optical axis of the vision system allows simultaneous measurement of lateral and vertical structural displacement across multiple points on a structure. The high contrast markers, in the forms of LEDs and corner cube prisms, allow reliable position extraction of the markers, even under short exposure of high frame rate vision system (180 fps and 240 fps). Experiment had been carried applied on a test structure to measure structural displacement distributed along one side of a test truss bridge. Frequency response and damping ratio has been evaluated from the obtained displacement measurement, both in lateral and vertical direction of the bridge vibration. The evaluation can provide the baseline condition of the structure vibration.

The optics parameters regarding permissible blur diameter and limitation of depth of field has been discussed in depth. By allowing certain degree of calculated focal blur in the captured image, depth of field of tandem-marker based displacement measurement system can be extended to cover a whole span of a test structure. Capturing structural

displacement distributed along two sides of a bridge model is possible by provision of collimated lighting device, half mirror on one side, and full plate mirror on the other side. Accuracy of the proposed system is within 4% of the actual displacement from 12 m measurement distance. Frequency response and modal shape analysis was conducted using Fast Fourier Transform and SSI-CPAST, respectively. Changes in frequency response and modal shape was observed from the different configurations of the deck of the model bridge.

Digital image correlation analysis was carried out to extract structural displacement of an actual bridge, by similarly placing the displacement measurement camera's optical axis almost parallel to the bridge's axis. The displacement measurement was complemented with traffic counting camera placed perpendicular to the bridge's axis, allowing full-length capturing of the passing vehicles. The traffic counting system can reliably detect and classify passing vehicles in the traffic based on the size of the vehicle. Effect of passing vehicles on the displacement and the frequency response of the structure is presented using differential displacement and frequency spectrogram. Only large and loaded vehicles exhibit notable displacement and frequency response on the bridge. It was found that no overloading and no excessive structural response occurred during the experiment.

The proposed vision-based distributed displacement measurement method is feasible for actual field application of structural health monitoring. Both single side and dual side configuration is possible to capture lateral and vertical displacement of structural members simultaneously. The implementation with high-speed camera and telephoto lens resulted in acceptable measurement spatial resolution for medium span bridges.

Several recommendations are suggested for the possible further studies concerning application of vision-system for structural health monitoring:

- overcoming the limitation of depth of field for application of very large structure using multiple cameras with parallel optical axis,

- image degradation resulting in false motion of the markers due to environment effect such as heat haze can be compensated to some extent using image correlation by minimizing the respective marker appearance's between frames,

- arrangement of more markers on different members and joints of the bridge to allow more complex shape of structural vibration,

- implementation with simpler image-based displacement measurement methods such as marker centroid tracking or phase correlation to achieve real-time performance of the system for continuous in-situ structural health monitoring system,

- verification of the measured dynamics of the onsite structure using finite element simulation or array of electronics sensors.

Bibliography

[1] Christopher Nonis, Christopher Niezrecki, Tzu-Yang Yu, Shafique Ahmed, Che-Fu Su, and Tim Schmidt. Structural health monitoring of bridges using digital image correlation. In Tribikram Kundu, editor, *Health Monitoring of Structural and Biological Systems*, page 869507, Apr 2013.

[2] Charles Seim. Bridge maintenance and safety: A practitioner's view. In Dan M. Frangopol and Richard Sause, editors, *Bridge maintenance, safety, management and life-cycle optimization*, pages 3–7. CRC Press, Boca Raton, Fla., 2010. OCLC: 845696436.

[3] H Bakamwesiga, J Mwakali, and S Thelandersson. Nondestructive condition assessment of highway bridges for safety enhancement. In *Bridge Maintenance, Safety, Management and Life Extension*, pages 1764–1771. CRC Press, May 2014.

[4] Charles R Farrar and Keith Worden. An introduction to structural health monitoring. *Philosophical Transactions of the Royal Society A: Mathematical, Physical and Engineering Sciences*, 365(1851):303–315, Feb 2007.

[5] Peter C. Chang, Alison Flatau, and S. C. Liu. Review paper: Health monitoring of civil infrastructure. *Structural Health Monitoring: An International Journal*, 2(3):257–267, Sep 2003.

[6] Ming Liu, Dan M. Frangopol, and Sunyong Kim. Bridge system performance assessment from structural health monitoring: A case study. *Journal of Structural Engineering*, 135(6):733–742, Jun 2009.

[7] Charles R Farrar and Keith Worden. An introduction to structural health monitoring. *Philosophical Transactions of the Royal Society A: Mathematical, Physical and Engineering Sciences*, 365(1851):303–315, Feb 2007.

[8] Tung Khuc and F. Necati Catbas. Completely contactless structural health monitoring of real-life structures using cameras and computer vision: Structural health

monitoring using computer vision. *Structural Control and Health Monitoring*, 24(1):e1852, Jan 2017.

[9] Shatirah Akib, MM Fayyadh, and HA Razak. Review of bridge vibration and future direction. *17th International Congress on Sound and Vibration (ICSV17), Cairo, Egypt, 18-22 July 2010 Doebling*, 4, Jul 2010.

[10] T. Yoshioka, M. Takahashi, H. Yamaguchi, and Y. Matsumoto. Damage assessment of truss diagonal members based on frequency changes in local higher modes. *Procedia Engineering*, 14:3119–3126, 2011.

[11] Sudath C. Siriwardane. Vibration measurement-based simple technique for damage detection of truss bridges: A case study. *Case Studies in Engineering Failure Analysis*, 4:50–58, 2015.

[12] Patrick Paultre. *Dynamics of Structures*. John Wiley & Sons, Inc, 2011.

[13] O.S. Salawu and C. Williams. Review of full-scale dynamic testing of bridge structures. *Engineering Structures*, 17(2):113–121, Feb 1995.

[14] Yang Deng, Aiqun Li, and Dongming Feng. Probabilistic damage detection of long-span bridges using measured modal frequencies and temperature. *International Journal of Structural Stability and Dynamics*, 18(10):1850126, Oct 2018.

[15] Chuan-Zhi Dong and F Necati Catbas. A review of computer vision–based structural health monitoring at local and global levels. *Structural Health Monitoring*, page 147592172093558, Jul 2020.

[16] Yan Xu, James M.W. Brownjohn, and Farhad Huseynov. Accurate deformation monitoring on bridge structures using a cost-effective sensing system combined with a camera and accelerometers: Case study. *Journal of Bridge Engineering*, 24(1):05018014, Jan 2019.

[17] Tadayoshi Aoyama, Makoto Chikaraishi, Akimasa Fujiwara, Liang Li, Mingjun Jiang, Kazuki Inoue, Takeshi Takaki, Idaku Ishii, Hua Yang, Chikako Umemoto,

and et al. Vibration sensing of a bridge model using a multithread active vision system. *IEEE/ASME Transactions on Mechatronics*, 23(1):179–189, Feb 2018.

[18] N. T. Khiem and L. K. Toan. A novel method for crack detection in beam-like structures by measurements of natural frequencies. *Journal of Sound and Vibration*, 333(18):4084–4103, 2014.

[19] Garrett Brunell and Yail J. Kim. Effect of local damage on the behavior of a laboratory-scale steel truss bridge. *Engineering Structures*, 48:281–291, 2013.

[20] Liang Wang. *INNOVATIVE DAMAGE ASSESSMENT OF STEEL TRUSS BRIDGES USING MODAL STRAIN ENERGY CORRELATION*. PhD thesis, Queensland University of Technology, 2012.

[21] Zhishen Wu, Suzhen Li, and Koichi Yokoyama. Advancement of bridge health monitoring based on distributed fiber optic sensors. In *2007 Japan Bridge Engineering Workshop*, page 13. Japanese Public Works Research Institute, 2007.

[22] Wasanthi R. Wickramasinghe, David P. Thambiratnam, Tommy H.T. Chan, and Theanh Nguyen. Vibration characteristics and damage detection in a suspension bridge. *Journal of Sound and Vibration*, 375:254–274, Aug 2016.

[23] Joel P. Conte, Xianfei He, Babak Moaveni, Sami F. Masri, John P. Caffrey, Mazen Wahbeh, Farzad Tasbihgoo, Daniel H. Whang, and Ahmed Elgamal. Dynamic Testing of Alfred Zampa Memorial Bridge. *Journal of Structural Engineering*, 134(6):1006–1015, jun 2008.

[24] Michael Fraser, Ahmed Elgamal, Xianfei He, and Joel P. Conte. Sensor Network for Structural Health Monitoring of a Highway Bridge. *Journal of Computing in Civil Engineering*, 24(1):11–24, jan 2010.

[25] Jian-Xiao Mao, Hao Wang, Dong-Ming Feng, Tian-You Tao, and Wen-Zhi Zheng. Investigation of dynamic properties of long-span cable-stayed bridges based on one-year monitoring data under normal operating condition. *Structural Control and Health Monitoring*, 25(5):e2146, May 2018.

[26] Sakib Mahmud Khan, Sez Atamturktur, Mashrur Chowdhury, and Mizanur Rahman. Integration of structural health monitoring and intelligent transportation systems for bridge condition assessment: Current status and future direction. *IEEE Transactions on Intelligent Transportation Systems*, 17(8):2107–2122, Aug 2016.

[27] P. Paultre, J. Proulx, and M. Talbot. Dynamic testing procedures for highway bridges using traffic loads. *Journal of Structural Engineering (United States)*, 121(2):362–376, 1995.

[28] Q Qin, H B Li, L Z Qian, and C K Lau. Modal Identification of Tsing Ma Bridge By Using Improved Eigensystem Realization Algorithm. *Journal of Sound and Vibration*, 247(2):325–341, 2001.

[29] Ki-Tae Park, Sang-Hyo Kim, Heung-Suk Park, and Kyu-Wan Lee. The determination of bridge displacement using measured acceleration. *Engineering Structures*, 27(3):371–378, 2005.

[30] C. Rainieri and G. Fabbrocino. Automated output-only dynamic identification of civil engineering structures. *Mechanical Systems and Signal Processing*, 24(3):678–695, 2010.

[31] CJ Brown and R Karuma. Monitoring of structures using the global positioning system. *Proceedings of the Institution of Civil Engineers Structures & Buildings*, 134(1):97–105, 1999.

[32] Gethin Wyn Roberts, Xiaolin Meng, and Alan Henry Dodson. Integrating a Global Positioning System and Accelerometers to Monitor the Deflection of Bridges. *Journal of Surveying Engineering*, 130(2):65–72, 2004.

[33] A. Nickitopoulou, K. Protopsalti, and S. Stiros. Monitoring dynamic and quasi-static deformations of large flexible engineering structures with GPS: Accuracy, limitations and promises. *Engineering Structures*, 28(10):1471–1482, 2006.

[34] X. Meng, A. H. Dodson, and G. W. Roberts. Detecting bridge dynamics with GPS and triaxial accelerometers. *Engineering Structures*, 29(11):3178–3184, 2007.

[35] H. Xia, G. De Roeck, N. Zhang, and J. Maeck. Experimental analysis of a high-speed railway bridge under Thalys trains. *Journal of Sound and Vibration*, 268(1):103–113, 2003.

[36] Hani H. Nassif, Mayrai Gindy, and Joe Davis. Comparison of laser Doppler vibrometer with contact sensors for monitoring bridge deflection and vibration. *NDT and E International*, 38(3):213–218, 2005.

[37] Jose L. Valin, Edison Gonçalves, Francisco Palacios, and Jorge Ricardo Pérez. Methodology for analysis of displacement using digital holography. *Optics and Lasers in Engineering*, 43(1):99–111, 2005.

[38] Fabio Casciati and Lijun Wu. Local positioning accuracy of laser sensors for structural health monitoring. *Structural Control and Health Monitoring*, 20(5):728–739, 2013.

[39] M. Pieraccini, M. Fratini, F. Parrini, G. Macaluso, and C. Atzeni. High-speed cw step-frequency coherent radar for dynamic monitoring of civil engineering structures. *Electronics Letters*, 40(14):907–908, July 2004.

[40] Carmelo Gentile and Giulia Bernardini. An interferometric radar for non-contact measurement of deflections on civil engineering structures: laboratory and full-scale tests. *Structure and Infrastructure Engineering*, 6(5):521–534, 2010.

[41] G. T. Webb, P. J. Vardanega, and C. R. Middleton. Categories of SHM Deployments: Technologies and Capabilities. *Journal of Bridge EnginQeering*, 20(11):04014118, 2015.

[42] A. Mazen Wahbeh, John P Caffrey, and Sami F Masri. A vision-based approach for the direct measurement of displacements in vibrating systems. *Smart Materials and Structures*, 12:785–794, 2003.

[43] Sandeep Sony, Shea Laventure, and Ayan Sadhu. A literature review of next-generation smart sensing technology in structural health monitoring. *Structural Control and Health Monitoring*, 26(3):e2321, Mar 2019.

[44] Timothy J. Beberniss and David A. Ehrhardt. High-speed 3D digital image correlation vibration measurement: Recent advancements and noted limitations. *Mechanical Systems and Signal Processing*, 86:35–48, mar 2017.

[45] Longxi Luo and Maria Q. Feng. Edge-enhanced matching for gradient-based computer vision displacement measurement: Edge-enhanced matching. *Computer-Aided Civil and Infrastructure Engineering*, 33(12):1019–1040, Dec 2018.

[46] Dongming Feng and Maria Q. Feng. Experimental validation of cost-effective vision-based structural health monitoring. *Mechanical Systems and Signal Processing*, 88:199–211, May 2017.

[47] Dongming Feng and Maria Q. Feng. Computer vision for SHM of civil infrastructure: From dynamic response measurement to damage detection – A review. *Engineering Structures*, 156:105–117, February 2018.

[48] Marcin Malesa, Krzysztof Malowany, Jakub Pawlicki, Malgorzata Kujawinska, Pawel Skrzypczak, Artur Piekarczuk, Tomasz Lusa, and Andrzej Zagorski. Nondestructive testing of industrial structures with the use of multi-camera digital image correlation method. *Engineering Failure Analysis*, 69:122–134, Nov 2016.

[49] Insub Choi, Jun Hee Kim, and Donghyun Kim. A target-less vision-based displacement sensor based on image convex hull optimization for measuring the dynamic response of building structures. *Sensors (Switzerland)*, 16(12):1–17, 2016.

[50] Katsuhisa Kanda, Yuji Miyamoto, Akihiro Kondo, and Makoto Oshio. Monitoring of earthquake induced motions and damage with optical motion tracking. *Smart Materials and Structures*, 14(3):S32–S38, Jun 2005.

[51] D. Ribeiro, R. Calçada, J. Ferreira, and T. Martins. Non-contact measurement of the dynamic displacement of railway bridges using an advanced video-based system. *Engineering Structures*, 75:164–180, Sep 2014.

[52] C Almeida Santos, C Oliveira Costa, and J Batista. A vision-based system for measuring the displacements of large structures: Simultaneous adaptive calibration and full motion estimation. *Mechanical Systems and Signal Processing*, 72–73:678–694, 2016.

[53] Dongming Feng and Maria Q. Feng. Computer vision for shm of civil infrastructure: From dynamic response measurement to damage detection – a review. *Engineering Structures*, 156:105–117, Feb 2018.

[54] Zulhaj Aliansyah, Mingjun Jiang, Takeshi Takaki, and Idaku Ishii. High-speed Vision System for Dynamic Structural Distributed Displacement Analysis. *J. Phys.: Conf. Ser.*, 1075:012014, August 2018.

[55] Zhai Yusheng, Zhang Zhifeng, Su Yuling, Wang Xinjie, and Feng Qibo. A high-precision roll angle measurement method. *Optik*, 126(24):4837–4840, December 2015.

[56] A. Missoffe, L. Chassagne, S. Topçu, P. Ruaux, B. Cagneau, and Y. Alayli. New simple optical sensor: From nanometer resolution to centimeter displacement range. *Sensors and Actuators A: Physical*, 176:46–52, April 2012.

[57] Grzegorz Zamiela and Marek Dobosz. Corner cube reflector lateral displacement evaluation simultaneously with interferometer length measurement. *Optics & Laser Technology*, 50:118–124, September 2013.

[58] Dongming Feng, Maria Q. Feng, Ekin Ozer, and Yoshio Fukuda. A vision-based sensor for noncontact structural displacement measurement. *Sensors (Switzerland)*, 15(7):16557–16575, 2015.

[59] R. Ditommaso and F. C. Ponzo. Automatic evaluation of the fundamental frequency variations and related damping factor of reinforced concrete framed structures using the Short Time Impulse Response Function (STIRF). *Engineering Structures*, 82:104–112, 2015.

[60] Monica Carfagni, Edoardo Lenzi, and Marco Pierini. The Loss Factor as a Measure of Mechanical Damping. *Proc. SPIE*, 3243:5, February 1998.

[61] G. A. Stephen, J. M W Brownjohn, and C. A. Taylor. Measurements of static and dynamic displacement from visual monitoring of the Humber Bridge. *Engineering Structures*, 15(3):197–208, 1993.

[62] Piotr Olaszek. Investigation of the dynamic characteristic of bridge structures using a computer vision method. *Measurement*, 25:227–236, 1999.

[63] J. J. Lee and M. Shinozuka. Real-Time Displacement Measurement of a Flexible Bridge Using Digital Image Processing Techniques. *Experimental Mechanics*, 46:105–114, 2006.

[64] P. Kohut, K. Holak, T. Uhl, L. Ortyl, T. Owerko, P. Kuras, and R. Kocierz. Monitoring of a civil structure's state based on noncontact measurements. *Structural Health Monitoring*, 12(5-6):411–429, 2013.

[65] Dongming Feng, Maria Q. Feng, Ekin Ozer, and Yoshio Fukuda. A vision-based sensor for noncontact structural displacement measurement. *Sensors (Switzerland)*, 15(7):16557–16575, 2015.

[66] Y F Ji and C C Chang. Nontarget image-based technique for small cable vibration measurement. *Journal of Bridge Engineering*, 13(1):34–42, 2008.

[67] S.-W. Kim, B.-G. Jeon, N.-S. Kim, and J.-C. Park. Vision-based monitoring system for evaluating cable tensile forces on a cable-stayed bridge. *Structural Health Monitoring*, 12(5-6):440–456, 2013.

[68] Long Tian and Bing Pan. Remote bridge deflection measurement using an advanced video deflectometer and actively illuminated LED targets. *Sensors (Switzerland)*, 16(9):1–13, 2016.

[69] G. Busca, A. Cigada, P. Mazzoleni, and E. Zappa. Vibration Monitoring of Multiple Bridge Points by Means of a Unique Vision-Based Measuring System. *Experimental Mechanics*, 54(2):255–271, 2014.

[70] Yi-Zhe Song, Chris R Bowen, Alicia H Kim, Aydin Nassehi, Julian Padget, and Nick Gathercole. Virtual visual sensors and their application in structural health monitoring. *Structural Health Monitoring*, 13(3):251–264, 2014.

[71] Yoshio Fukuda, Maria Q Feng, Yuto Narita, and Takayuki Tanaka. Vision-Based Displacement Sensor for Monitoring Dynamic Response Using Robust Object Search Algorithm. *IEEE Sensors Journal*, 13(12):4725–4732, 2013.

[72] Jong Jae Lee, Hoai Nam Ho, and Jong Han Lee. A vision-based dynamic rotational angle measurement system for large civil structures. *Sensors (Switzerland)*, 12(6):7326–7336, 2012.

[73] H. A. Bruck, S. R. McNeill, M. A. Sutton, and W. H. Peters. Digital image correlation using Newton-Raphson method of partial differential correction. *Experimental Mechanics*, 29(3):261–267, 1989.

[74] C. Quentin Davis. Statistics of subpixel registration algorithms based on spatiotemporal gradients or block matching. *Optical Engineering*, 37:1290, 1998.

[75] Hassan Foroosh, Josiane B. Zerubia, and Marc Berthod. Extension of phase correlation to subpixel registration. *IEEE Transactions on Image Processing*, 11(3):188–199, 2002.

[76] Alan Pilch, Ajay Mahajan, and Tsuchin Chu. Measurement of Whole-Field Surface Displacements and Strain Using a Genetic Algorithm Based Intelligent Image Correlation Method. *Journal of Dynamic Systems, Measurement, and Control*, 126(3):479–488, 2004.

[77] Pan Bing, Xie Hui-min, Xu Bo-qin, and Dai Fu-long. Performance of sub-pixel registration algorithms in digital image correlation. *Measurement Science and Technology*, 17(6):1615–1621, 2006.

[78] Longxi Luo and Maria Q. Feng. Vision based displacement sensor with heat haze filtering capability. In *Structural Health Monitoring 2017*. DEStech Publications, Inc., Sep 2017.

[79] Tadayoshi Aoyama, Liang Li, Mingjun Jiang, Kazuki Inoue, Takeshi Takaki, Idaku Ishii, Hua Yang, Chikako Umemoto, Hiroshi Matsuda, Makoto Chikaraishi, and Akimasa Fujiwara. Vibration Sensing of a Bridge Model Using a Multithread Active Vision System. *IEEE/ASME Transactions on Mechatronics*, 23(1):179–189, 2017.

[80] Yang Shang, Qifeng Yu, Zhen Yang, Zhiqiang Xu, and Xiaohu Zhang. Displacement and deformation measurement for large structures by camera network. *Optics and Lasers in Engineering*, 54:247–254, 2014.

[81] Marcin Malesa, Krzysztof Malowany, Jakub Pawlicki, Malgorzata Kujawinska, Pawel Skrzypczak, Artur Piekarczuk, Tomasz Lusa, and Andrzej Zagorski. Nondestructive testing of industrial structures with the use of multi-camera digital image correlation method. *Engineering Failure Analysis*, 69:122–134, Nov 2016.

[82] Jean Michel Franco, Byron Mauricio Mayag, Johannio Marulanda, and Peter Thomson. Static and dynamic displacement measurements of structural elements using low cost RGB-D cameras. *Engineering Structures*, 153(February):97–105, 2017.

[83] Krzysztof Malowany, Marcin Malesa, Tomasz Kowaluk, and Malgorzata Kujawinska. Multi-camera digital image correlation method with distributed fields of view. *Optics and Lasers in Engineering*, 98(July):198–204, 2017.

[84] P Kohut and P Kurowski. Application of modal analysis supported by 3D vision-based measurements. *Journal of Theoretical and Applied Mechanics*, 47(4):pp. 855–870, 2009.

[85] Joseph Morlier and Guilhem Michon. Virtual Vibration Measurement Using KLT

Motion Tracking Algorithm. *Journal of Dynamic Systems, Measurement, and Control*, 132(1):011003, 2010.

[86] Peter Avitabile, Chris Niezrecki, Mark Helfrick, Chris Warren, and Pawan Pingle. Noncontact Measurement Techniques for Model Correlation. *Test*, 44(January):8–12, 2010.

[87] E. Caetano, S. Silva, and J. Bateira. A vision system for vibration monitoring of civil engineering structures. *Experimental Techniques*, 35(4):74–82, 2011.

[88] Hua Yang, Qingyi Gu, Tadayoshi Aoyama, Takeshi Takaki, and Idaku Ishii. Dynamics-Based Stereo Visual Inspection Using Multidimensional Modal Analysis. *IEEE SENSORS*, 13(12):4831–4843, 2013.

[89] Justin G. Chen, Neal Wadhwa, Young Jin Cha, Frédo Durand, William T. Freeman, and Oral Buyukozturk. Modal identification of simple structures with high-speed video using motion magnification. *Journal of Sound and Vibration*, 345:58–71, 2015.

[90] Dashan Zhang, Jie Guo, Xiujun Lei, and Changan Zhu. A high-speed vision-based sensor for dynamic vibration analysis using fast motion extraction algorithms. *Sensors (Switzerland)*, 16(4), 2016.

[91] Jianing Hao. Natural vibration analysis of long span suspension bridges. In *Advances in Engineering Research*, volume 135, page 1059–1062, 2017.

[92] Mitsuo Kawatani, Chul-Woo Kim, Naoki Kawada, and Shohei Koga. Assessment of traffic-induced low frequency noise radiated from steel box girder bridge. *Int. J. Steel Structure*, 8(4):305–314, 2008.

[93] Jian-Xiao Mao, Hao Wang, Dong-Ming Feng, Tian-You Tao, and Wen-Zhi Zheng. Investigation of dynamic properties of long-span cable-stayed bridges based on one-year monitoring data under normal operating condition. *Structural Control and Health Monitoring*, 25(5):e2146, May 2018.

[94] Ge-Wei Chen, Sherif Beskhyroun, and Piotr Omenzetter. Experimental investigation into amplitude-dependent modal properties of an eleven-span motorway bridge. *Engineering Structures*, 107:80–100, Jan 2016.

[95] Hua Yang, Takeshi Takaki, and Idaku Ishii. Simultaneous dynamics-based visual inspection using modal parameter estimation. *Journal of Robotics and Mechatronics*, 23, 02 2011.

[96] Hua Yang, Idaku Ishii, and Takeshi Takaki. Real-time vision-based modal parameters estimation at 10000 fps. In Masayoshi Tomizuka, Chung-Bang Yun, and Jerome P. Lynch, editors, *Sensors and Smart Structures Technologies for Civil, Mechanical, and Aerospace Systems*, page 83454F, Apr 2012.

[97] Zulhaj Aliansyah, Kohei Shimasaki, Mingjun Jiang, Takeshi Takaki, Idaku Ishii, Hua Yang, Chikako Umemoto, and Hiroshi Matsuda. A Tandem Marker-Based Motion Capture Method for Dynamic Small Displacement Distribution Analysis. *Journal of Robotics and Mechatronics*, 31(5):671–685, oct 2019.

[98] AASHTO. *AASHTO LRFD Bridge Design Specifications, U.S. Customary Units (7th Edition)*. American Association of State Highway and Transportation Officials (AASHTO), 2014. OCLC: 1096911575.

[99] Alessandra Fiore and Giuseppe Carlo Marano. Serviceability Performance Analysis of Concrete Box Girder Bridges Under Traffic-Induced Vibrations by Structural Health Monitoring: A Case Study. *International Journal of Civil Engineering*, 16(5):553–565, may 2018.

[100] Johannes Salvermoser, Céline Hadziioannou, and Simon C. Stähler. Structural monitoring of a highway bridge using passive noise recordings from street traffic. *The Journal of the Acoustical Society of America*, 138(6):3864–3872, dec 2015.

[101] David Hester and Arturo González. A discussion on the merits and limitations of using drive-by monitoring to detect localised damage in a bridge. *Mechanical Systems and Signal Processing*, 90:234–253, jun 2017.

[102] Luna Ngeljaratan and Mohamed A. Moustafa. System Identification of Large-Scale Bridges Using Target-Tracking Digital Image Correlation. *Frontiers in Built Environment*, 5:85, jun 2019.

[103] Renaude Carneiro dos Santos, Ana Paula C. Larocca, João Olympio de Araújo Neto, Augusto César Barros Barbosa, and José Venâncio Marra Oliveira. Detection of a curved bridge deck vibration using robotic total stations for structural health monitoring. *Journal of Civil Structural Health Monitoring*, 9(1):63–76, feb 2019.

[104] Piotr Górski, Monika Napieraj, and Eduard Konopka. Variability evaluation of dynamic characteristics of highway steel bridge based on daily traffic-induced vibrations. *Measurement*, 164:108074, nov 2020.

[105] Yang Deng, Aiqun Li, and Dongming Feng. Probabilistic Damage Detection of Long-Span Bridges Using Measured Modal Frequencies and Temperature. *International Journal of Structural Stability and Dynamics*, 18(10):1850126, oct 2018.

[106] E. Peter Carden and Paul Fanning. Vibration Based Condition Monitoring: A Review. *Structural Health Monitoring: An International Journal*, 3(4):355–377, dec 2004.

[107] Eugene OBrien, Ciaran Carey, and Jennifer Keenahan. Bridge damage detection using ambient traffic and moving force identification: Bridge Damage Detection and Moving Force Identification. *Structural Control and Health Monitoring*, 22(12):1396–1407, dec 2015.

[108] Fabrizio Gara, Vanni Nicoletti, Davide Roia, Luigino Dezi, and Andrea Dall'Asta. Dynamic monitoring of an isolated steel arch bridge during static load test. In *2016 IEEE Workshop on Environmental, Energy, and Structural Monitoring Systems (EESMS)*, pages 1–6, Bari, Italy, jun 2016. IEEE.

[109] Eric V. Fernstrom, Tim R. Wank, and Kirk A. Grimmelsman. Dynamic Testing of a Truss Bridge Using a Vibroseis Truck. In J.M. Caicedo, F.N. Catbas, A. Cunha,

V. Racic, P. Reynolds, and K. Salyards, editors, *Topics on the Dynamics of Civil Structures, Volume 1*, pages 155–163. Springer New York, New York, NY, 2012.

[110] Ahmed Elhattab, Nasim Uddin, and Eugene OBrien. Drive-By Bridge Frequency Identification under Operational Roadway Speeds Employing Frequency Independent Underdamped Pinning Stochastic Resonance (FI-UPSR). *Sensors*, 18(12):4207, nov 2018.

[111] Abdollah Malekjafarian and Eugene J. OBrien. On the use of a passing vehicle for the estimation of bridge mode shapes. *Journal of Sound and Vibration*, 397:77–91, jun 2017.

[112] Hoai Ho and Mayuko Nishio. Evaluation of dynamic responses of bridges considering traffic flow and surface roughness. *Engineering Structures*, 225:111256, dec 2020.

[113] Daniel Cantero, Patrick McGetrick, Chul-Woo Kim, and Eugene OBrien. Experimental monitoring of bridge frequency evolution during the passage of vehicles with different suspension properties. *Engineering Structures*, 187:209–219, may 2019.

[114] P J McGetrick, A González, and E J OBrien. Theoretical investigation of the use of a moving vehicle to identify bridge dynamic parameters. *Insight - Non-Destructive Testing and Condition Monitoring*, 51(8):433–438, aug 2009.

[115] Soheil Sadeghi Eshkevari, Thomas J. Matarazzo, and Shamim N. Pakzad. Simplified vehicle–bridge interaction for medium to long-span bridges subject to random traffic load. *Journal of Civil Structural Health Monitoring*, 10(4):693–707, sep 2020.

[116] Khatereh Vaghefi, Renee C. Oats, Devin K. Harris, Theresa (Tess) M. Ahlborn, Colin N. Brooks, K. Arthur Endsley, Christopher Roussi, Robert Shuchman, Joseph W. Burns, and Richard Dobson. Evaluation of Commercially Available

Remote Sensors for Highway Bridge Condition Assessment. *Journal of Bridge Engineering*, 17(6):886–895, nov 2012.

[117] Sze-Wei Khoo, Saravanan Karuppanan, and Ching-Seong Tan. A Review of Surface Deformation and Strain Measurement Using Two-Dimensional Digital Image Correlation. *Metrology and Measurement Systems*, 23(3):461–480, sep 2016.

[118] W. Tong. Formulation of Lucas-Kanade Digital Image Correlation Algorithms for Non-contact Deformation Measurements: A Review: Lucas-Kanade Digital Image Correlation Algorithms. *Strain*, 49(4):313–334, aug 2013.

[119] Bing Pan, LiPing Yu, and QianBing Zhang. Review of single-camera stereo-digital image correlation techniques for full-field 3D shape and deformation measurement. *Science China Technological Sciences*, 61(1):2–20, jan 2018.

[120] Bing Pan. Digital image correlation for surface deformation measurement: historical developments, recent advances and future goals. *Measurement Science and Technology*, 29(8):082001, aug 2018.

[121] D.H. Diamond, P.S. Heyns, and A.J. Oberholster. Accuracy evaluation of sub-pixel structural vibration measurements through optical flow analysis of a video sequence. *Measurement*, 95:166–172, jan 2017.

[122] Bora Gencturk, Kazi Hossain, Aadit Kapadia, Emad Labib, and Yi-Lung Mo. Use of digital image correlation technique in full-scale testing of prestressed concrete structures. *Measurement*, 47:505–515, jan 2014.

[123] M. Hamrat, B. Boulekbache, M. Chemrouk, and S. Amziane. Flexural cracking behavior of normal strength, high strength and high strength fiber concrete beams, using Digital Image Correlation technique. *Construction and Building Materials*, 106:678–692, mar 2016.

[124] Bing Pan, Kemao Qian, Huimin Xie, and Anand Asundi. Two-dimensional digital image correlation for in-plane displacement and strain measurement: a review. *Measurement Science and Technology*, 20(6):062001, jun 2009.

[125] T M Ahlborn, D K Harris, K Vaghefi, and R C Oats. An Evaluation of Commercially Available Remote Sensors for Assessing Highway Bridge Condition. Technical report, Michigan Technological University, oct 2010.

[126] Longxi Luo, Maria Q. Feng, and Zheng Y. Wu. Robust vision sensor for multi-point displacement monitoring of bridges in the field. *Engineering Structures*, 163:255–266, may 2018.

[127] Longxi Luo, Maria Q. Feng, and Jianping Wu. A comprehensive alleviation technique for optical-turbulence-induced errors in vision-based displacement measurement. *Structural Control and Health Monitoring*, 27(3), mar 2020.

[128] Mareike Kohm and Lothar Stempniewski. Beam tests for a wireless modal-based bridge monitoring system. In *The Evolving Metropolis*, volume 114, page 669–682, Sep 2019.

[129] Zhengmi Tang, Kohei Shimasaki, Mingjun Jiang, Takeshi Takaki, Idaku Ishii, Aoi Koga, and Hiroshi Matsuda. Ironworks Conveyor Monitoring Using Mirror-drive High-speed Active Vision. *ISIJ International*, 60(5):960–970, may 2020.

[130] Patrizia Bellucci and Ernesto Cipriani. Data accuracy on automatic traffic counting: the SMART project results. *European Transport Research Review*, 2(4):175–187, dec 2010.

[131] Ahmad Arinaldi, Jaka Arya Pradana, and Arlan Arventa Gurusinga. Detection and classification of vehicles for traffic video analytics. *Procedia Computer Science*, 144:259–268, 2018.

[132] Erhan Ince. Measuring traffic flow and classifying vehicle types: A surveillance video based approach. *Turkish Journal of Electrical Engineering and Computer Science*, 19(4):607–620, 2011.

[133] Hana Rabbouch, Foued Saâdaoui, and Rafaa Mraihi. Unsupervised video summarization using cluster analysis for automatic vehicles counting and recognizing. *Neurocomputing*, 260:157–173, oct 2017.

[134] Fei Liu, Zhiyuan Zeng, and Rong Jiang. A video-based real-time adaptive vehicle-counting system for urban roads. *PLOS ONE*, 12(11):e0186098, nov 2017.

[135] Nipjyoti Bharadwaj, Pallav Kumar, Shriniwas Arkatkar, Akhiles Maurya, and Gaurang Joshi. Traffic data analysis using image processing technique on Delhi–Gurgaon expressway. *Current Science*, 110(5):16, mar 2016.

[136] Huiyuan Fu, Huadong Ma, Yinxin Liu, and Dawei Lu. A vehicle classification system based on hierarchical multi-SVMs in crowded traffic scenes. *Neurocomputing*, 211:182–190, oct 2016.

[137] Takaya Kawakatsu, Akira Kakitani, Kenro Aihara, Atsuhiro Takasu, and Jun Adachi. Traffic Surveillance System for Bridge Vibration Analysis. In *2017 IEEE International Conference on Information Reuse and Integration (IRI)*, pages 69–74, San Diego, CA, aug 2017. IEEE.

[138] Jia-Ping Lin and Min-Te Sun. A YOLO-Based Traffic Counting System. In *2018 Conference on Technologies and Applications of Artificial Intelligence (TAAI)*, pages 82–85, Taichung, nov 2018. IEEE.

[139] Maojin Sun, Yan Wang, Teng Li, Jing Lv, and Jun Wu. Vehicle counting in crowded scenes with multi-channel and multi-task convolutional neural networks. *Journal of Visual Communication and Image Representation*, 49:412–419, nov 2017.

[140] Sakib Mahmud Khan, Sez Atamturktur, Mashrur Chowdhury, and Mizanur Rahman. Integration of Structural Health Monitoring and Intelligent Transportation Systems for Bridge Condition Assessment: Current Status and Future Direction. *IEEE Transactions on Intelligent Transportation Systems*, 17(8):2107–2122, aug 2016.

[141] Chuan-Zhi Dong, Selcuk Bas, and F. Necati Catbas. A portable monitoring approach using cameras and computer vision for bridge load rating in smart cities. *Journal of Civil Structural Health Monitoring*, 10(5):1001–1021, nov 2020.

[142] Chien-Chou Chen, Wen-Hwa Wu, Hong-Zeng Tseng, Chi-Hong Chen, and Gwo-long Lai.   Application of digital photogrammetry techniques in identifying the mode shape ratios of stay cables with multiple camcorders. *Measurement*, 75:134–146, nov 2015.

[143] F. Necati Catbas, Ricardo Zaurin, Mustafa Gul, and Hasan Burak Gokce. Sensor Networks, Computer Imaging, and Unit Influence Lines for Structural Health Monitoring: Case Study for Bridge Load Rating. *Journal of Bridge Engineering*, 17(4):662–670, jul 2012.

[144] Ricardo Zaurin, Tung Khuc, and F. Necati Catbas. Hybrid Sensor-Camera Monitoring for Damage Detection: Case Study of a Real Bridge. *Journal of Bridge Engineering*, 21(6):05016002, jun 2016.

[145] Liangfu Ge, Danhui Dan, and Hui Li. An accurate and robust monitoring method of full-bridge traffic load distribution based on yolov3 machine vision. *Structural Control and Health Monitoring*, 27(12), dec 2020.

[146] Pei-feng Hu, Zong-zhong Tian, and Hong-chao Liu. Traffic Counting Errors Due to Occlusion in Video Image Vehicle Detection Systems. In *ICCTP 2010*, pages 2408–2419, Beijing, China, jul 2010. American Society of Civil Engineers.

[147] Angel Sánchez, Pedro D. Suárez, Aura Conci, and Eldman O. Nunes. Video-Based Distance Traffic Analysis: Application to Vehicle Tracking and Counting. *Computing in Science & Engineering*, 13(3), may 2011.

[148] Shengfa Miao, Arno Knobbe, Eddy Koenders, and Carlos Bosma. Analysis of Traffic Effects on a Dutch Highway Bridge. *IABSE Symposium Report*, 99(27):357–364, may 2013.

[149] Xudong Jian, Ye Xia, Jose A. Lozano-Galant, and Limin Sun. Traffic Sensing Methodology Combining Influence Line Theory and Computer Vision Techniques for Girder Bridges. *Journal of Sensors*, 2019:1–15, may 2019.

[150] Michael A. Grubb, Kenneth E. Wilson, Christopher D. White, and William N. Nickas. Load and Resistance Factor Design (LRFD) for Highway Bridge Superstructures Reference Manual. Technical Report FHWA-NHI-15-047, Federal Highway Administration, Arlington, VA, jul 2015.

[151] FHWA Office of Policy. Comprehensive truck size and weight study vol3 chapter6. Technical Report FHWA-PL-00-029, U.S. Department of Transportation, aug 2000.

[152] Dongming Feng and Maria Q. Feng. Output-only damage detection using vehicle-induced displacement response and mode shape curvature index: Damage Detection Using Vehicle-Induced Displacement and MSC Index. *Structural Control and Health Monitoring*, 23(8):1088–1107, aug 2016.